リモートセンシングの防災分野への応用
Application of Remote Sensing to Disaster Management

July 5, 2018

山崎　文雄　Fumio Yamazaki

千葉大学　Chiba University, Japan

http://ares.tu.chiba-u.jp/

Contents

Objectives of Remote Sensing in Disaster Management

- **Pre-event exposure and topography mapping:**
  land-cover classification, building and road detection, DSM/DEM, surface temperature

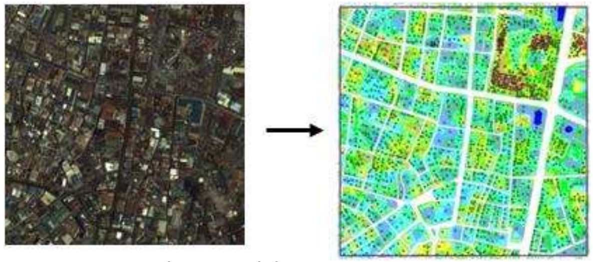

- **Post-event damage assessment**:
  change detection due to natural and man-made disasters

•***Pre-event*** *use is basically the same as other application fields.*

•*Combined use of* ***texture*** *(optical/SAR) and* ***GIS*** *&* ***DEM*** *is important for pre- and post-event* ***damage assessment****.*

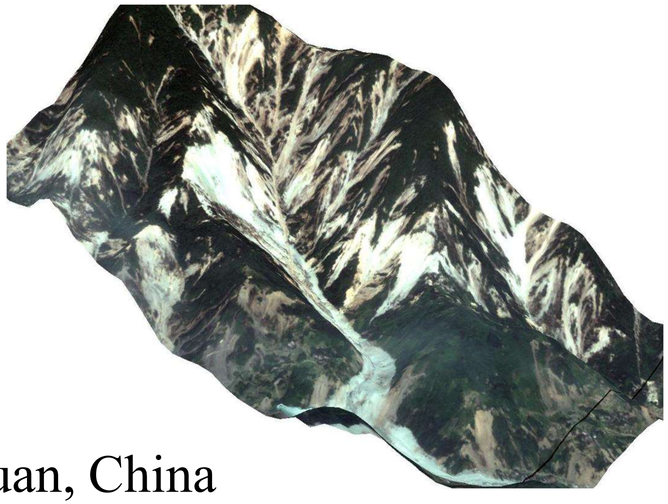

Sichuan, China

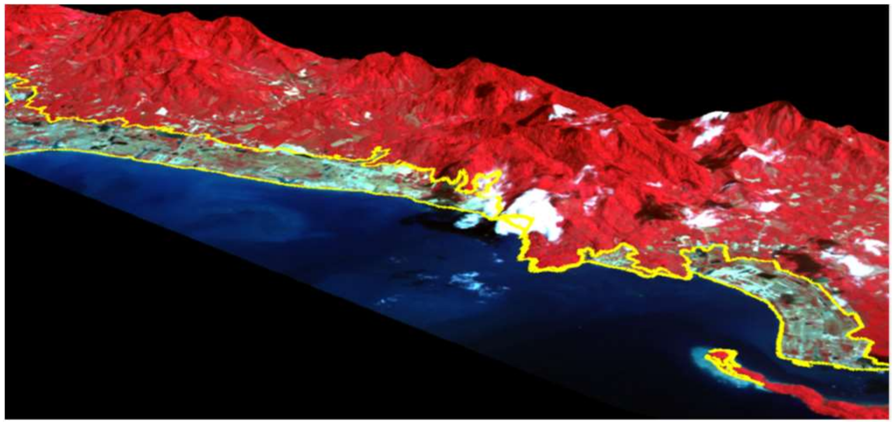

Khao Lak, Thailand

Platforms of Remote Sensing

- **Satellite**: near-polar orbit, geo-stationary, Space Shuttle/Station
- **Airborne platform**: airplane, helicopter, drone
- **Ground-based**: balloon, tall building, crane, ladder, car

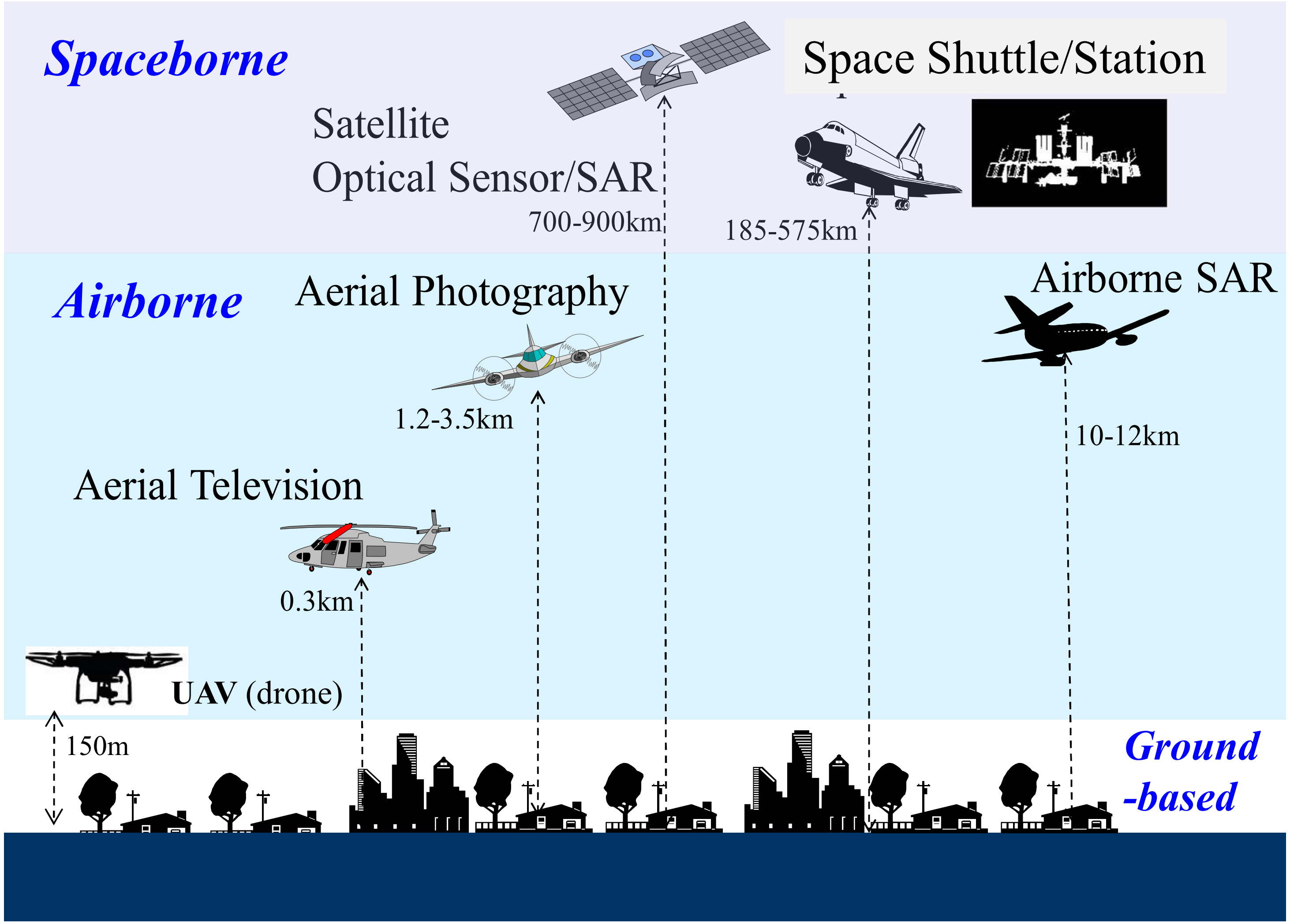

Wavelength of Electromagnetic Waves and Satellite Sensors

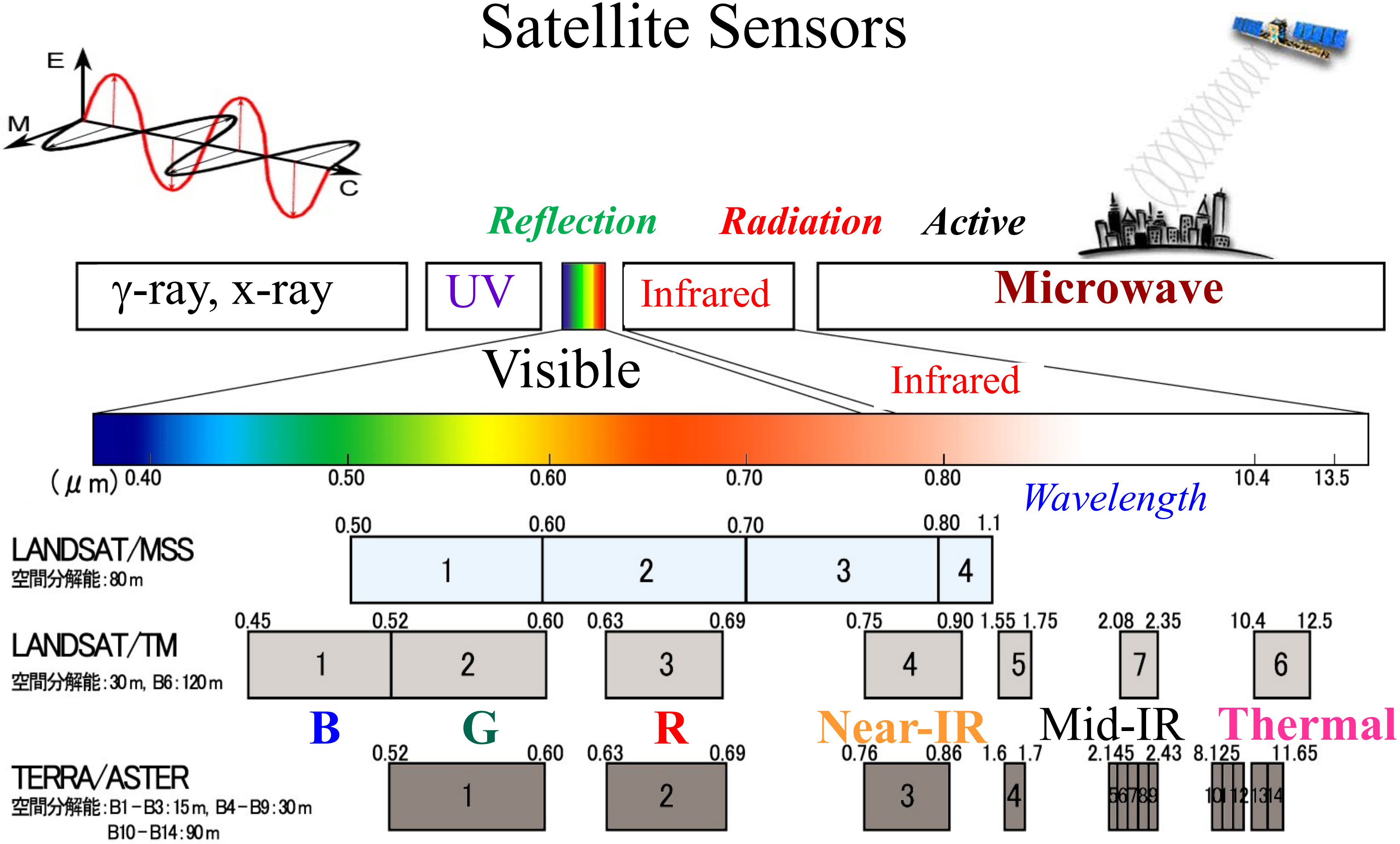

Acquisition condition of various sensors and platforms in disaster response

Platform /Sensor	Satellite ◎ Large coverage	Airborne ○ Mod. coverage	Ground Based △ Low coverage
Optical Sensor	△ Day, Fixed time △ No cloud	○Day, Any time ○ No low cloud	◎ Day, Any time
LiDAR	△	○ All day, Any time ○ No low cloud ◎ High accuracy	◎ Day, Any time
Thermal Infrared	○All day, Fixed time △ No cloud △ Low resolution	◎ All day, Any time ○ No low cloud ○ Mod. resolution	◎All day, Any time ◎ High resolution
SAR	○ All day, Fixed time ◎ All weather	◎ All day, Any time ◎ All weather △ R & D stage	△ Ground penetration Radar

Contents

- Remote Sensing and Disaster Management
- Satellite Optical and Thermal Sensors
- Satellite SAR
- Airborne SAR
- Lidar and UAV

Landsat-5 TM Images of Kobe area in 1994-95

Aug. 17, 1994 (Before EQ)

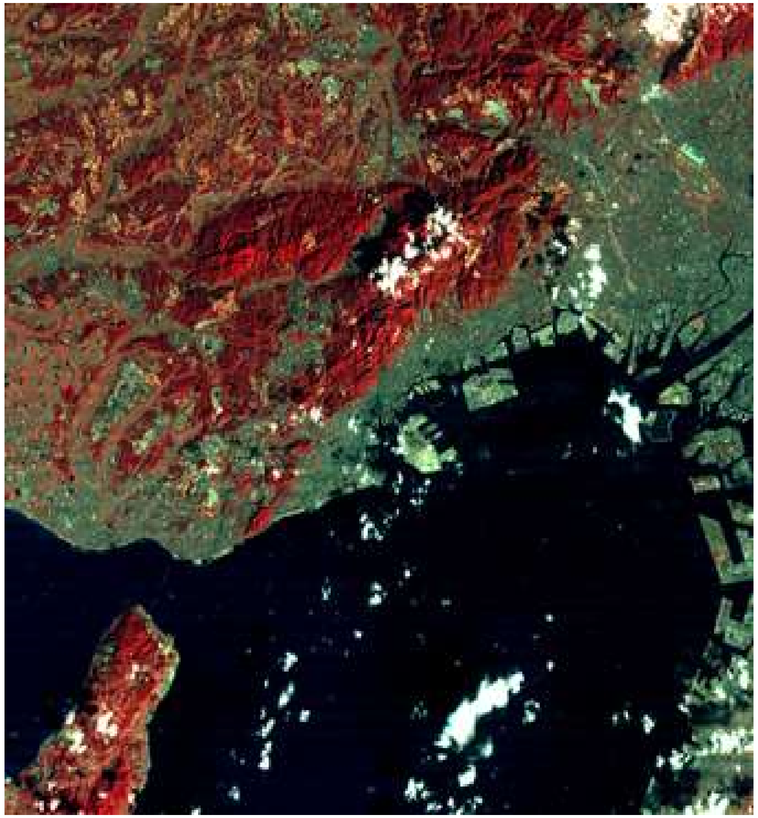

Jan. 24, 1995 (After EQ)

1998 RIKEN EDM
Disaster Information Systems Team

Damage Distribution Estimated from Landsat-5 Images

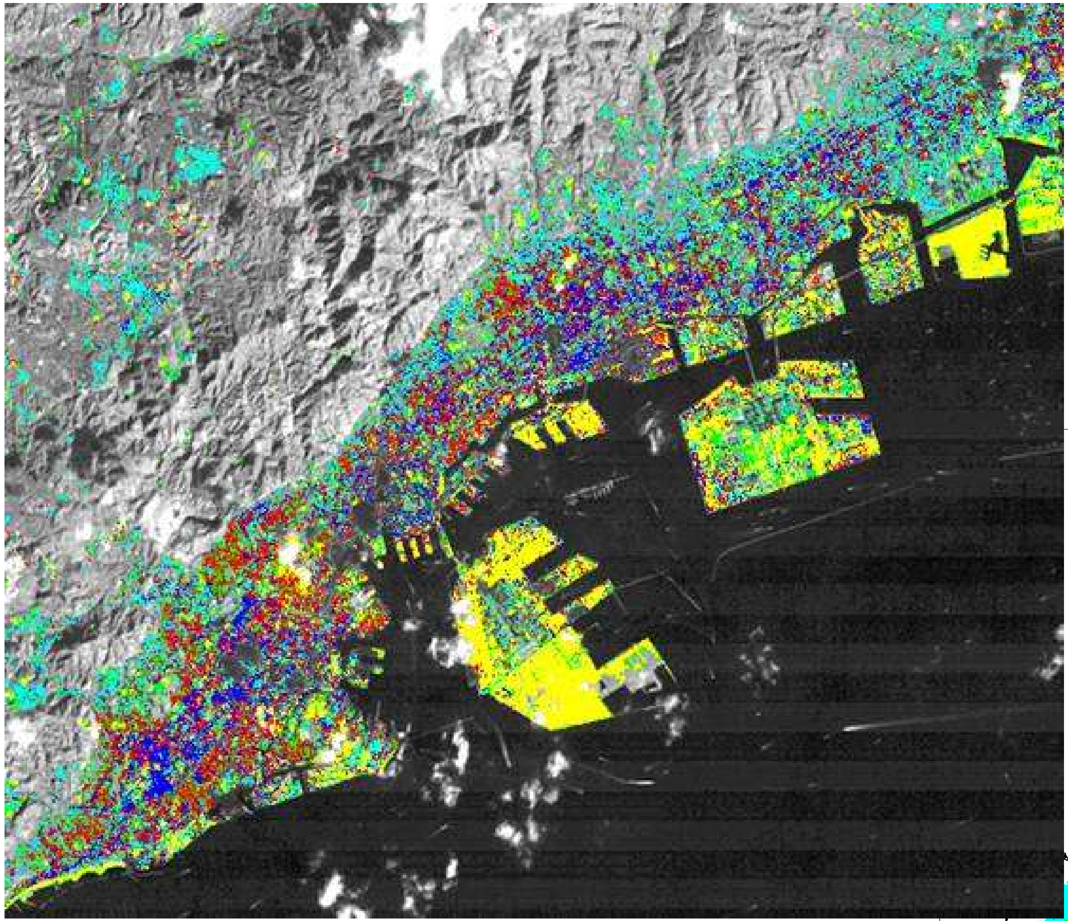

Pre-event: 08/17/94
Post-event: 01/24/95

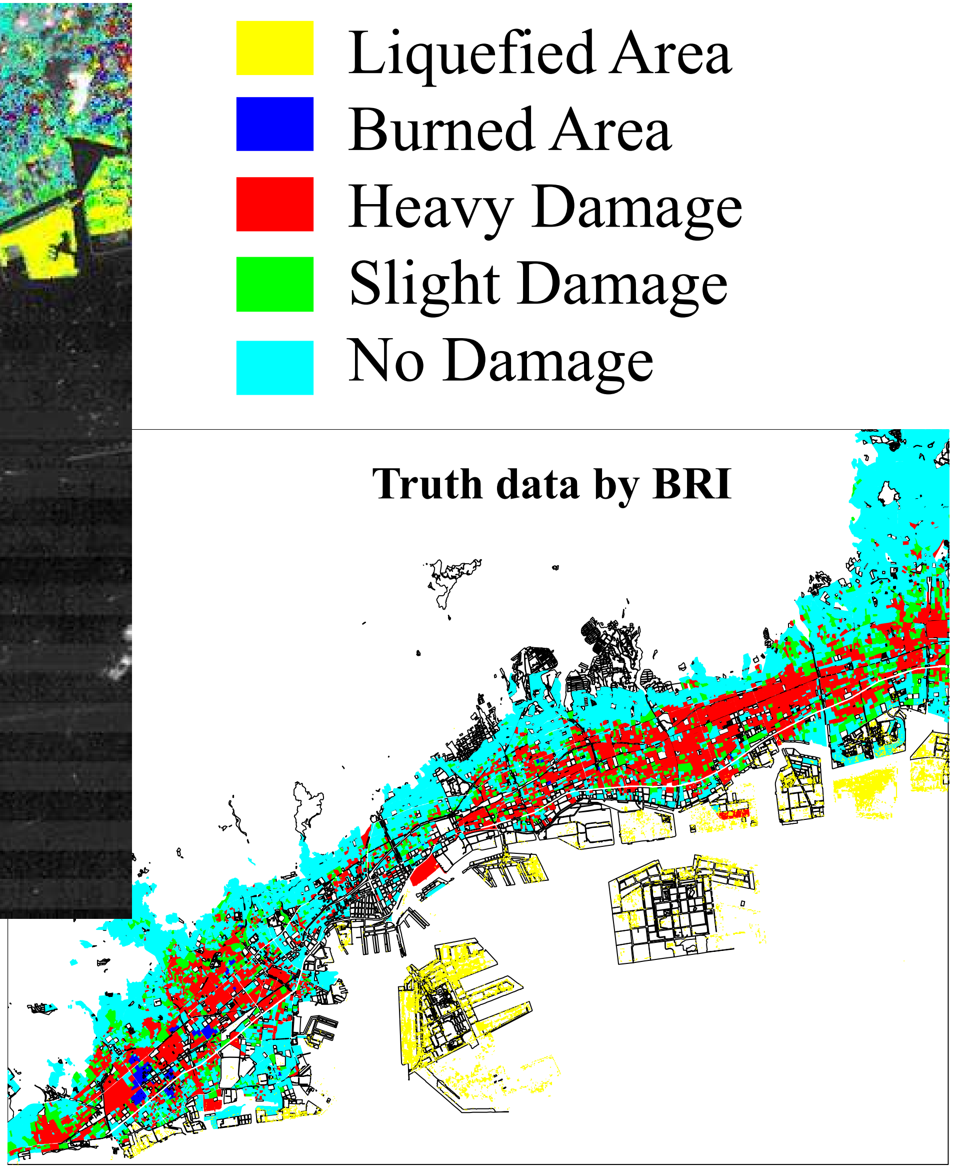

松岡昌志，山崎文雄，翠川三郎，土木学会論文集, No. 648/I-54, pp. 177-185, 2001

Use of GPS and RS Data for Field Survey

Joint Survey by MCEER/EDM after the 1999 Kocaeli, Turkey EQ

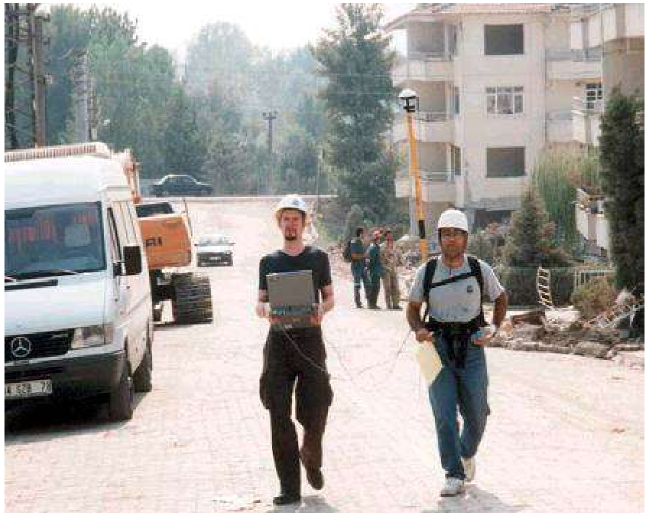

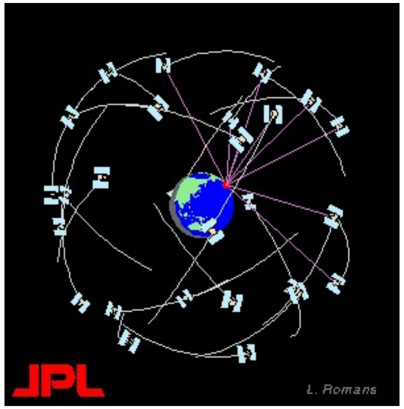

Landsat image as a base map

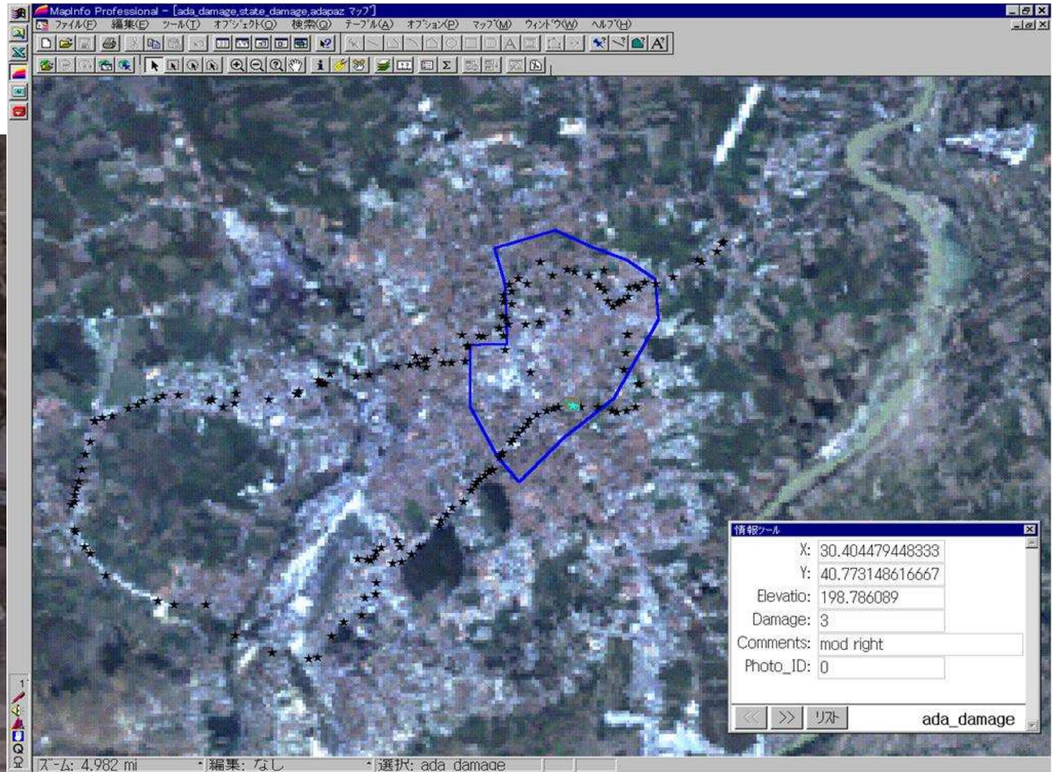

Spatial Resolution: ASTER and QuickBird Images of Bam, Iran

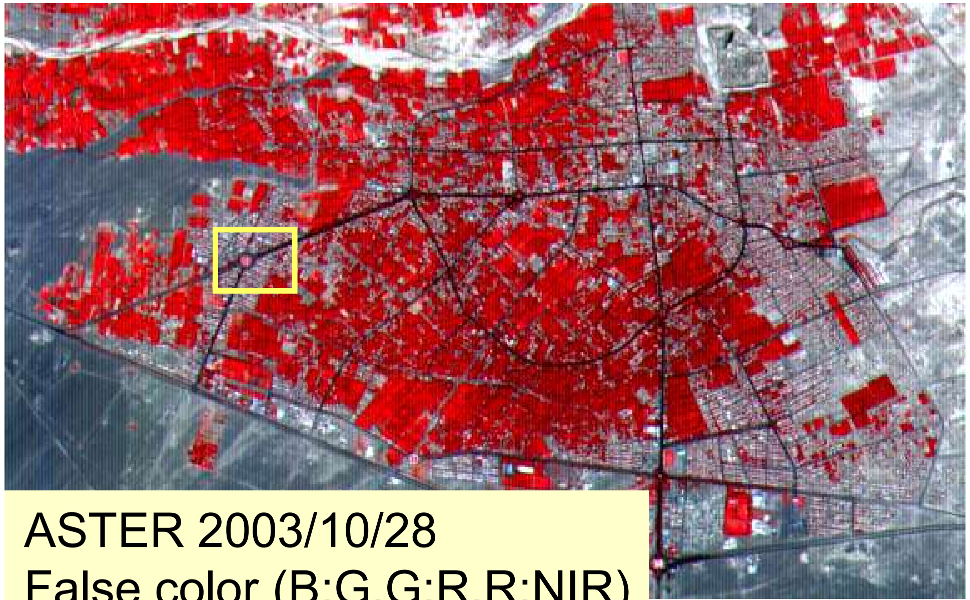

ASTER 2003/10/28
False color (B:G,G:R,R:NIR)
Pixel size : 15m

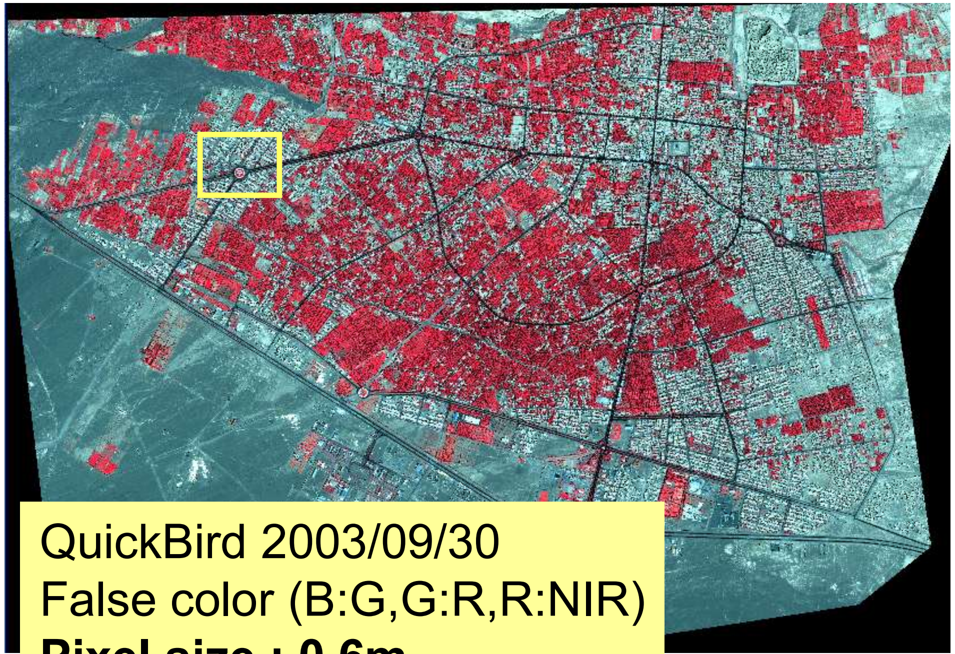

QuickBird 2003/09/30
False color (B:G,G:R,R:NIR)
Pixel size : 0.6m

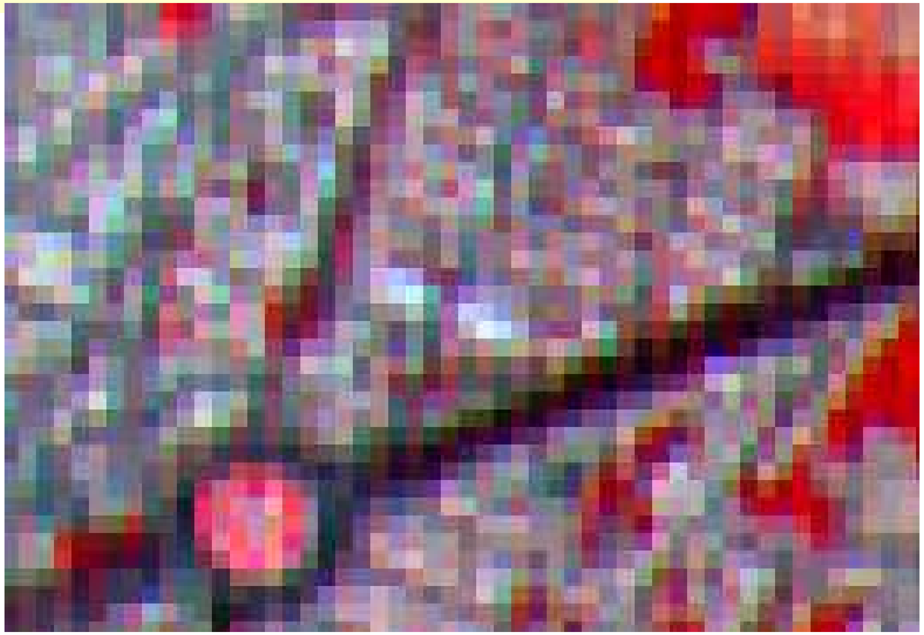

Change Detection: QB images of Bam, Iran

Pre-event 2003.9.30 → Post-event 2004.1.3

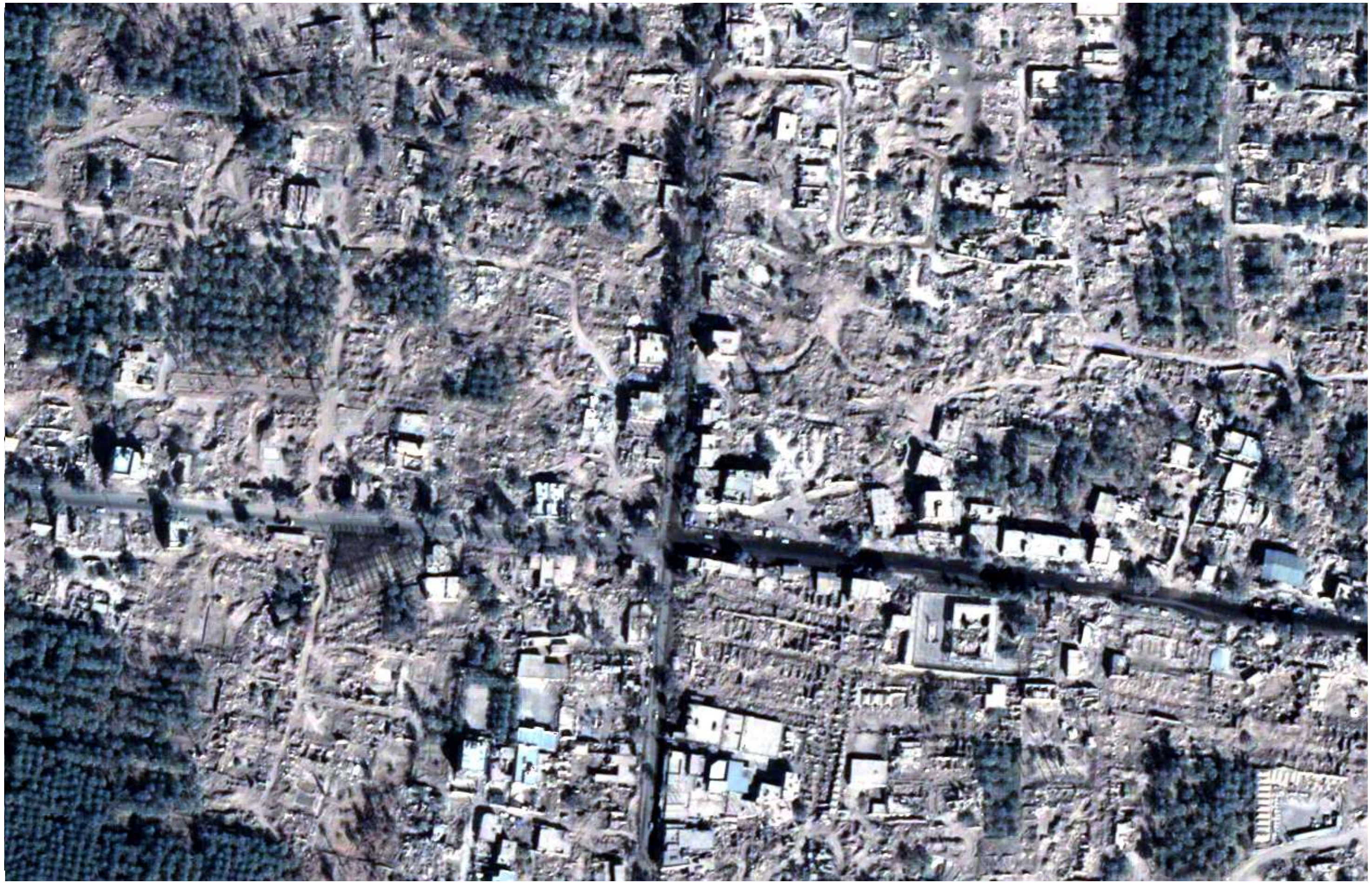

Damage classification of masonry buildings (EMS, 1998) and typical pre- and post event QB images

EMS: *European Macroseismic Scale*

Classification of damage to masonry buildings	
	**Grade 1: Negligible to slight damage (no structural damage, slight non-structural damage)** Hair-line cracks in very few walls. Fall of small pieces of plaster only. Fall of loose stones from upper parts of buildings in very few cases.
	**Grade 2: Moderate damage (slight structural damage, moderate non-structural damage)** Cracks in many walls. Fall of fairly large pieces of plaster. Partial collapse of chimneys.
	**Grade 3: Substantial to heavy damage (moderate structural damage, heavy non-structural damage)** Large and extensive cracks in most walls. Roof tiles detach. Chimneys fracture at the roof line; failure of individual non-structural elements (partitions, gable walls).
	**Grade 4: Very heavy damage (heavy structural damage, very heavy non-structural damage)** Serious failure of walls; partial structural failure of roofs and floors.
	**Grade 5: Destruction (very heavy structural damage)** Total or near total collapse.

Pre- event | Post- event

Grade 3

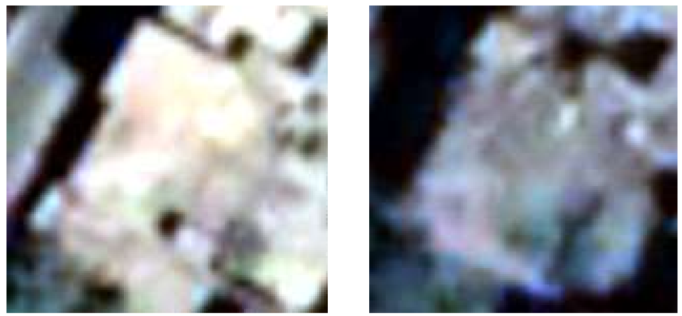

Grade 4

Grade 5

Result of visual damage detection of QB images for Bam City

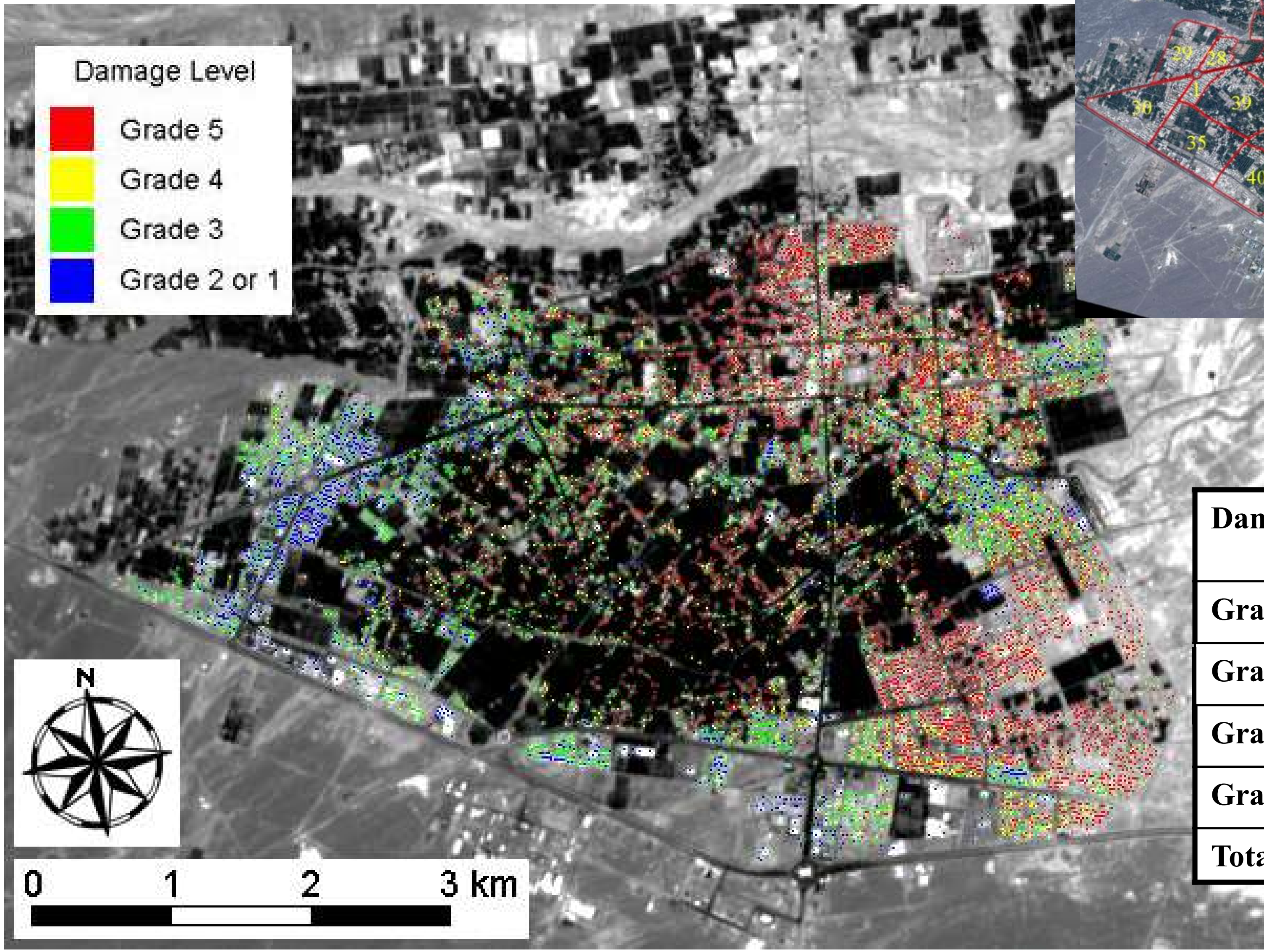

Number of blocks= 41

Damage	Number of buildings
Grade 1 & 2	1,597
Grade 3	3,815
Grade 4	1,700
Grade 5	4,951
Total	12,063

Yamazaki, Yano and Matsuoka (2005) Earthquake Spectra

Shadow Correction of Optical Image 光学画像における影補正

QuickBird Image of Bangkok
November 7, 2002
10:53 AM

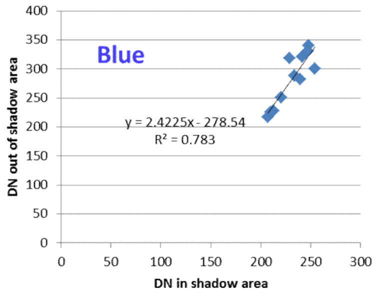

Spectroradiometer measurement

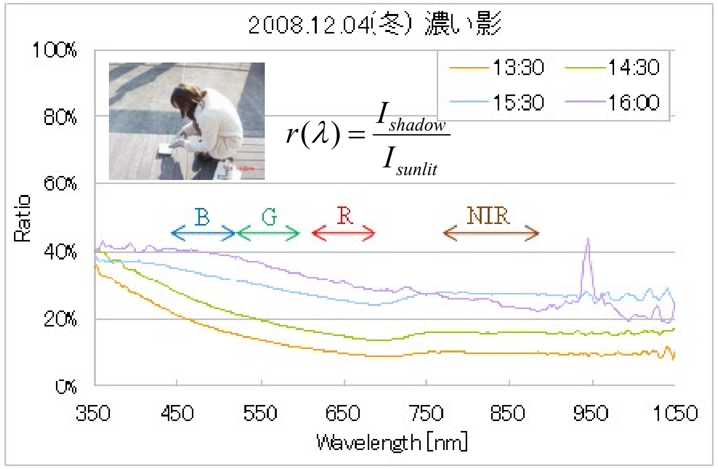

Shadow and non-shadow pairs

Original image

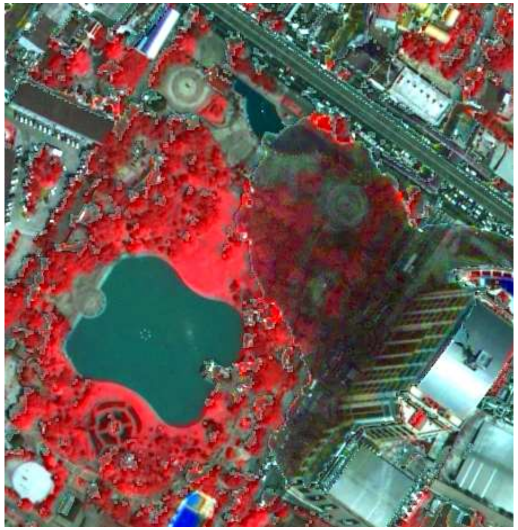

Corrected image

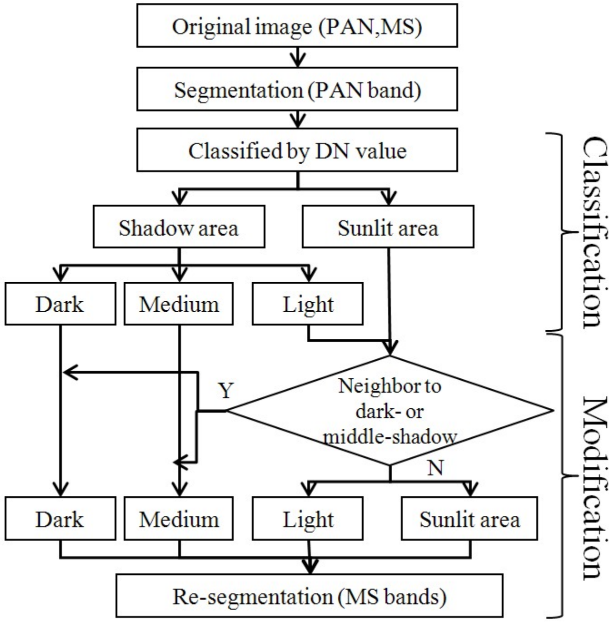

W. Liu, F. Yamazaki, Object-Based Shadow Extraction and Correction of High-Resolution Optical Satellite Images, IEEE JSTARS, pp. 1-7, 2012.

Original and corrected shadow-free QB images

False Color

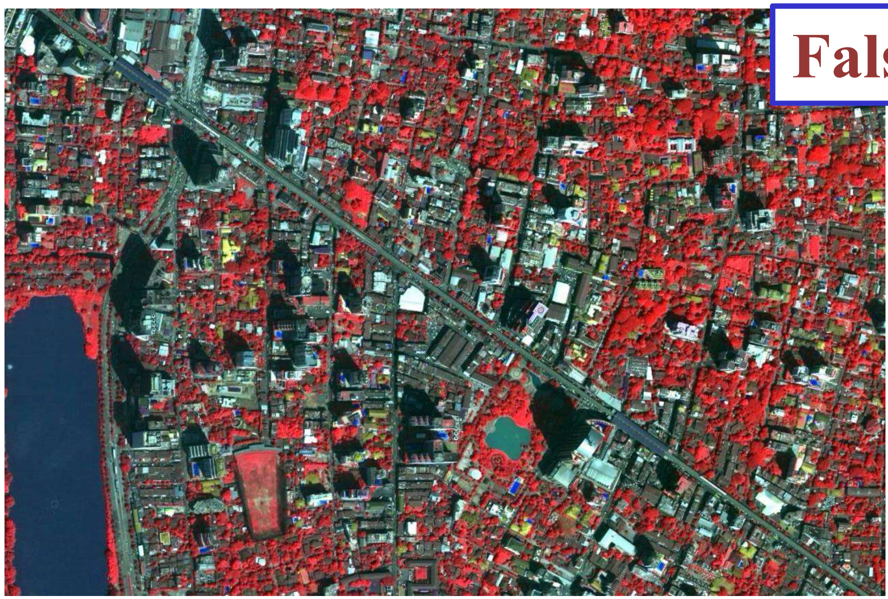

Original image

Corrected shadow-free image

Unsupervised Classification

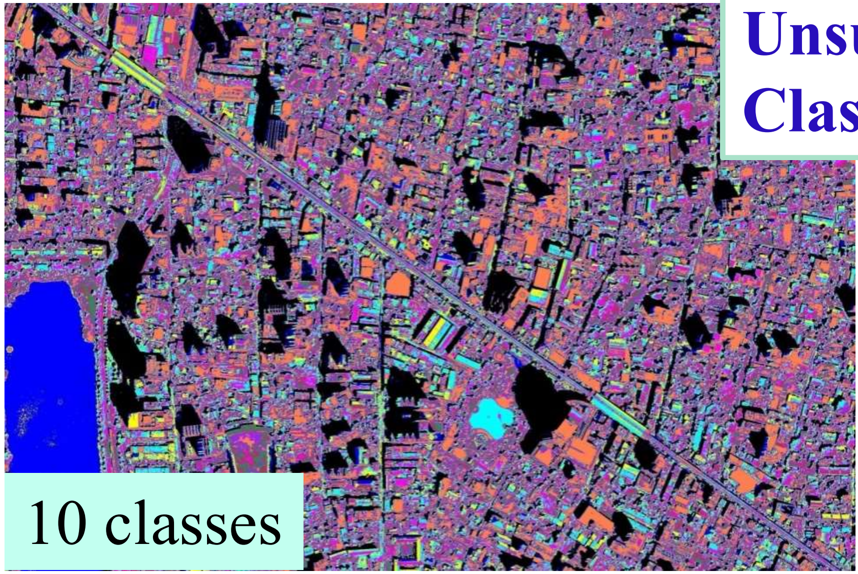

10 classes

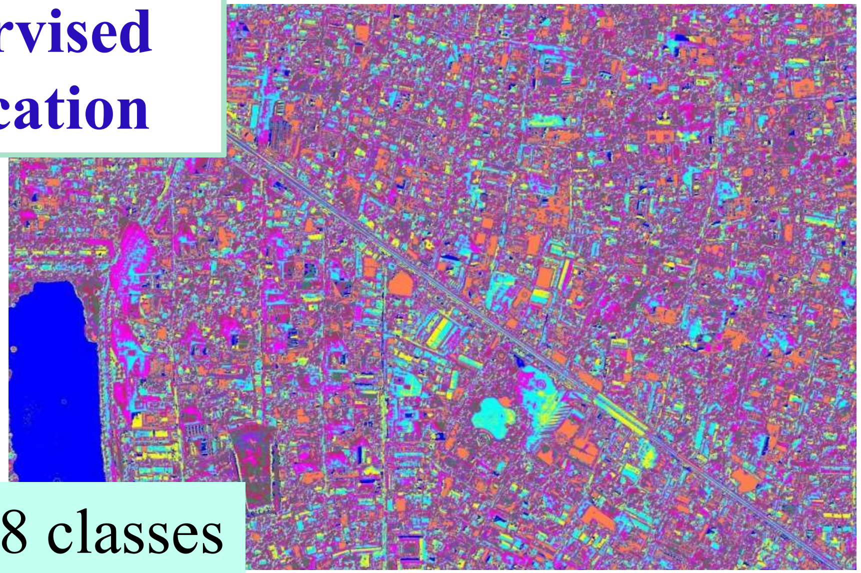

8 classes

Satellites that observed the M9.0 2011 Tohoku earthquake

Optical, Medium Resolution

- ALOS AVNIR-2 (10m)
- Terra ASTER (15m)
- Landsat 7 (30m)

SAR

- ALOS PALSAR (L-band, 6.25m)
- Radarsat 1, 2 (C-band, 8m)
- TerraSAR-X (X-band, 3m)
- COSMO-SkyMed (X-band, 3m)

Optical, High Resolution

- FORMOSAT-2 (2.0m)
- THEOS (2.0m)
- RapidEye (2.5m)
- WorldView-1,2 (0.5m)
- QuickBird (0.6m)
- Ikonos (1.0m)
- GeoEye-1 (0.5m)

2011.3.30 @ Sendai

WoldView2 & QuickBird

by Digital Globe

Aerial survey has been banned over Fukushima Daiichi NPP

March 14, 2011 11:04 am,
three minutes after #3 reactor caused hydrogen explosion

http://www.digitalglobe.com/index.php/27/S

ASTER TIR Images of Soma in the 2011 Tohoku EQ tsunami

東日本大震災前後のASTER夜間熱赤外画像　福島県相馬市

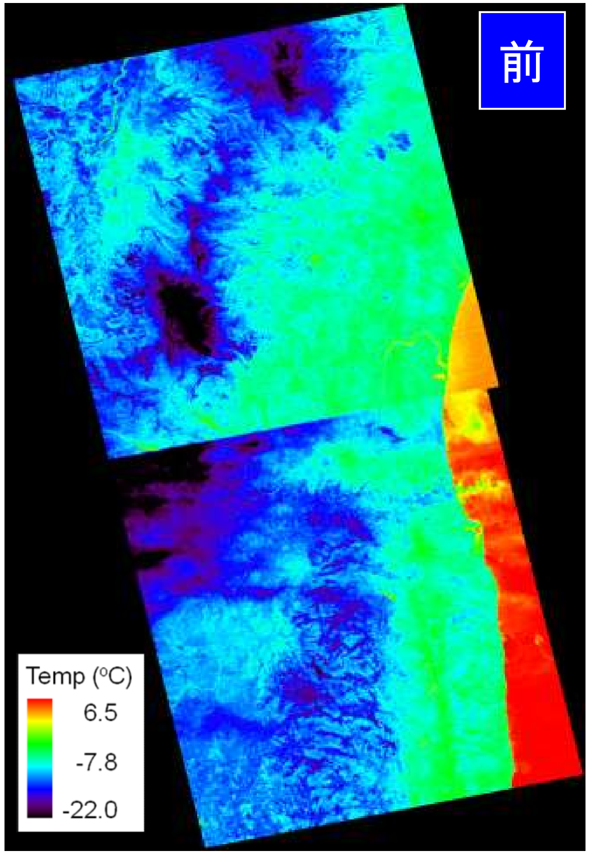

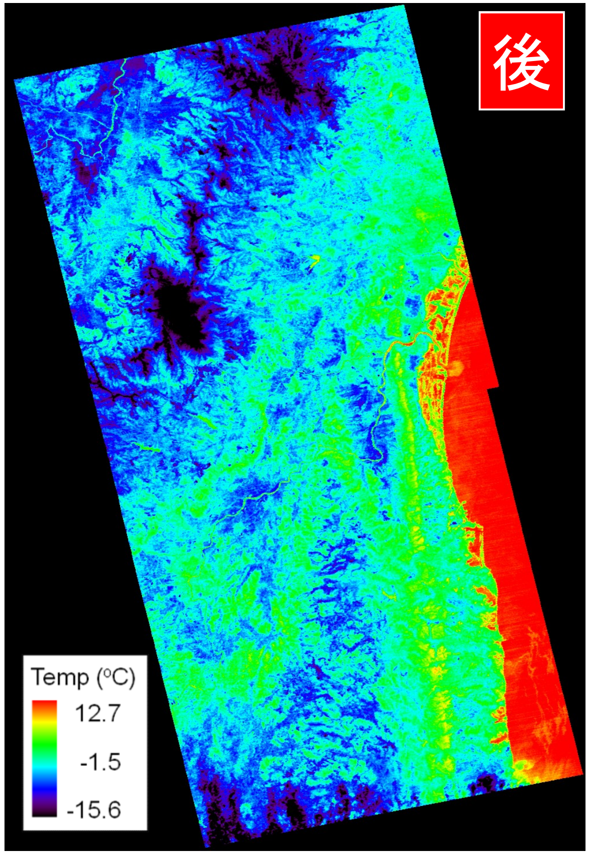

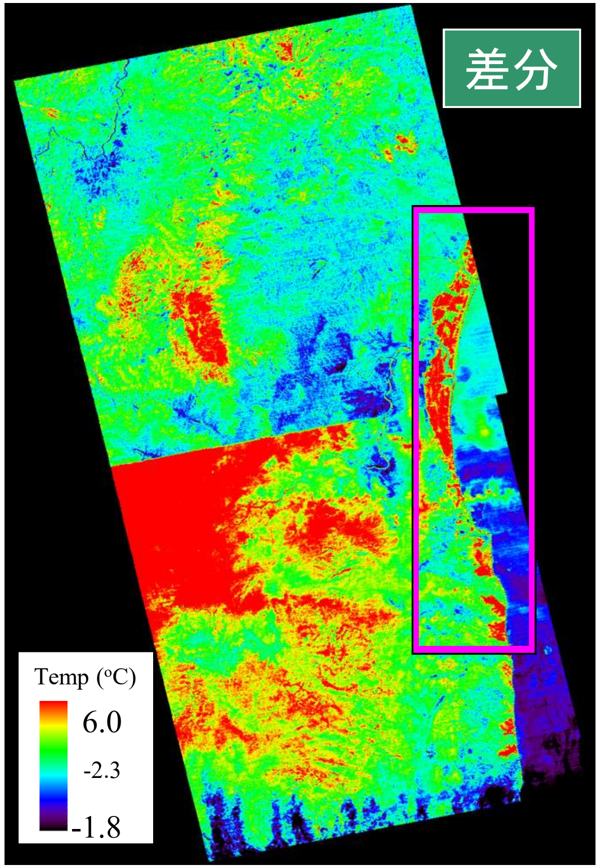

Pre-event:
2010/2/21 & 2008/1/15

Post-event:
2011/3/12

Soma City (21:30, **Nighttime**)

ΔTemp

解像度90m

花田大輝，山崎文雄，日本地震工学会論文集，Vol. 12, No. 6, 2012.

Tsunami flooded area estimation by ASTER TIR images

Areas more than 5° C increase excluding 9 m above sea level 相馬・夜間

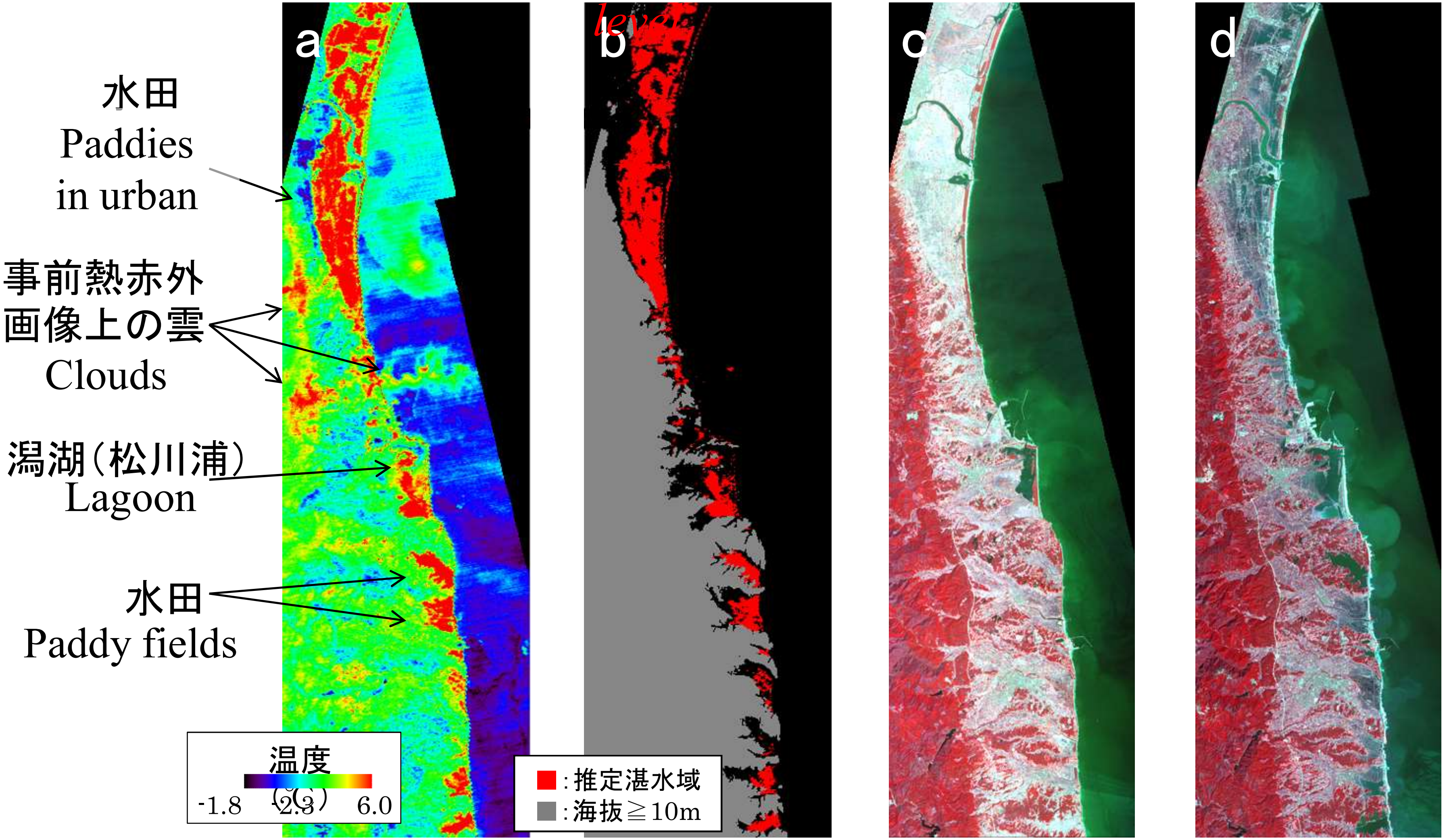

温度変化	推定湛水域	地震前画像	地震後画像
ΔTemp	Estimated Flooded Areas	Pre-event false color	Post-event false color

Contents

- Remote Sensing and Disaster Management
- Satellite Optical and Thermal Sensors
- Satellite SAR
- Airborne SAR
- Lidar and UAV

Flow of post-event damage assessment

Pre-event Archive Data

SAR images | Optical images | GIS, DEM

↓

Disaster

Emergency Observation

SAR images → ← GPS data

↓

Damage Assessment 1-3 days

Good Weather

Optical images → ← **Field Survey**

↓

Damage Confirmation 1-2 weeks

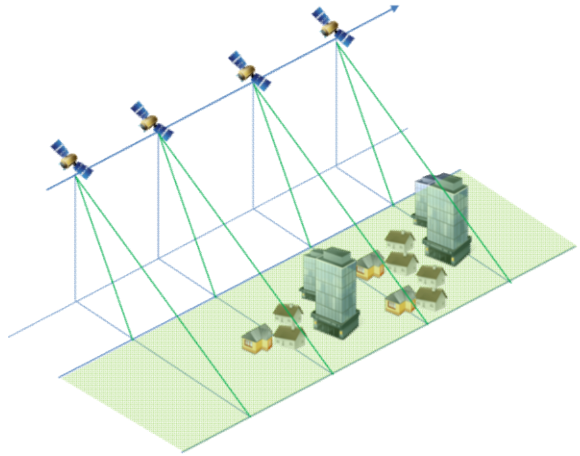

Characteristics of SAR

- All Weather, Daytime and Nighttime
- Combined use with GIS and Optical images
- Include height and lateral information due to side-looking mode

Change Detection from SAR intensity images

1. Image matching
2. Speckle noise filtering (*Lee Filter*)
3. Calculating following indices:

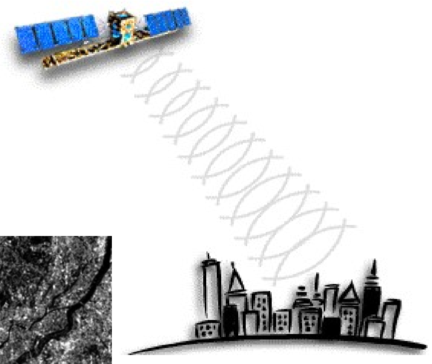

✓ **Difference** of backscattering coefficients (after – before)

$$d[dB] = \bar{I}a_i - \bar{I}b_i$$

✓ **Correlation** coefficient

$$r = \frac{N\sum_{i=1}^{N} Ia_i Ib_i - \sum_{i=1}^{N} Ia_i \sum_{i=1}^{N} Ib_i}{\sqrt{\left(N\sum_{i=1}^{N} Ia_i^{\,2} - \left(\sum_{i=1}^{N} Ia_i\right)^2\right)\cdot\left(N\sum_{i=1}^{N} Ib_i^{\,2} - \left(\sum_{i=1}^{N} Ib_i\right)^2\right)}}$$

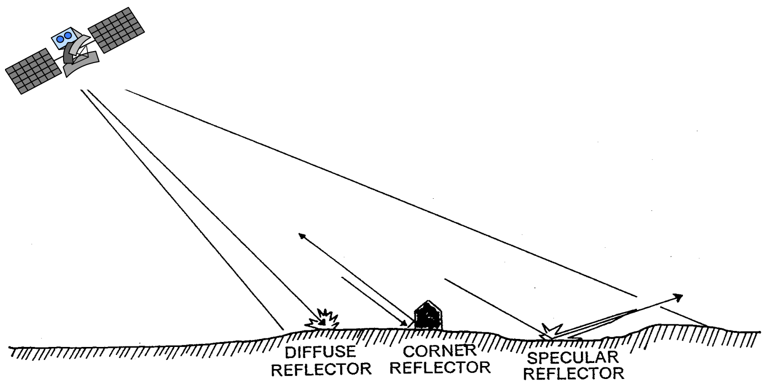

Ia_i and Ib_i are the digital numbers of the post- and pre-images.

$\bar{I}a_i$ and $\bar{I}b_i$ are the corresponding averaged digital numbers over the pixel window.

Estimated Damage Areas in 1995 Kobe EQ using ERS/SAR

✓ **Difference** of backscattering coefficient (1995/5/23 – 1994/6/3)

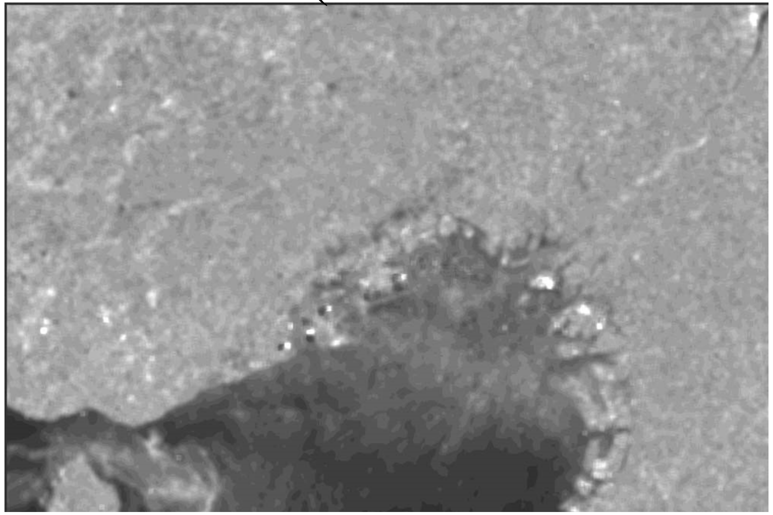

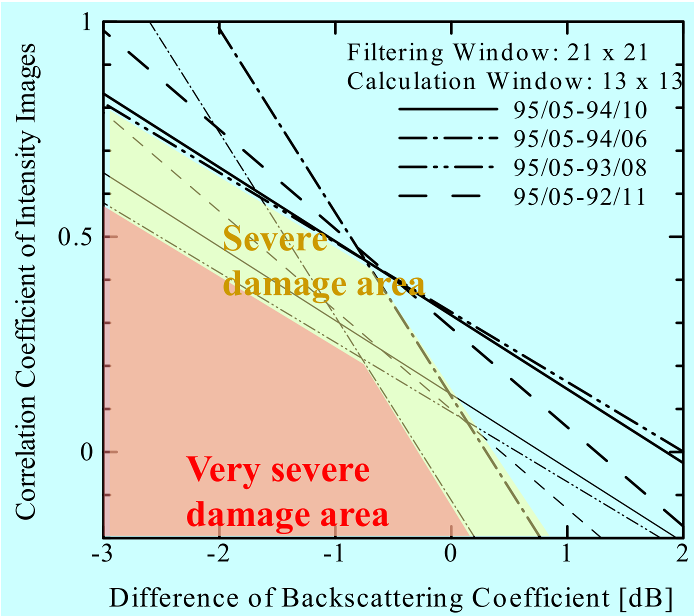

✓ **Correlation** coefficient

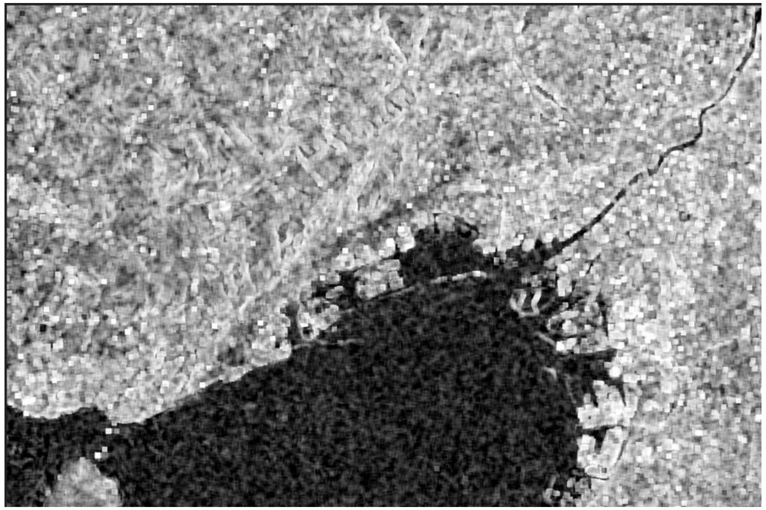

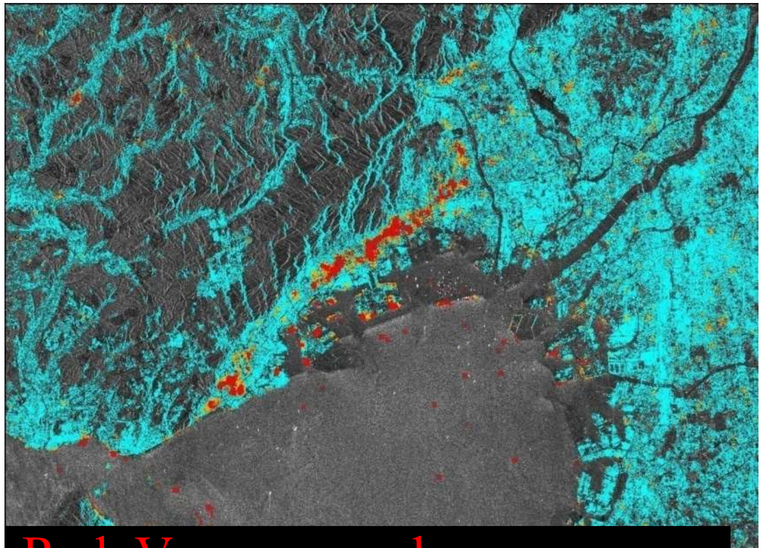

Red: Very severe damage area
Yellow: Severe damage area

M. Matsuoka, F. Yamazaki, Earthquake Spectra, Vol.20, No. 3, pp. 975-994, 2004.

TerraSAR-X intensity data of Sendai area for the 2011 Tohoku EQ

Pre-event

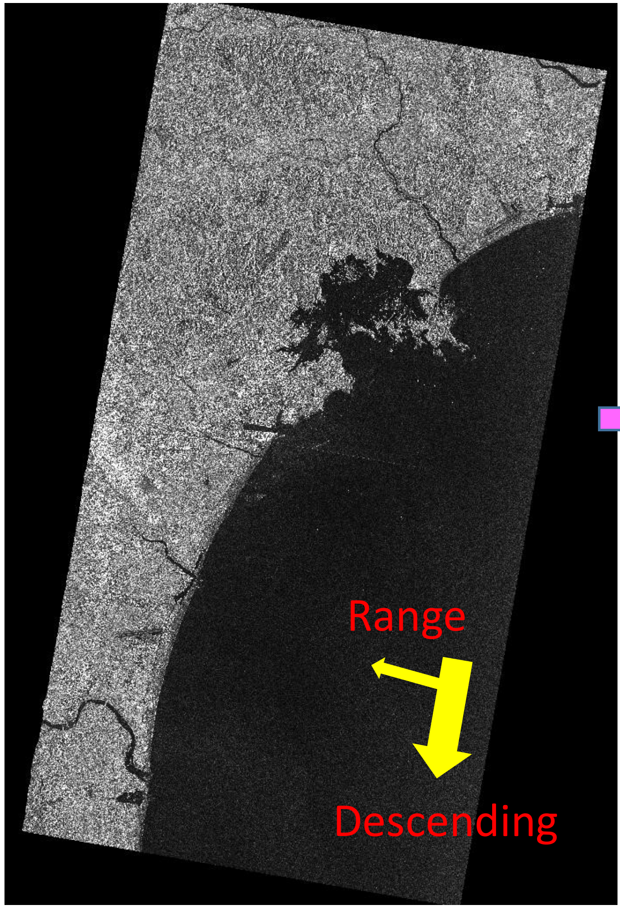

UTC: 2010/10/20, 20:43
Japan ST: **2010/10/21**, 5:43
Incidence angle: 37.32°

Post-event

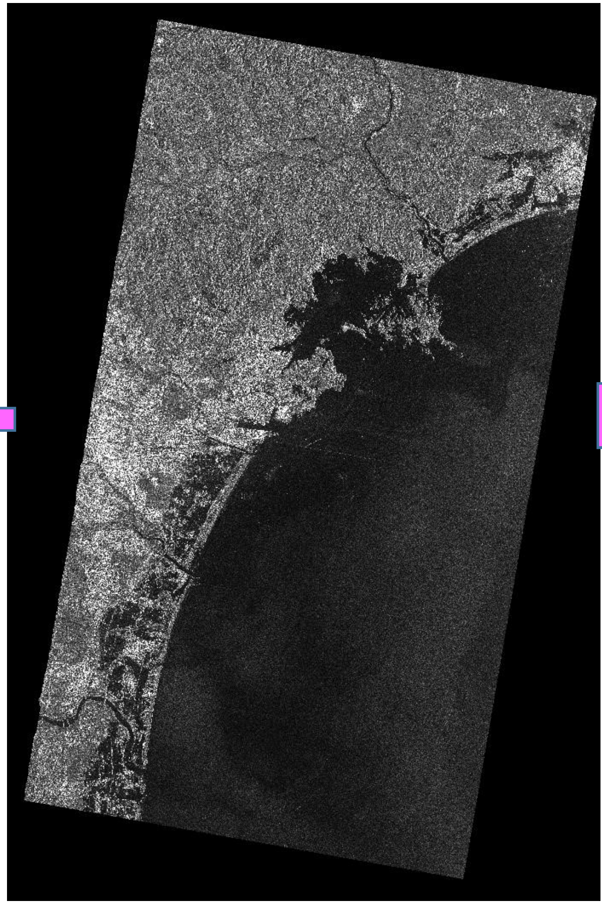

UTC: 2011/03/12, 20:43
Japan ST: **2011/03/13**, 5:43
Incidence angle: 37.30°

R: 2011/03/13
G&B: 2010/10/21

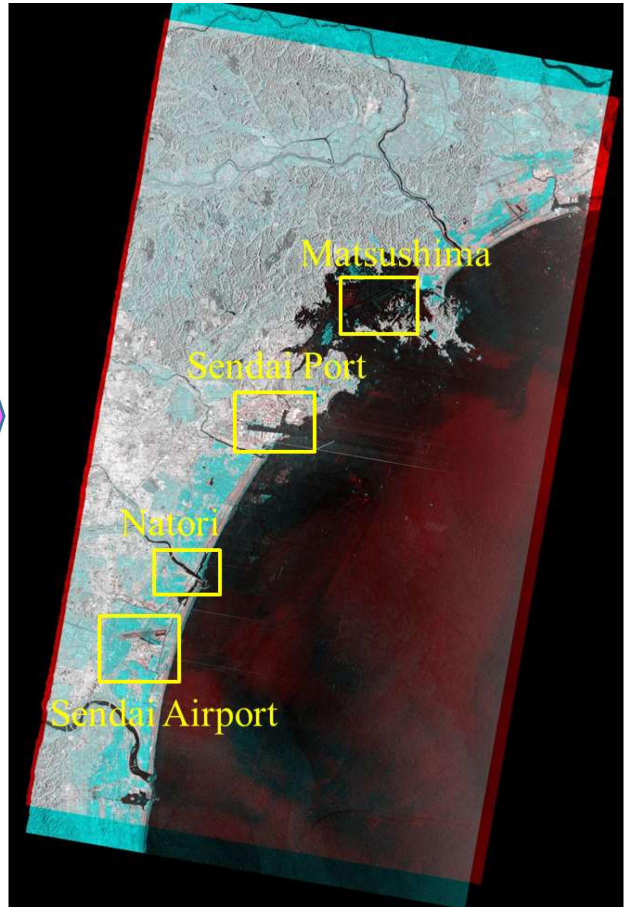

■ Reduced backscatter
Flooded areas etc.
■ Increased backscatter
Debris etc.

StripMap mode, HH polarization

Movement of an intact building in SAR images

Pre-event

Post-event

Color composite

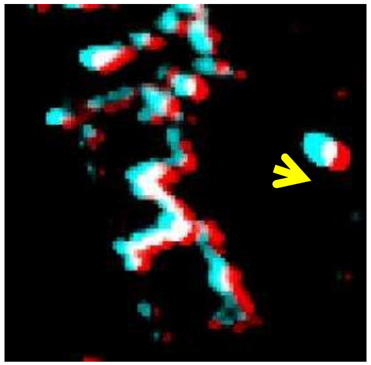

T: Pre-event SAR

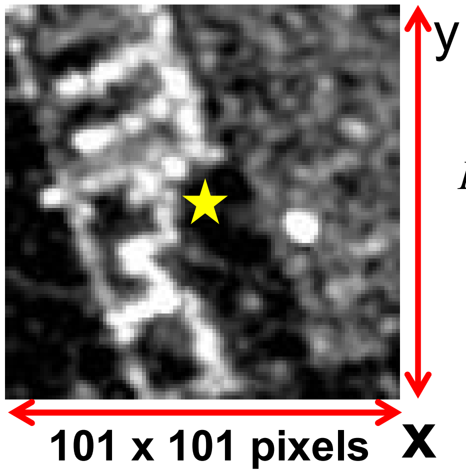

101 x 101 pixels

I: Post-event SAR

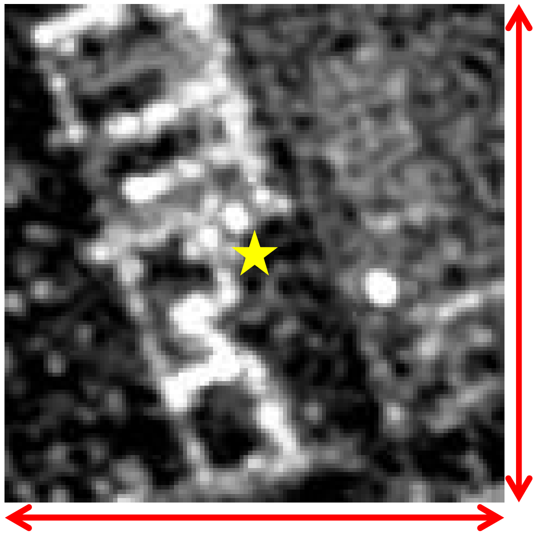

115 x 115 pixels

G&B: 2010.10.21 **R: 2011.03.13**

Area-based correlation

$$R(a,b)=\frac{\sum_{i=0}^{M_T-1}\sum_{j=0}^{N_T-1}\left\{I_{(a,b)}(i,j)-\bar{I}\right\}\left\{T(i,j)-\bar{T}\right\}}{\sqrt{\sum_{i=0}^{M_T-1}\sum_{j=0}^{N_T-1}\left\{I_{(a,b)}(i,j)-\bar{I}\right\}^2}\sqrt{\sum_{i=0}^{M_T-1}\sum_{j=0}^{N_T-1}\left\{T(i,j)-\bar{T}\right\}^2}}$$

$$\bar{I}=\frac{1}{M_T N_T}\sum_{i=0}^{M_T-1}\sum_{j=0}^{N_T-1}I_{(a,b)}(i,j)\qquad \bar{T}=\frac{1}{M_T N_T}\sum_{i=0}^{M_T-1}\sum_{j=0}^{N_T-1}T(i,j)$$

Correlation Matrix

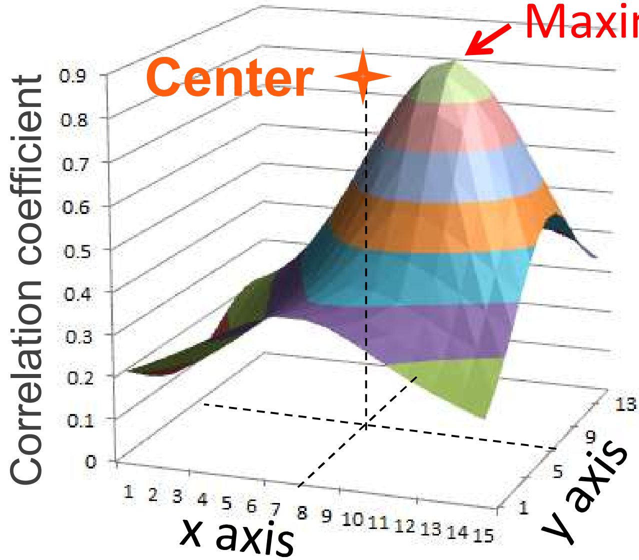

3.75 m to east, 1.25 m to south

(1.25m/pixel)

Estimation of crustal movements at GPS Yamoto

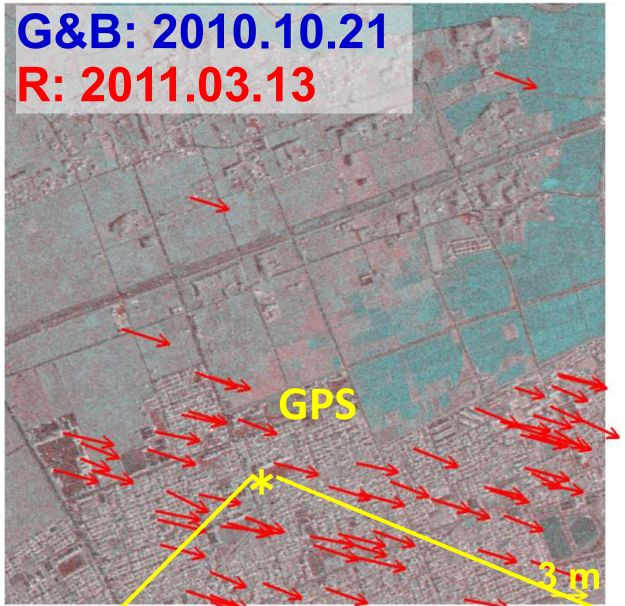

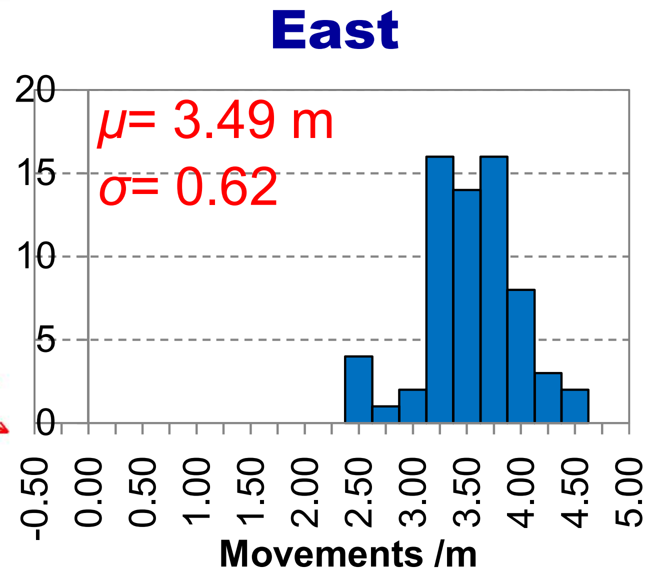

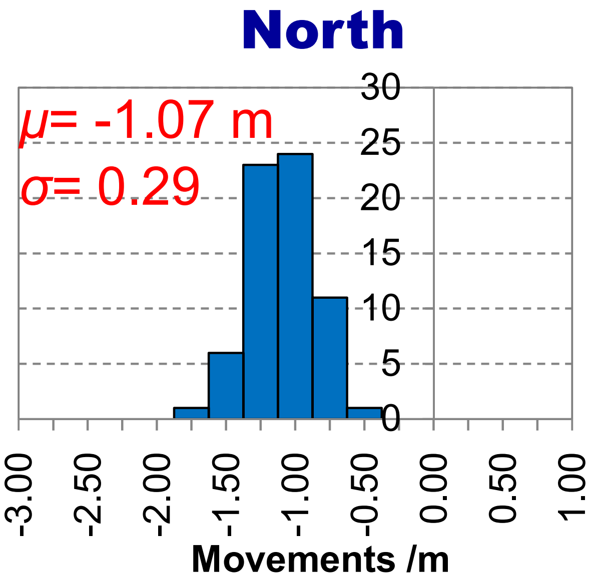

67 buildings

Google Earth 2011.04.06

Survey photo 2012.01.14

W. Liu, F. Yamazaki, Detection of Crustal Movement from TerraSAR-X intensity images for the 2011 Tohoku, Japan Earthquake, ***Geoscience and Remote Sensing Letters***, IEEE, 10(1), 2013.

Comparison with GPS observed data

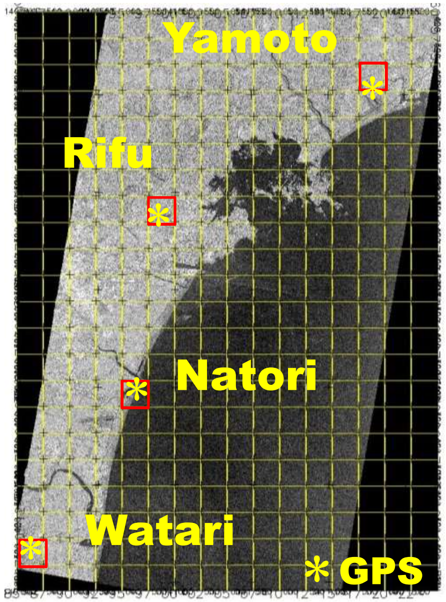

— GPS observed data □ Detected results

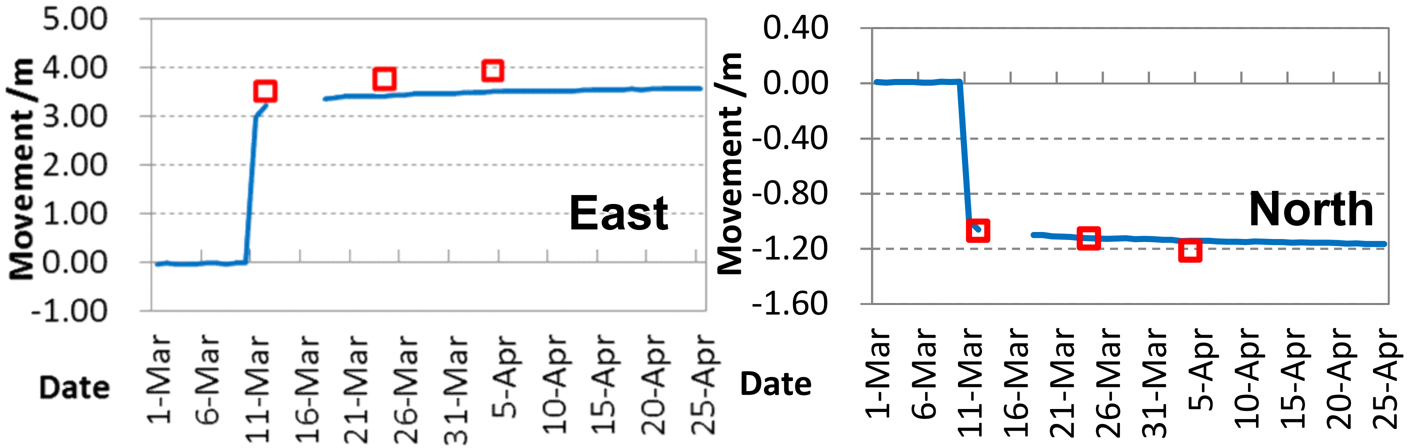

Yamoto

— GPS observed data □ Detected results

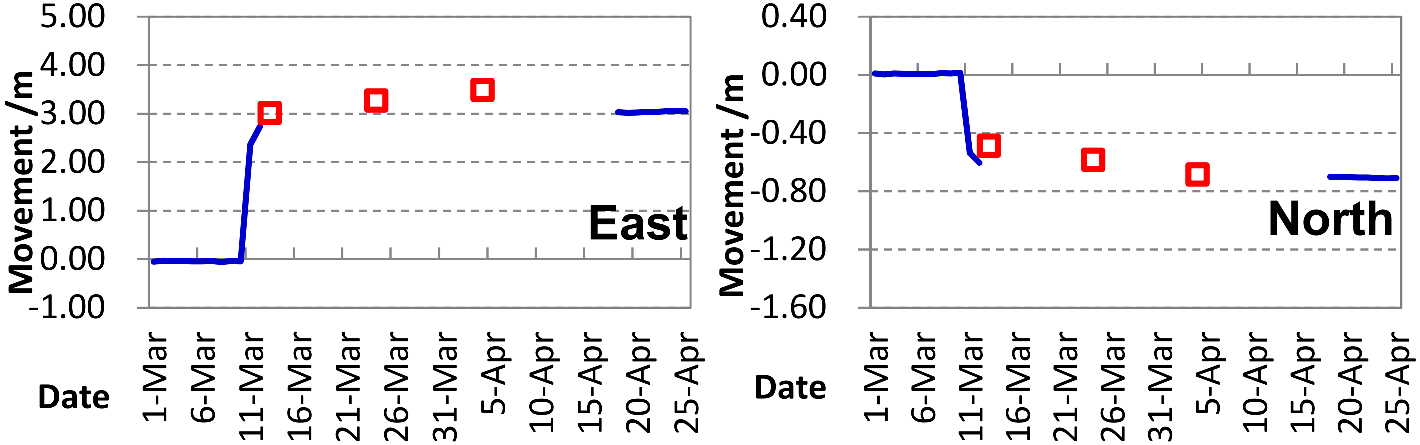

Natori

W. Liu, F. Yamazaki, IEEE Geoscience and Remote Sensing Letters, Vol. 10, No. 1, 2013.

Fukushima Daiichi nuclear power plant in September 2011

福島第一原子力発電所の事故後の状況

#1 reactor building

#2 reactor building

#3 reactor building

#4 reactor building

Photos by TEPCO on 2011/09/15

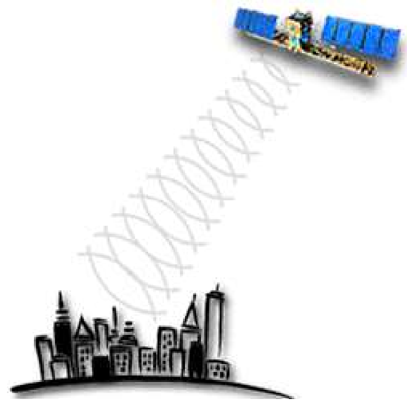

Scheme of SAR observation

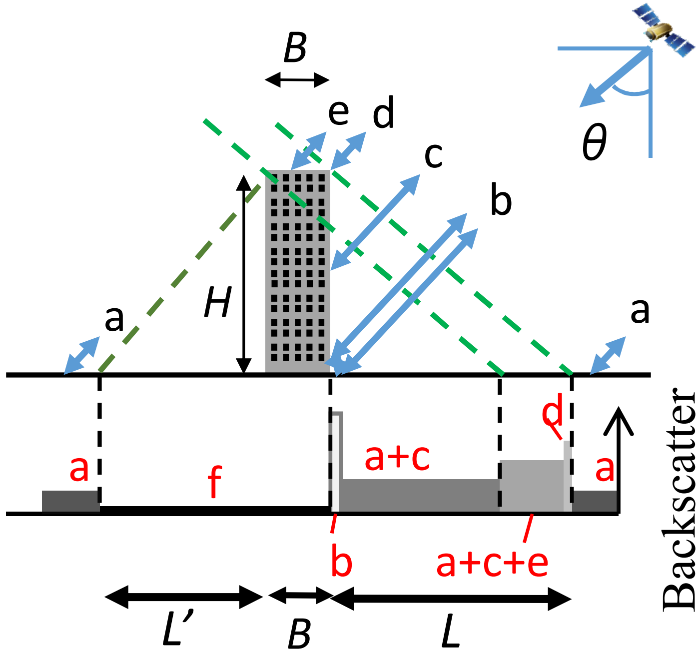

Radar Shadow

$L' = H \tan\theta$

Layover

$L = H / \tan\theta$

TerraSAR-X images of Fukushima Daiichi NPP after EQ

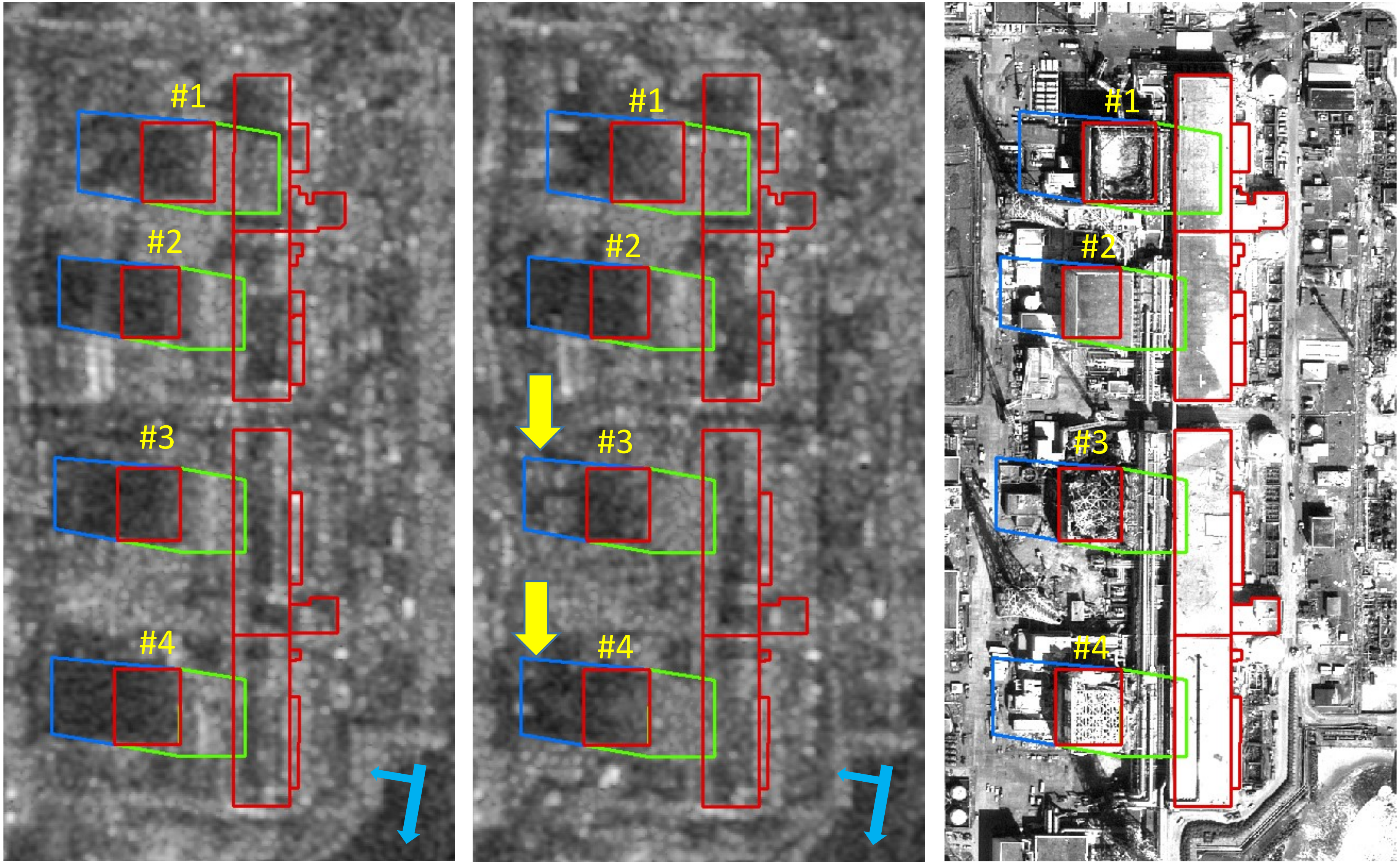

TSX 2011/03/13 05:43 | TSX 2011/09/05 05:43 | GeoEye-1 2011/09/16 09:33

Layover | Radar Shadow | Building Footprint

W. Liu, F. Yamazaki, T. Sasagawa, Journal of Disaster Research, Vol. 11, No. 2, 2016.

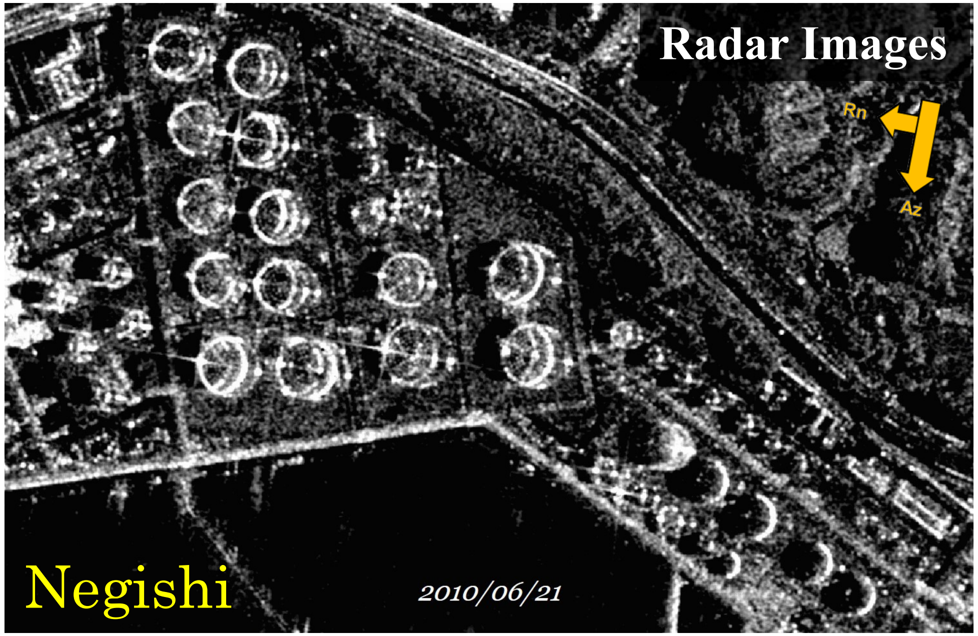

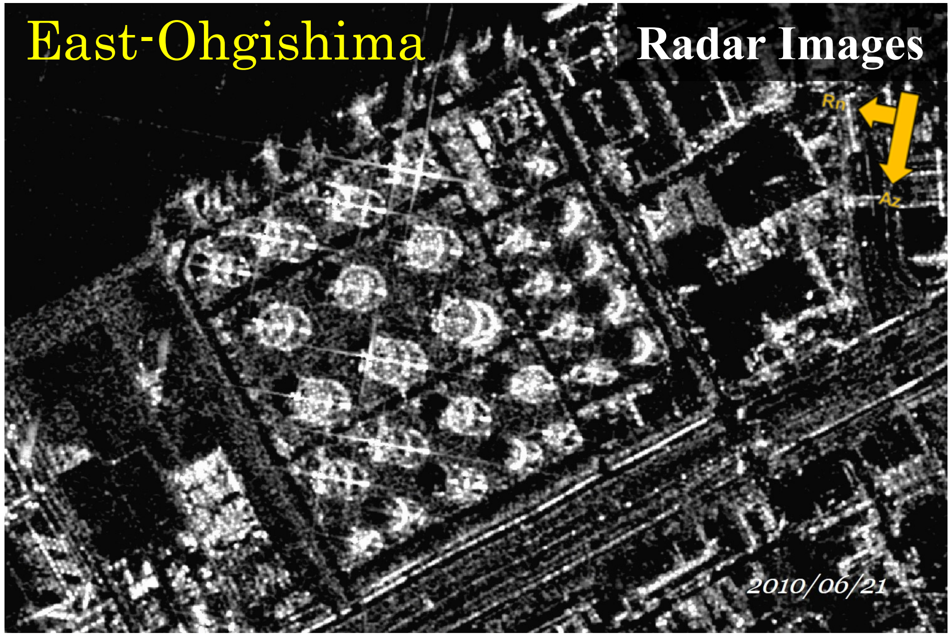

TerraSAR-X images of floating-roof-type oil tanks in Japan

Acquisition : 2010/06/21, 2010/09/06, 2010/11/22

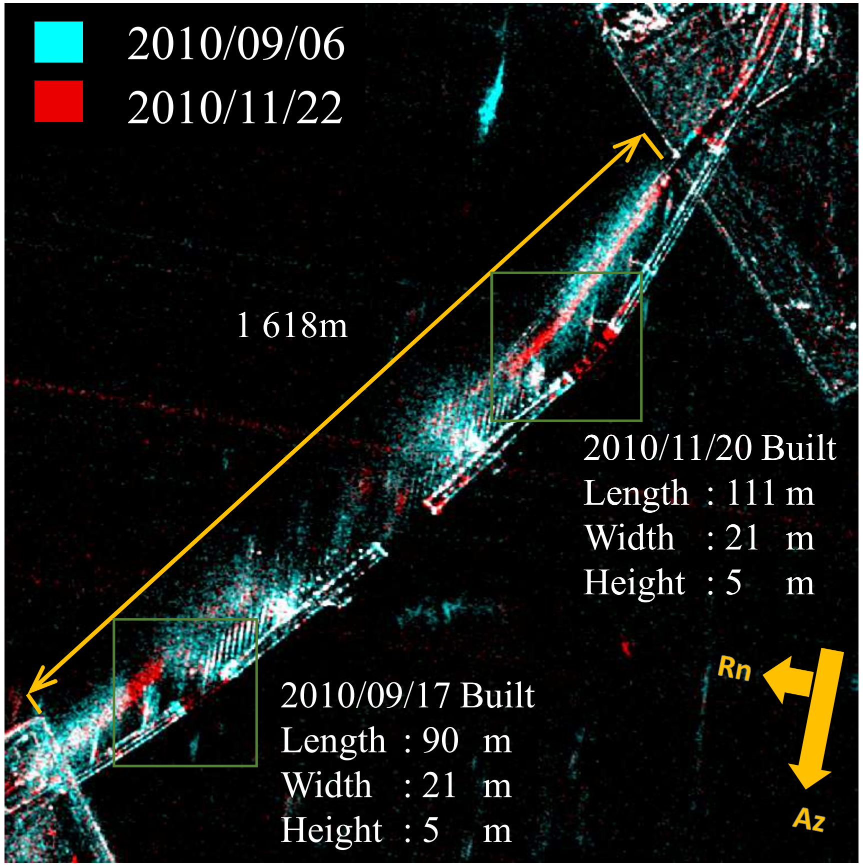
2010/09/06
2010/11/22
1 618m
2010/11/20 Built
Length : 111 m
Width : 21 m
Height : 5 m
2010/09/17 Built
Length : 90 m
Width : 21 m
Height : 5 m
Rn
Az

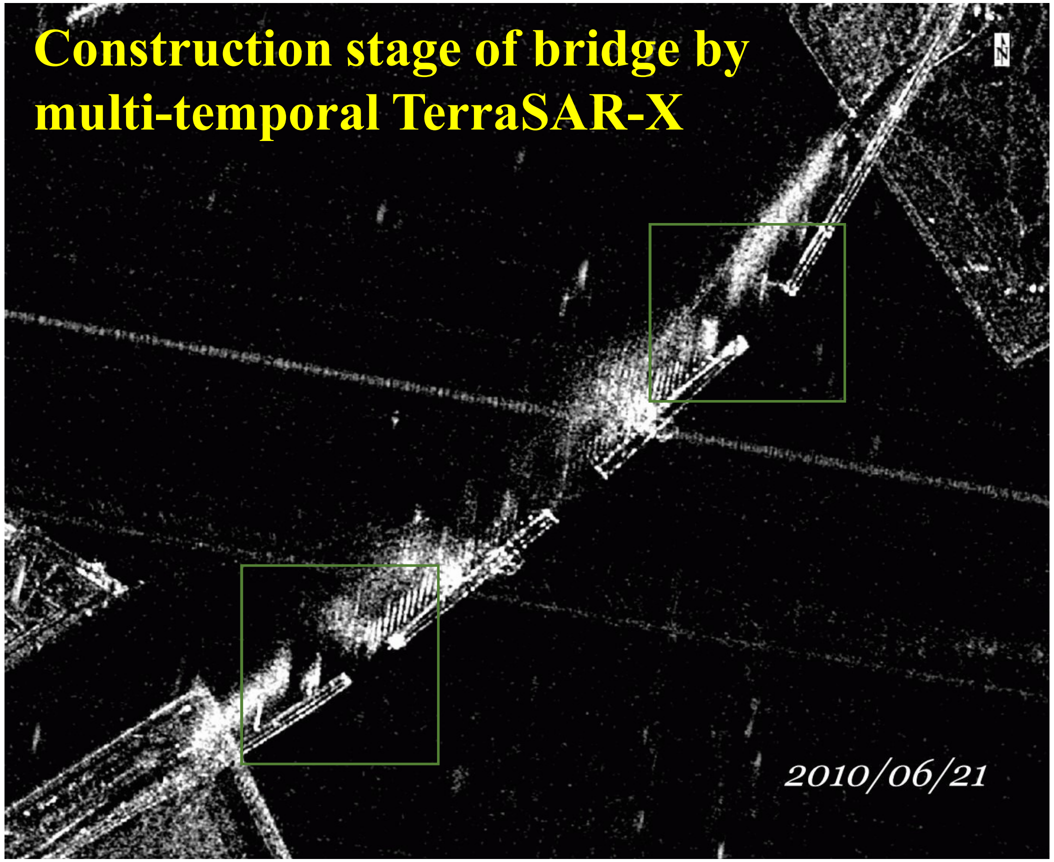
Construction stage of bridge by multi-temporal TerraSAR-X
2010/06/21


Tokyo Gate Bridge, Koto, Tokyo
Rn
Az
Acquisition : 2010/06/21, 2010/09/06, 2010/11/22
Beam ID : strip_013
Orbit Direction : Descending
Imaging Mode : StripMap
Polarization : HH
Look Direction : Right
Antenna Mode : SRA
Resolution(EEC) : 1.25m/pixel

a. Jogawa Bridge (L=126.0m)

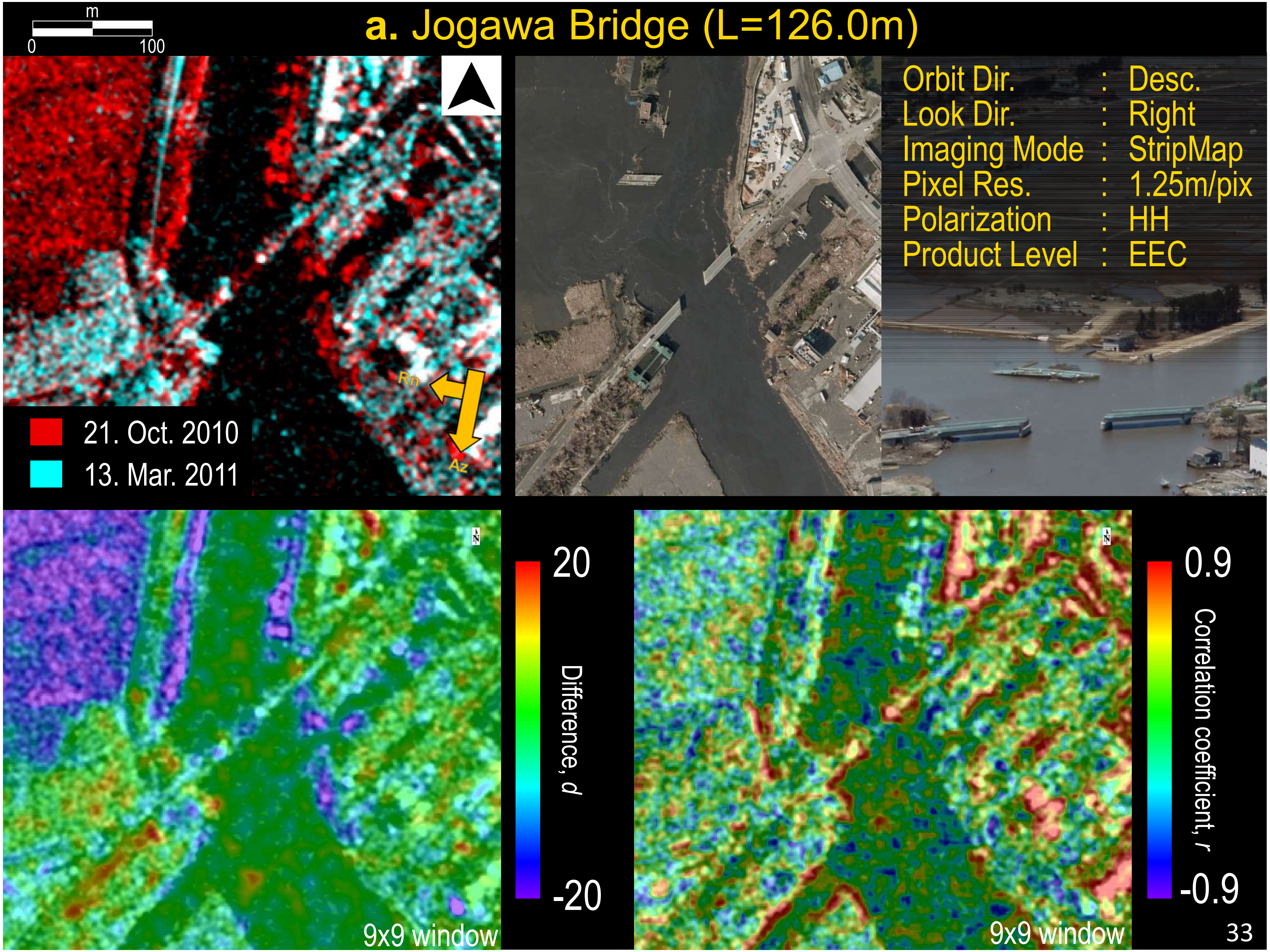

Two Bridges over Naruse River

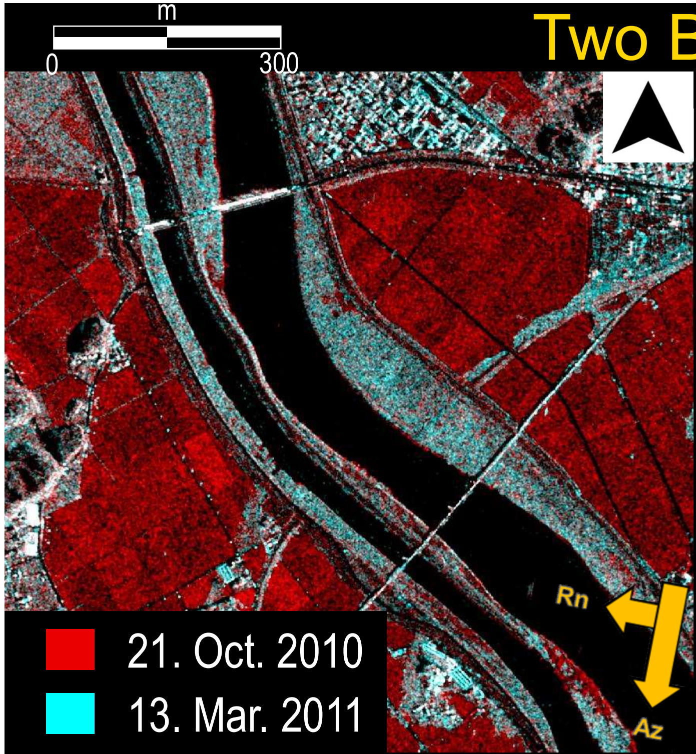

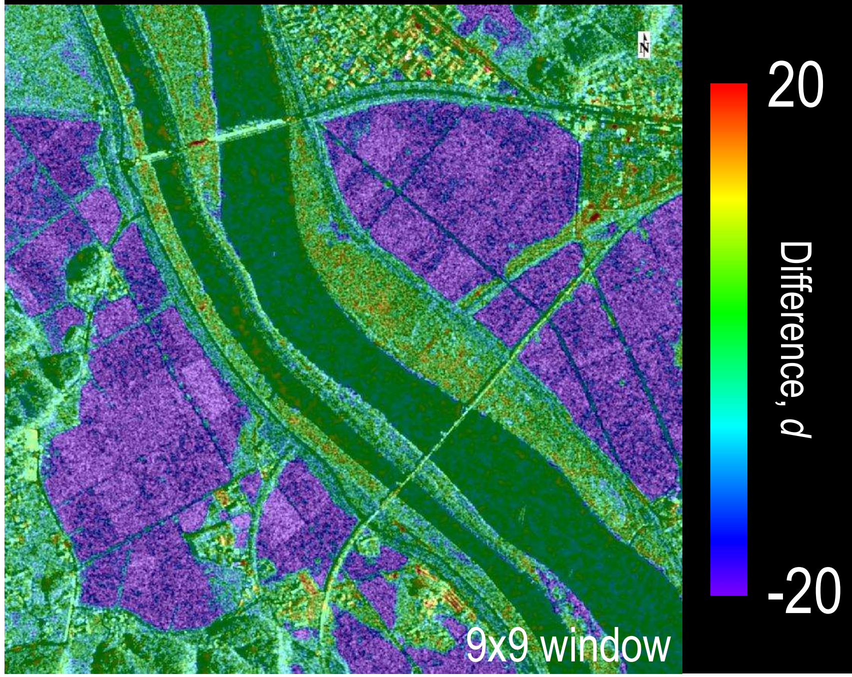

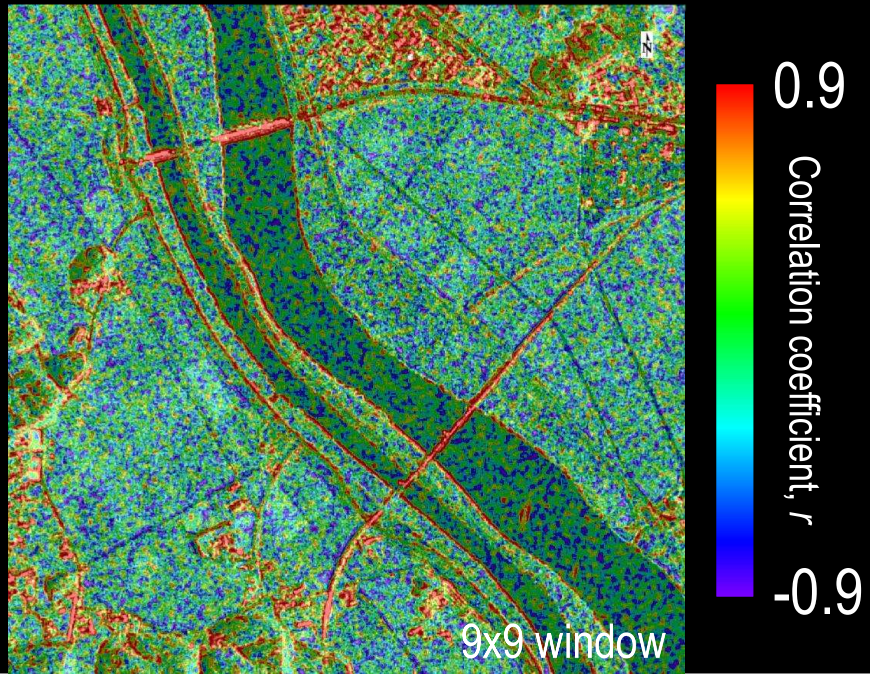

Change Detection for Enlarged Bridge Footprint

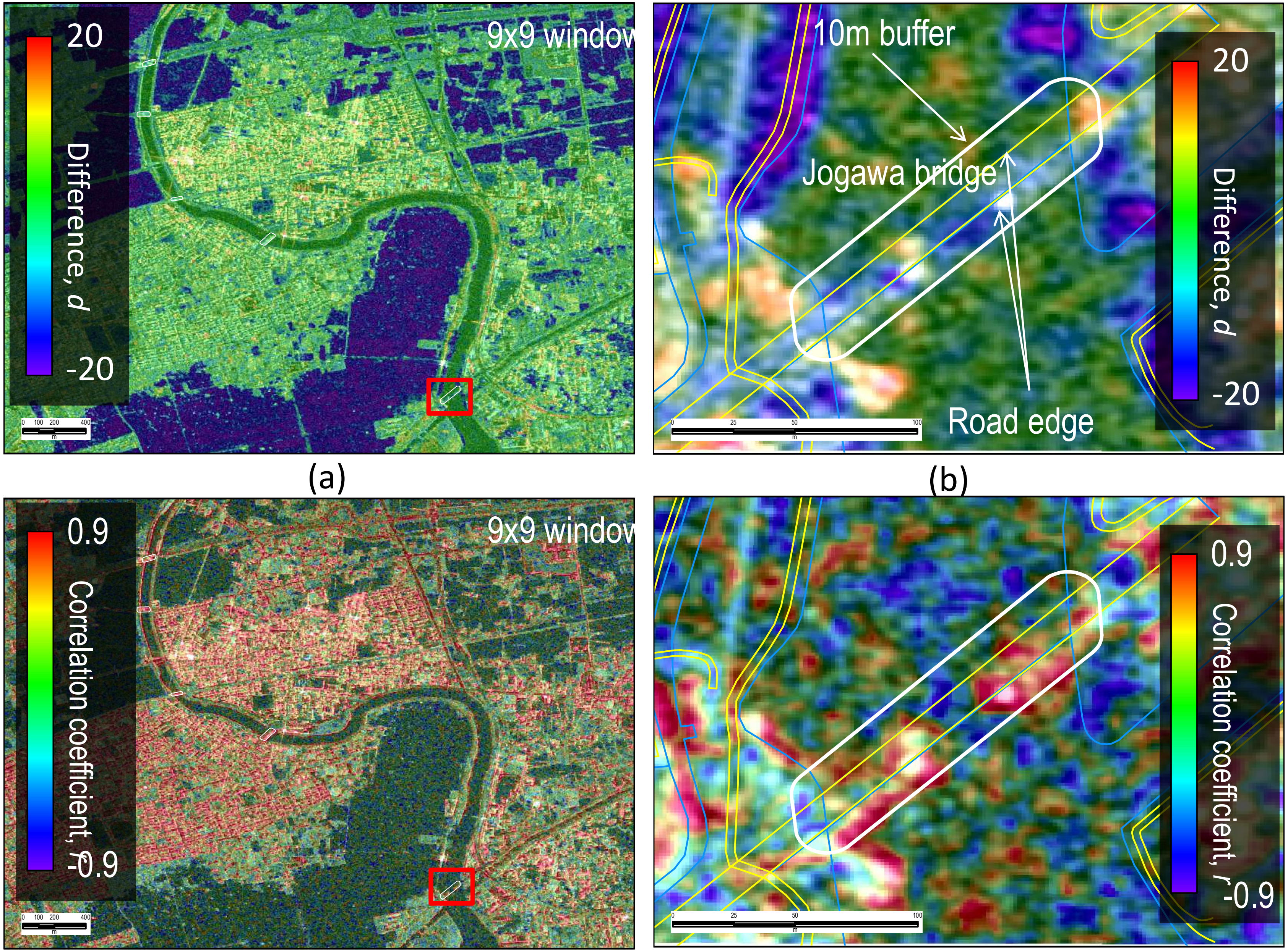

(a) (b) (c) (d)

Relationship between the difference *d* and correlation coefficient *r* (a) and the cumulative probability of *r* when the threshold was set as *r*=0.47 (b) for the 58 bridges

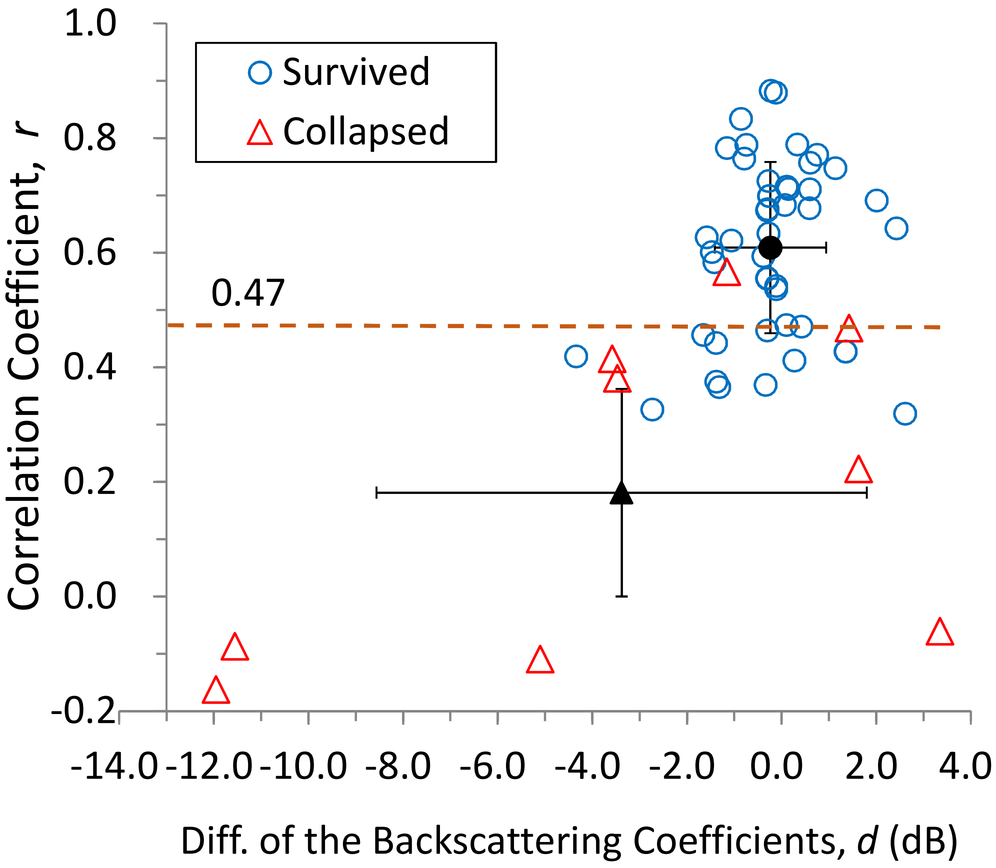

(a)

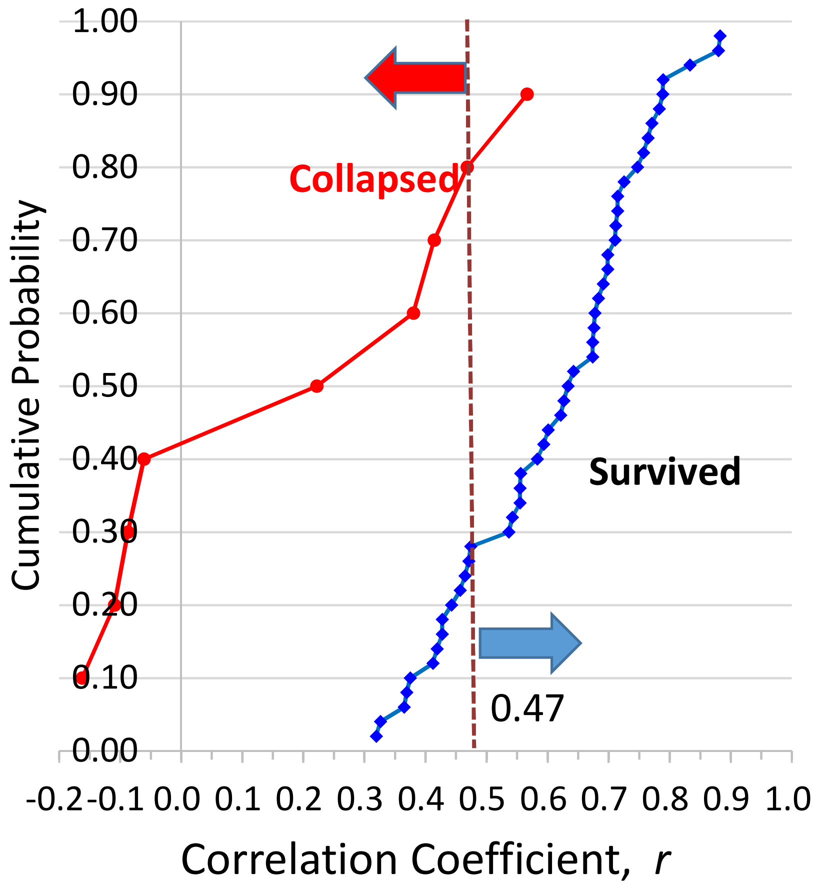

(b)

井上和樹，リュウ・ウェン，山崎文雄， 日本地震工学会論文集，Vol. 17, No. 5, 2017.

Change of the producer accuracies as a function of threshold of *r*

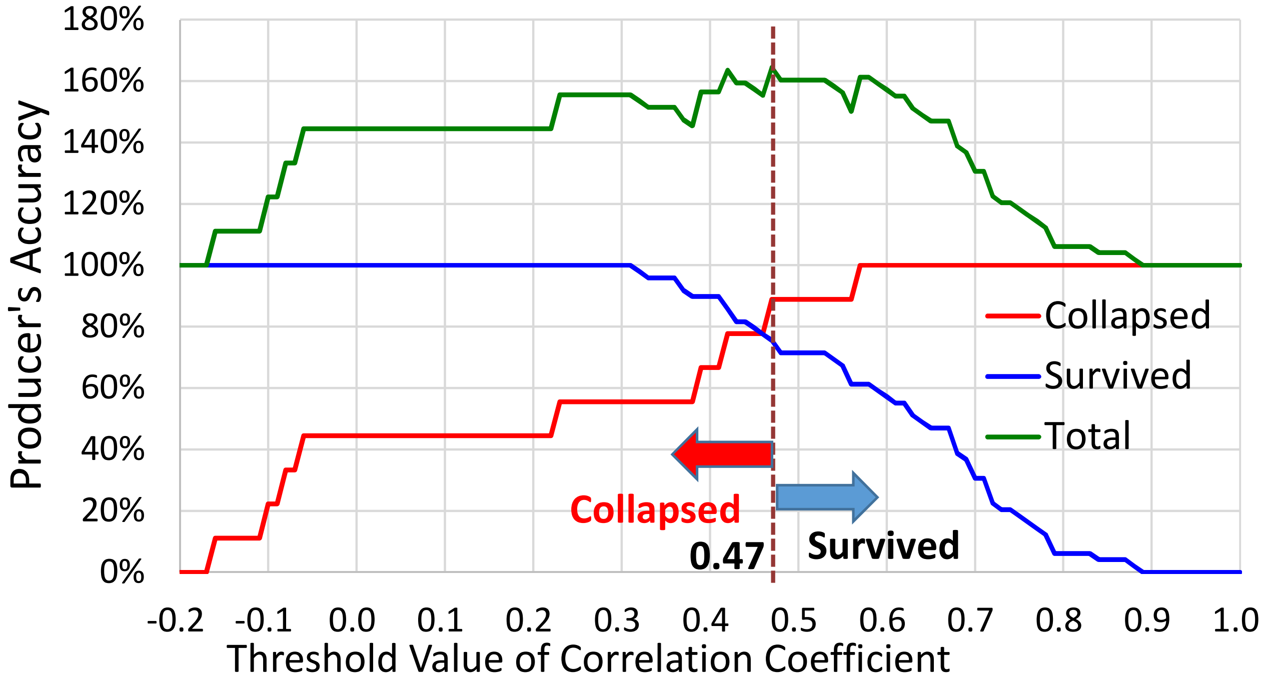

Error Matrix for the threshold r =0.47

		Reference Data			
		Collapsed	Survived	Total	User's Accuracy
SAR Image Interpretation	Collapsed	**8**	12	20	0.400
	Survived	1	**37**	38	0.974
	Total	9	49	**58**	
	Producer's Accuracy	0.889	0.755		
	Overall Accuracy				**0.776**
	Kappa Coefficient				**0.430**

井上和樹，リュウ・ウェン，山崎文雄，日本地震工学会論文集，Vol. 17, No. 5, 2017.

Contents

- Remote Sensing and Disaster Management
- Satellite Optical and Thermal Sensors
- Satellite SAR
- Airborne SAR
- Lidar and UAV

Multi-polarized **Pi-SAR-L2** image for the study area

Natori and Iwanuma cities, Miyagi prefecture, Japan. **JAXA**

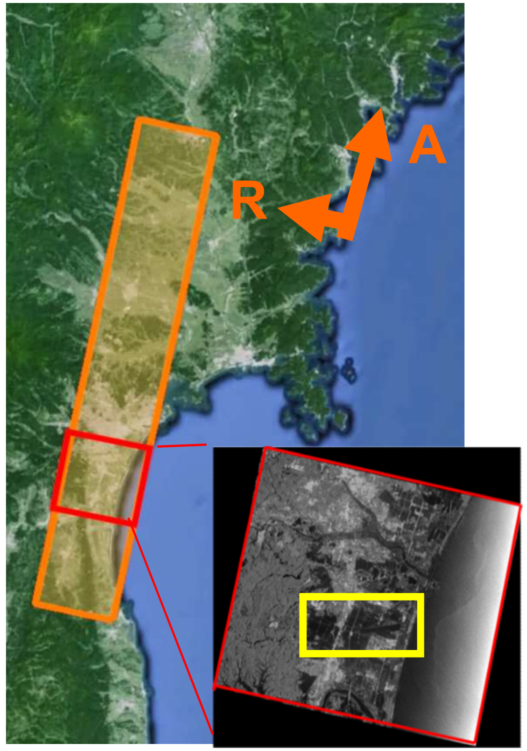

R: HH, **G**: HV, **B**: VV

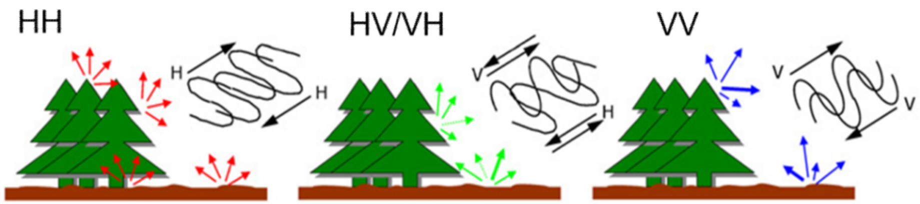

	Pi-SAR-L2
Date	2014/6/12
Band	L-band
Azimuth resolution	1.76 m
Range resolution	3.2 m
Pixel size	2.5 m/pixel
Polarization	HH / HV / VH / VV

Texture measures for the HH-polarized Pi-SAR-L2 image

Gray-Level Co-occurrence Matrix (GLCM)

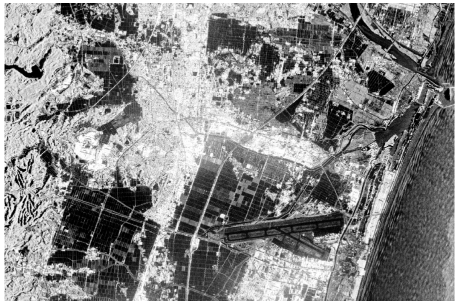

(a) mean

(b) variance

(c) homogeneity

(d) contrast

(e) dissimilarity

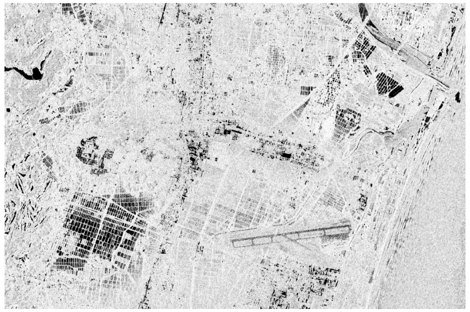

(f) entropy

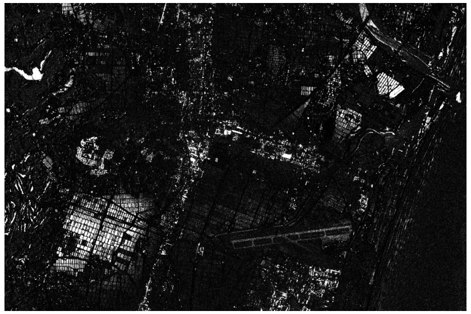

(g) angular second moment

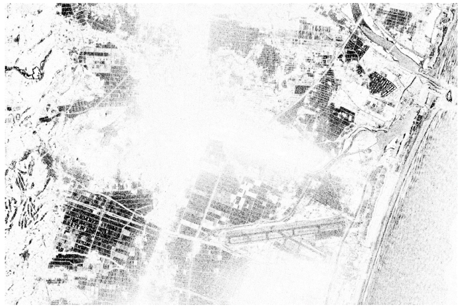

(h) correlation

Eight textural features in angle 0º
Distance 1
Window size of 9 x 9
using ENVI software

Original Image

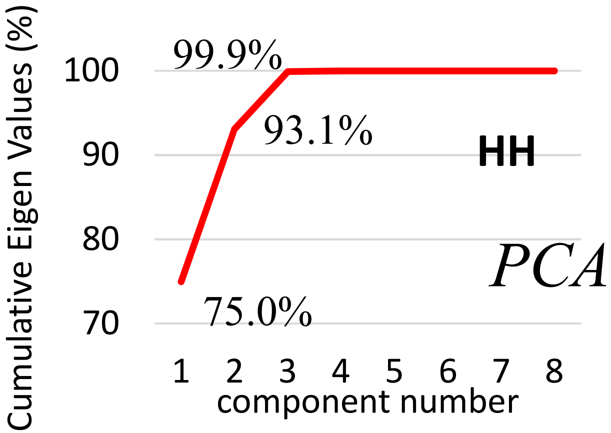

Object-based supervised land-cover classification result

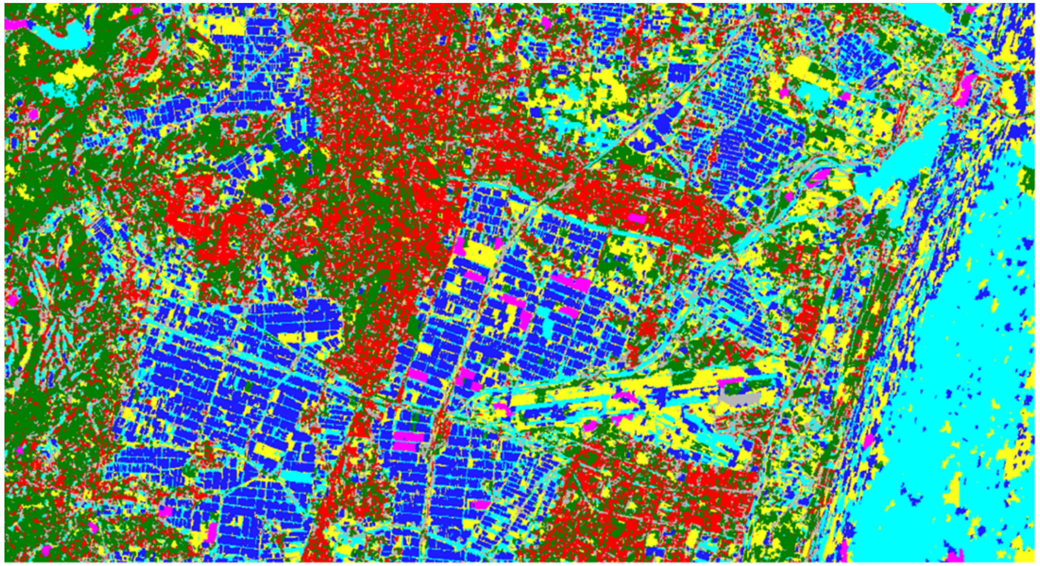

Original HH and HV pols.

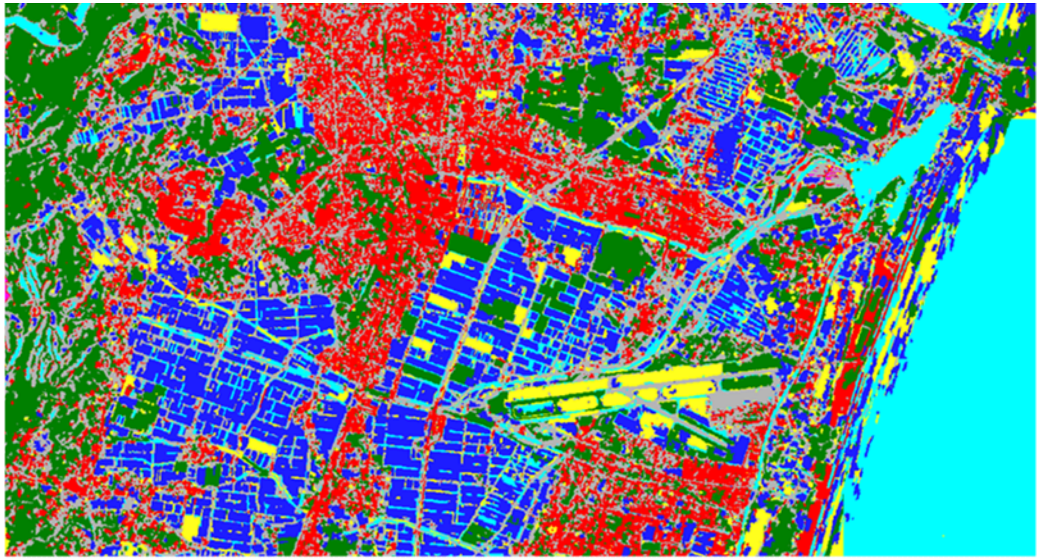

Original HH and HV + **5 PC textures** (95.5 %)

- Water and roads are difficult to classify.
- False positive errors for solar panels.
- The results are similar for 5 PCs and 8 PCs textures.

→ 95 % cumul. Eigenvalue is enough.

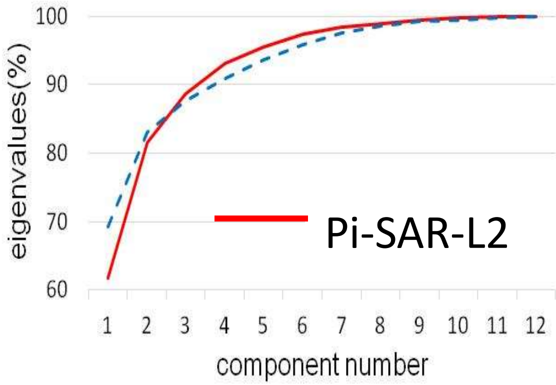

F. Yamazaki, N. Samuta, W. Liu, PIERS, 2017.

Pi-SAR2 (X2) flight after the 2016 Kumamoto EQ by NICT

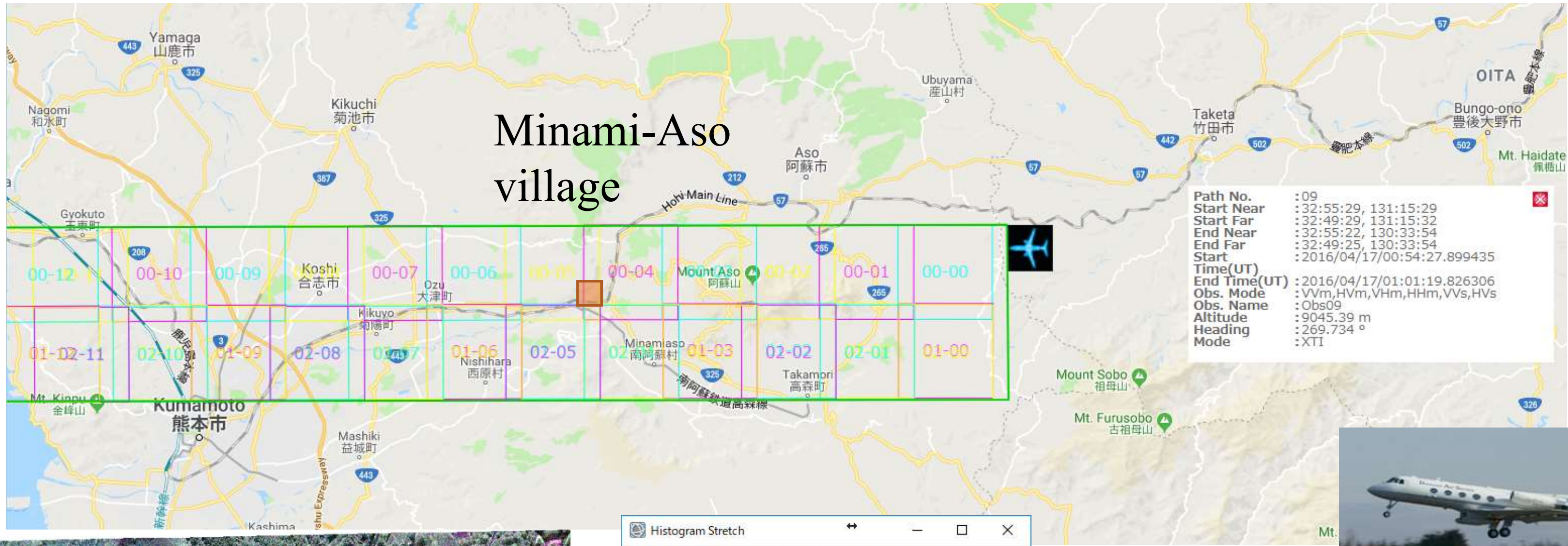

Polarimetric and Interferometric Airborne SAR (Pi-SAR-X2)

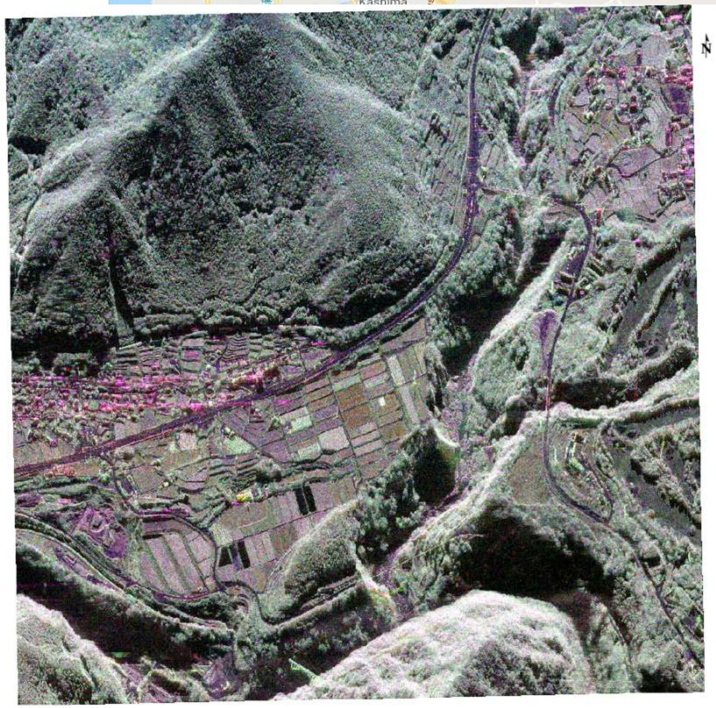

R : HH, G : HV, B : VV

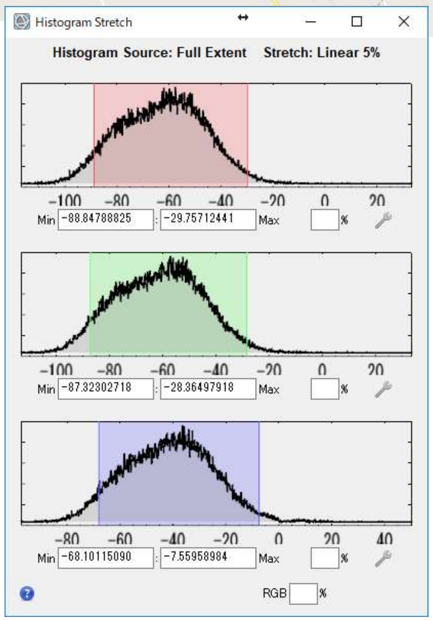

Enhanced Lee Filter : 3 × 3

$$\sigma^0 = 10\log(|DN|^2) + A$$

Date	Height (m)	Heading
2015.12. 5	8981 m	-91.3°
2016. 4.17	9027 m	-90.3°

Resolution (m): 0.3 (A) x 0.3 (R)
Pixel size (m): 0.25 x 0.25

4-component scattering power decomposition (G4U)

Minami-Aso village

Singh et al. (2013)

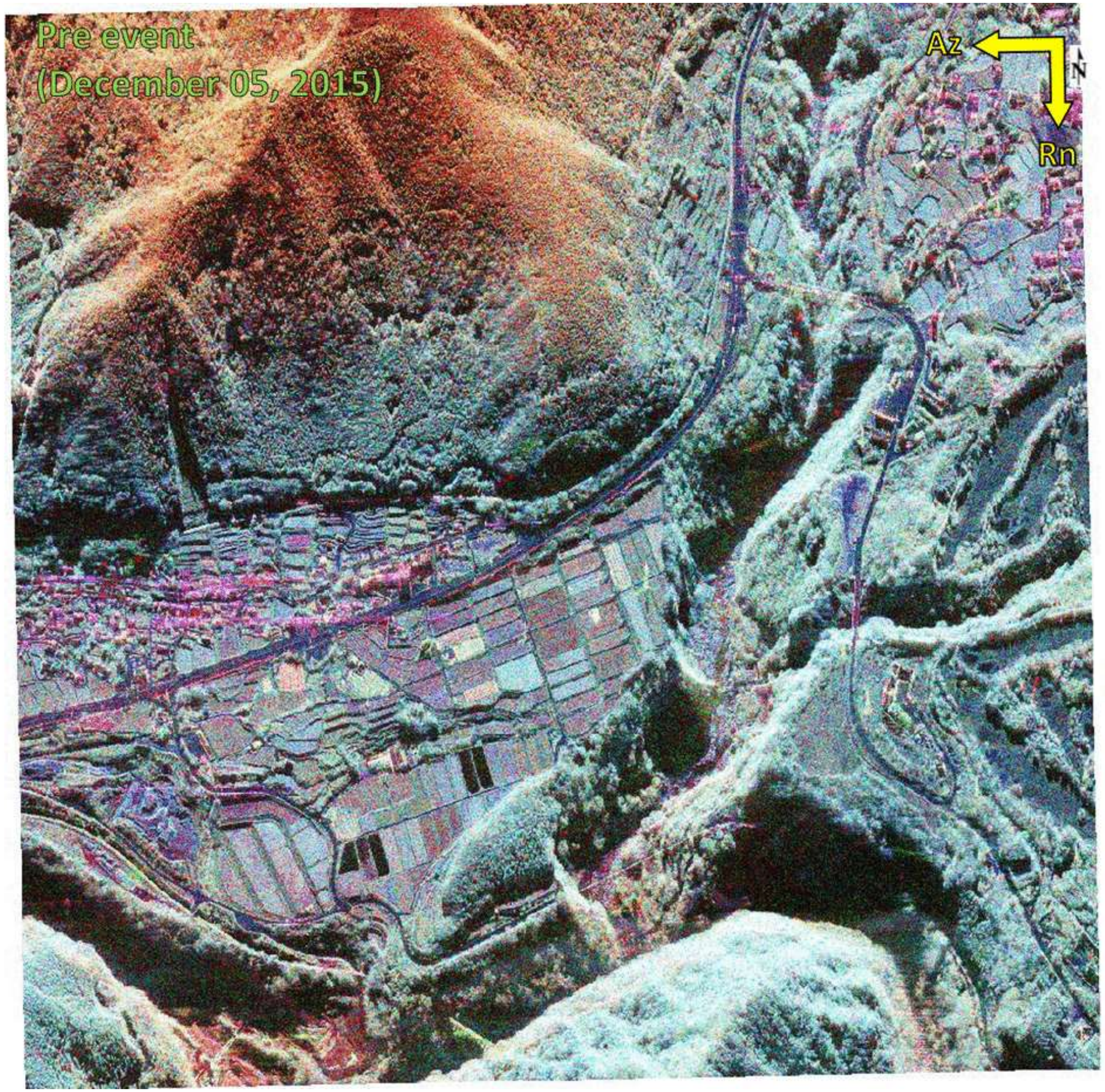

R: σ_d G: σ_v B: σ_s

HH pol
HV pol.
VH pol.
VV pol.

$$[S] = \begin{bmatrix} S_{HH} & S_{HV} \\ S_{VH} & S_{VV} \end{bmatrix}$$

Surface scattering (**Ps**)
Double-bounce scat. (**Pd**)
Volume scattering (**Pv**)
Helix scattering (**Pc**)

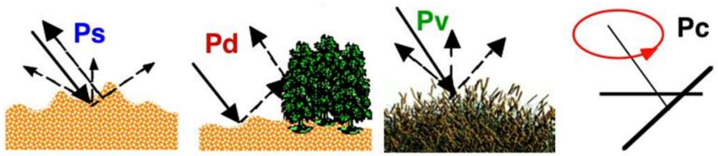

PolSAR pro 5.1

Comparison of aerial photo and Pi-SAR2 color composite for low-damage areas

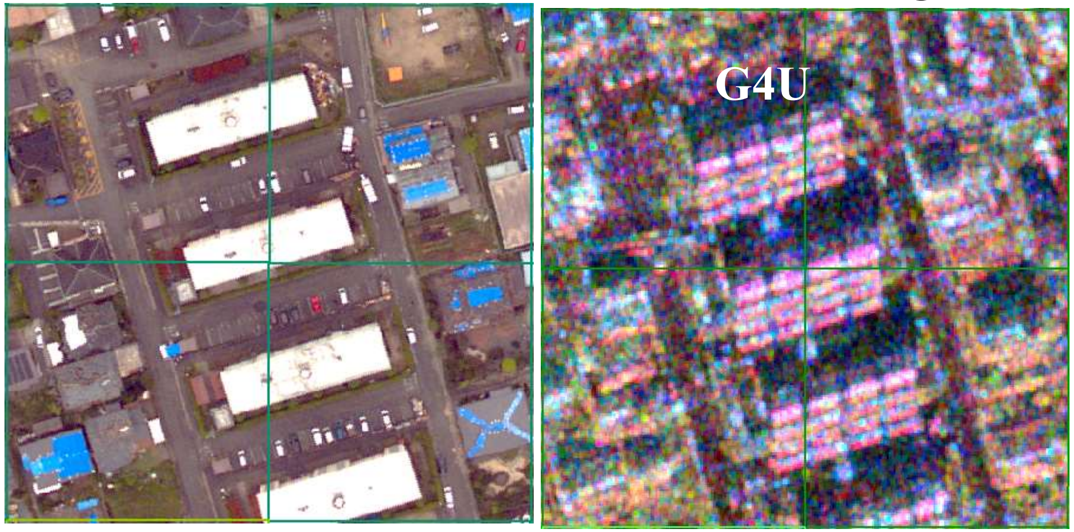

(a) Low collapsed ratio area with RC buildings

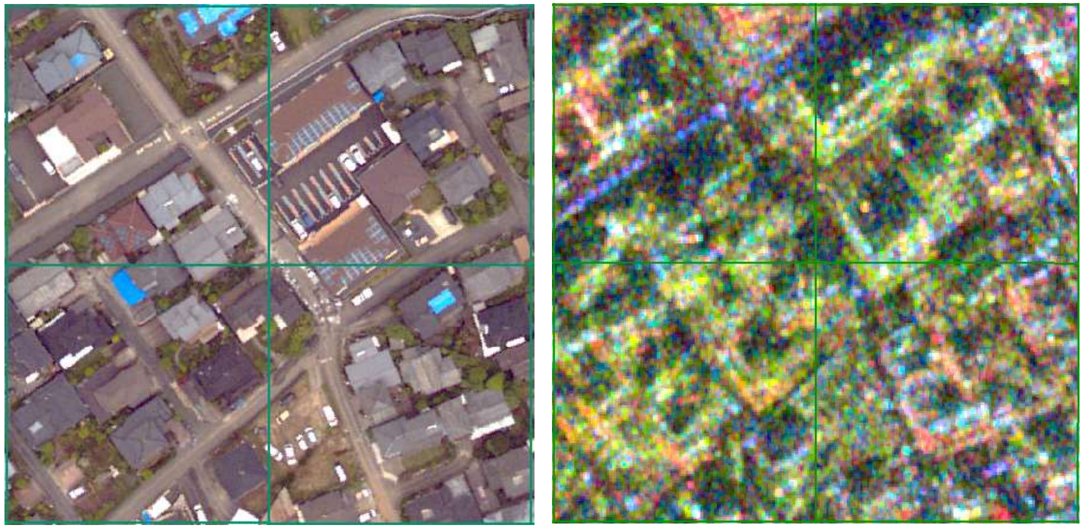

(b) Low collapsed ratio area with wooden houses

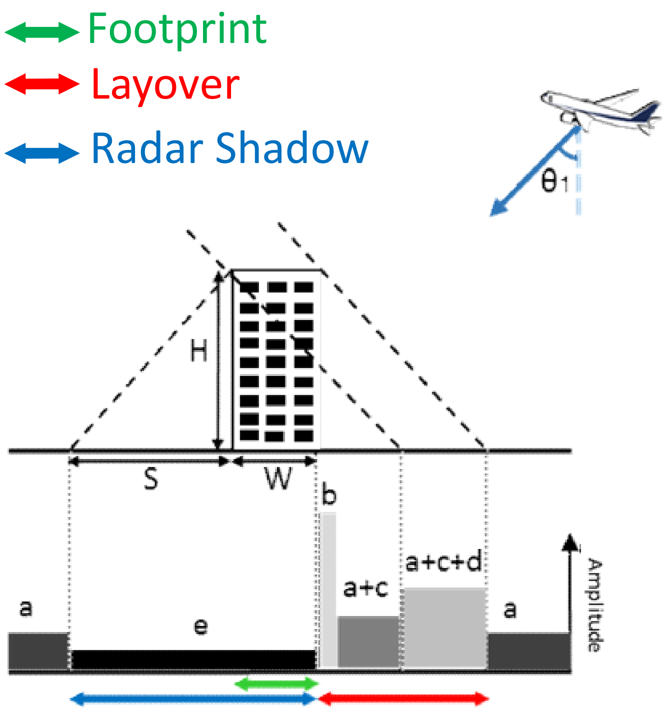

F. Yamazaki, W. Liu, S. Kojima, US-NCEE, 2018.

Comparison of aerial photo and Pi-SAR2 color composite (center) for high-damage areas

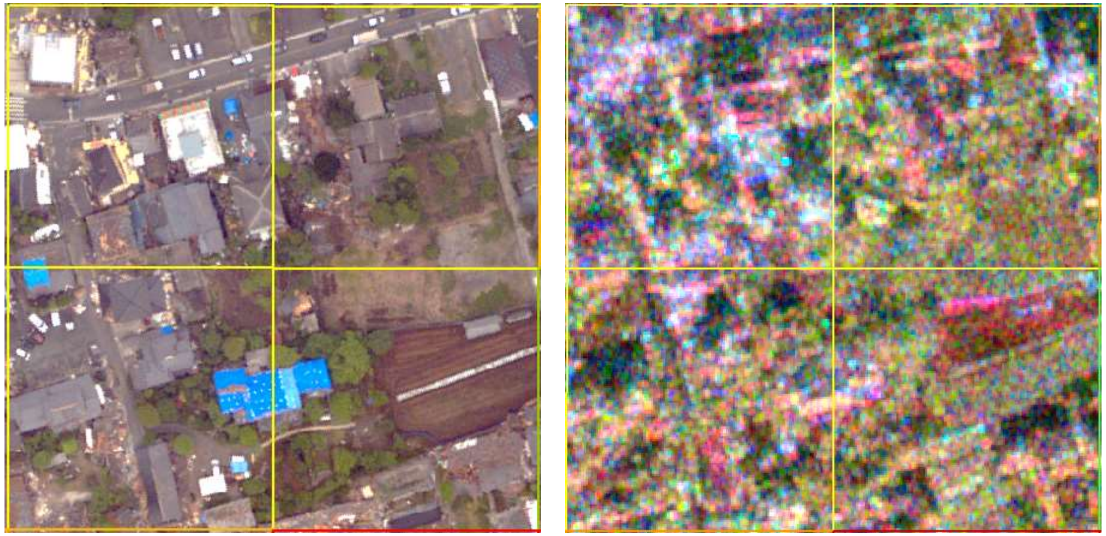

(c) high collapsed ratio area ($R_c \geq 40$ %)

(d) high collapsed ratio area ($R_c \geq 60$ %)

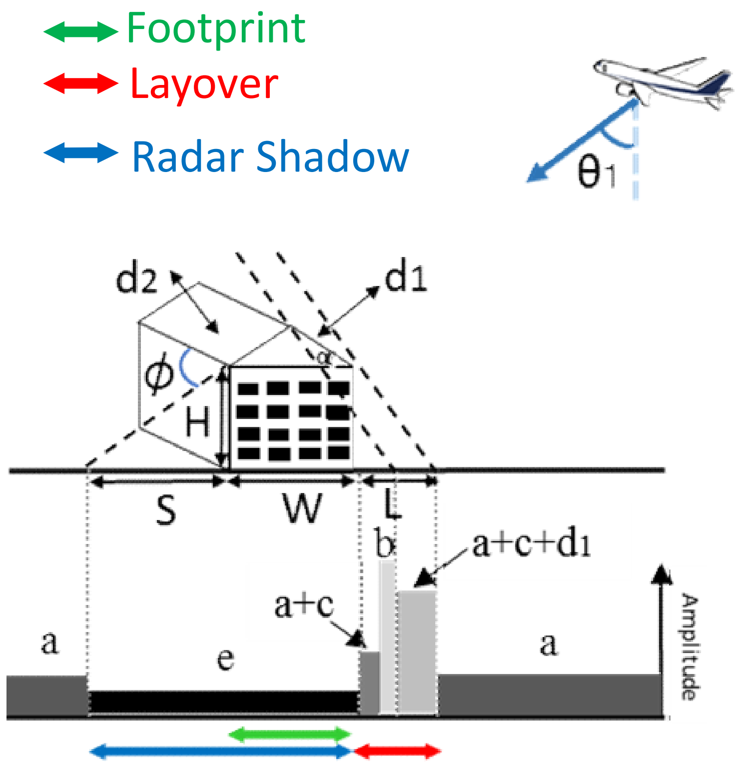

Airborne Pi-SAR-X2 images for bridges in central Tokyo

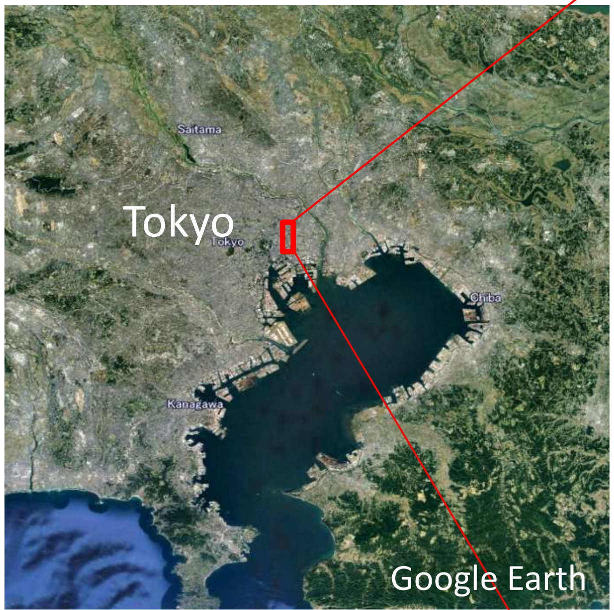

R:HH
G:HV
B:VV

NICT, Japan

Polarimetric and Interferometric Airborne SAR (Pi-SAR-X2)

Date	22 December, 2009	10 January, 2013
Incident angle (°)	42.2 (center)	44.3 (center)
Pixel size (m)	0.25 × 0.25 (Az × Rn)	0.25 × 0.25 (Az × Rn)
Azimuth angle (°)	2.06	-90.1

Effect of illumination angle φ to the bridge axis

In addition to the structural types, the backscattering characteristics of bridges also change according to the illumination angle

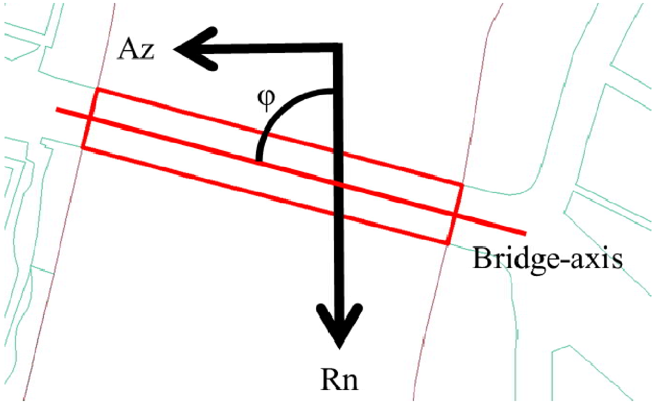

φ : The illumination angle between the bridge-axis and the range-direction

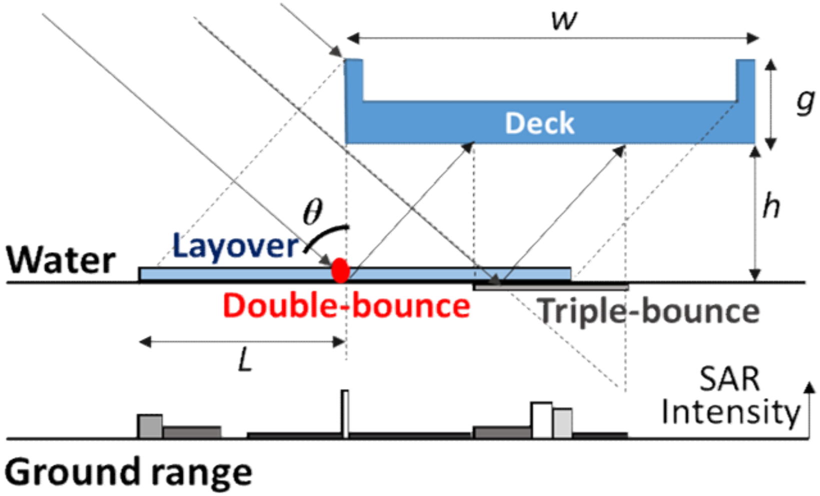

R:Pd
G:Pv
B:Ps

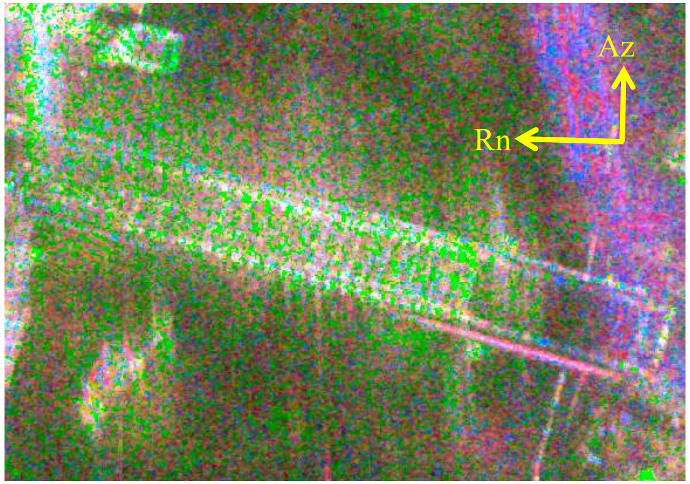

φ=12° (22 December, 2009)

R:Pd
G:Pv
B:Ps

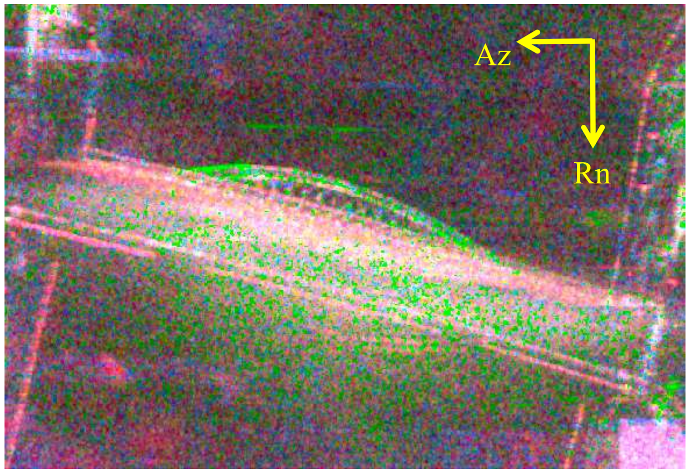

φ=76° (10 January, 2013)

Liu and Yamazaki (2018) Journal of Disaster Research,

Pi-SAR-X2 images of Girder bridge and Upper-arch bridge

Bridge (No.)	φ (°)	R:HH G:HV B:VV	R:Pd G:Pv B:Ps
No. 3 Girder bridge	8	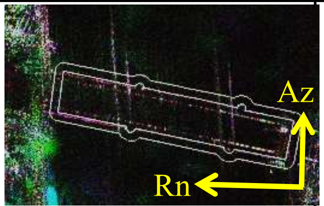	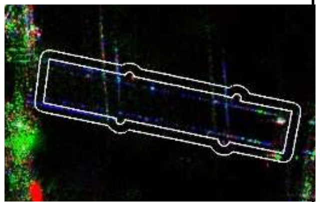
	80	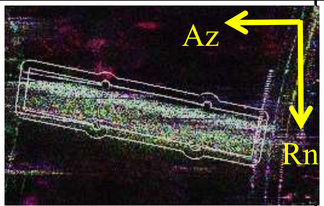	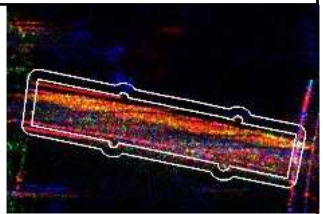
No. 2 Upper arch bridge	22	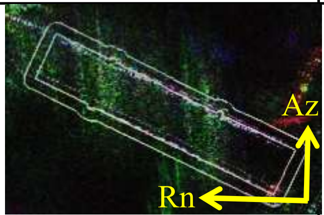	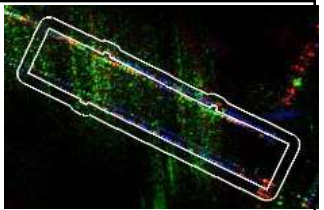
	66	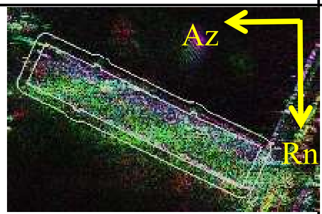	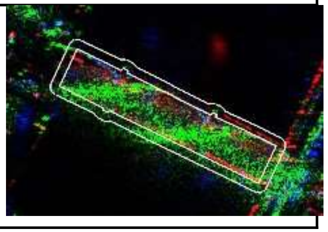

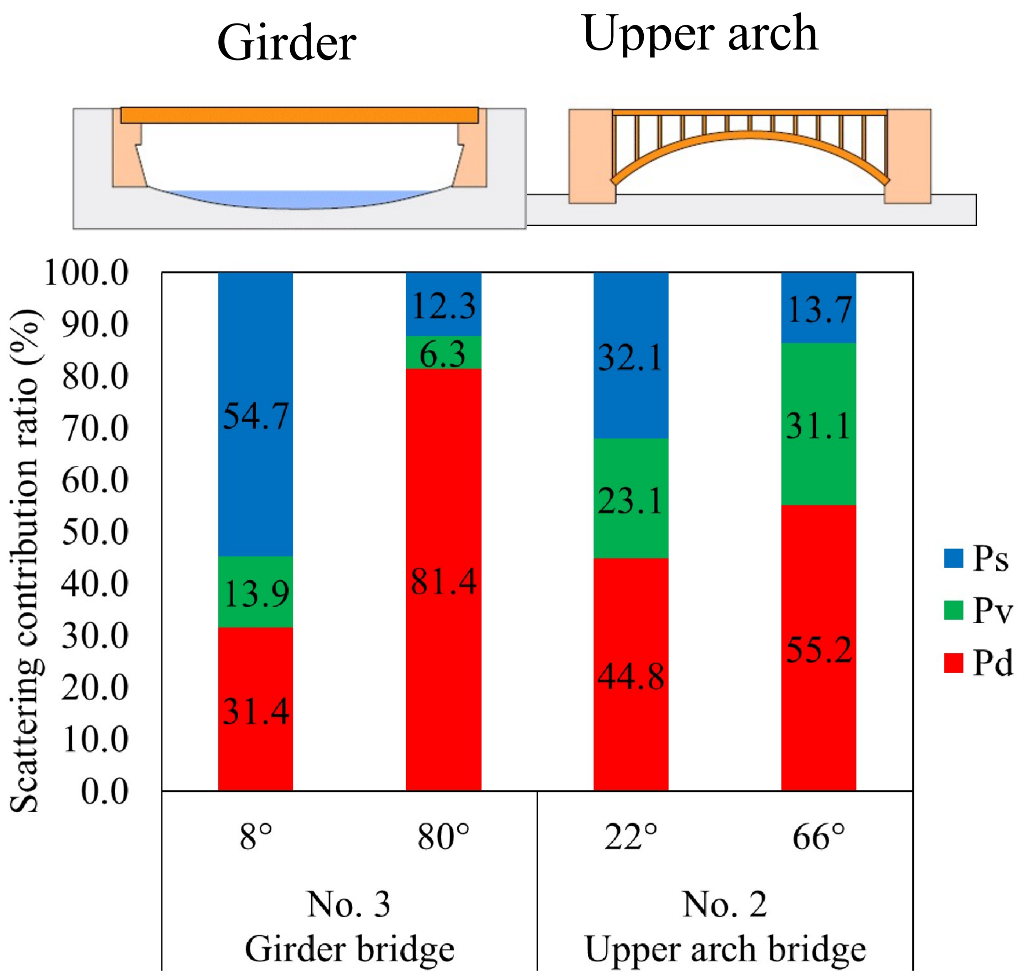

- Girder bridge : φ →90° **Pd** ⬆ **Ps** ⬇
- Upper arch : φ →90° **Pd** ⬆ **Ps** ⬇

H. Hirano, F. Yamazaki, W. Liu, *ACRS*, 2018.

Pi-SAR-X2 data used in this study

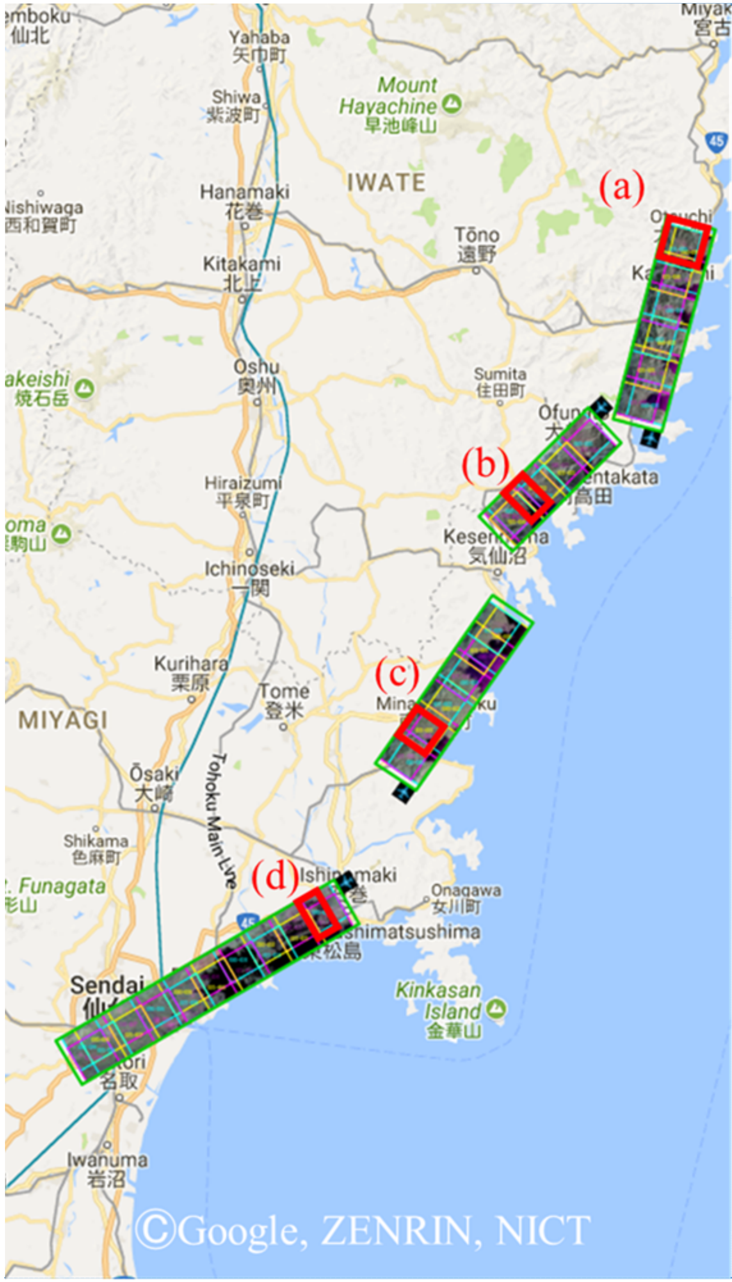

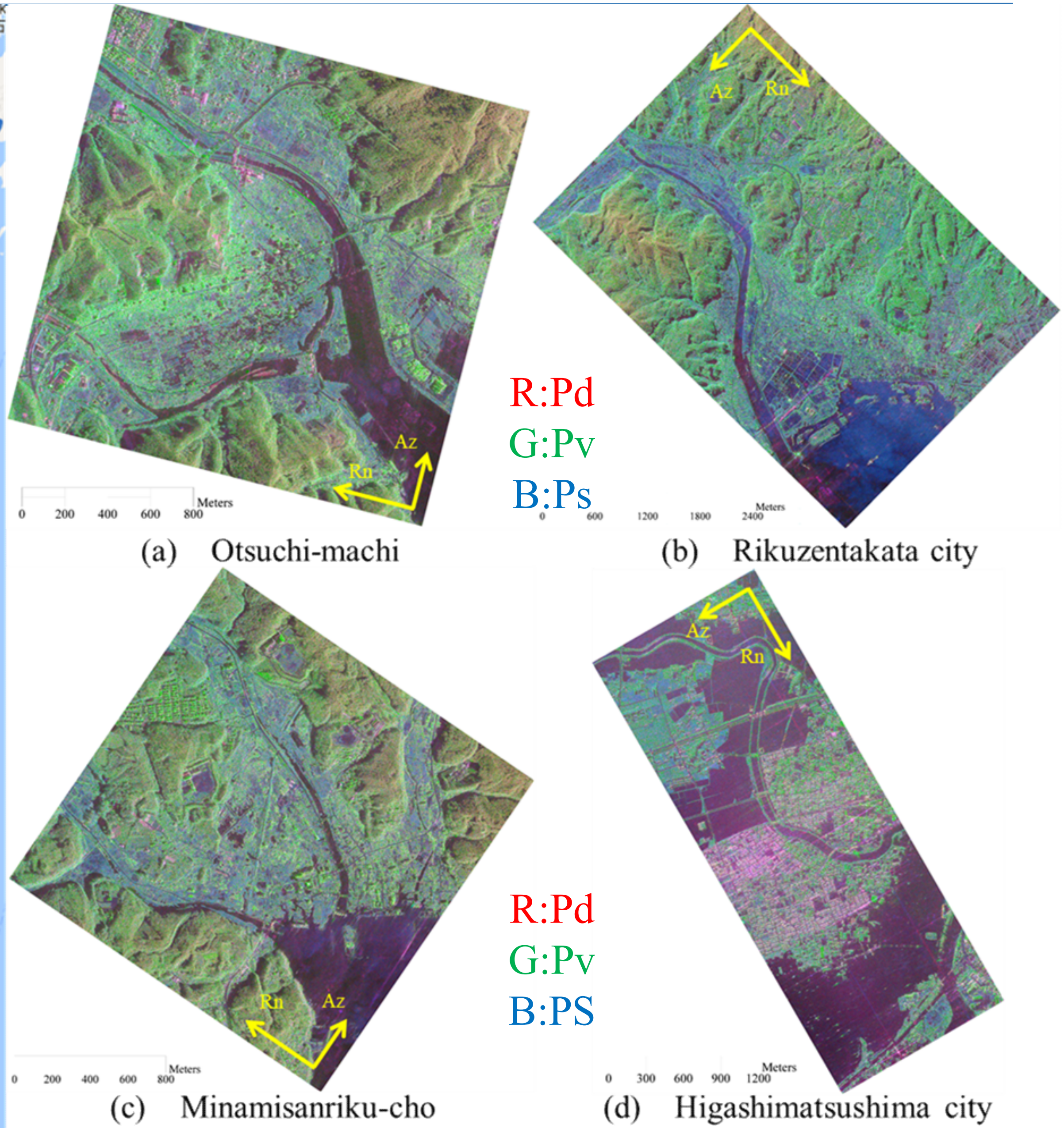

(a) Otsuchi-machi (b) Rikuzentakata city (c) Minamisanriku-cho (d) Higashimatsushima city

H. Hirano, F. Yamazaki, W. Liu, *ISRS*, 2018.

Washed away

No.	R:Pd G:Pv B:Ps (Sigma naught)	Google Earth Before	GSI map Soon after
101	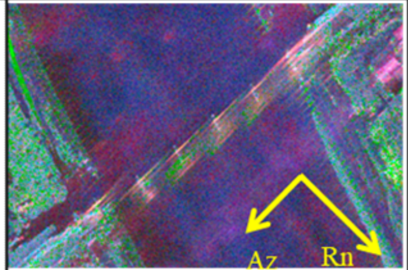		
103	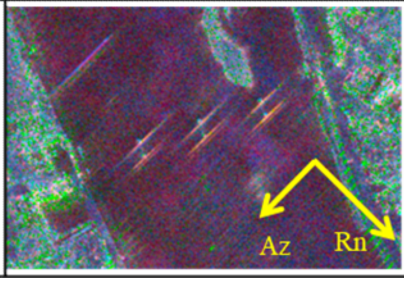		

Survived with debris

No.	R:Pd G:Pv B:Ps (Sigma naught)	Google Earth Before	GSI map Soon after
96	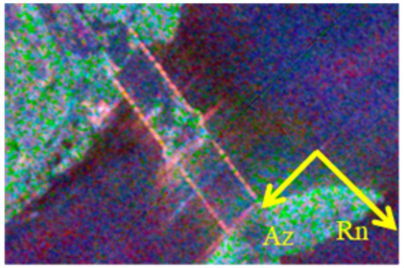		
124	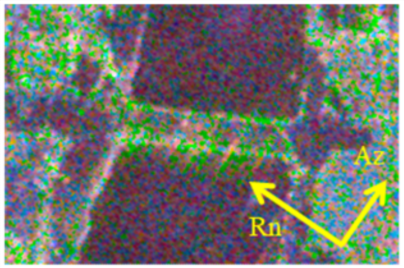		

Contents

- Remote Sensing and Disaster Management
- Satellite Optical and Thermal Sensors
- Satellite SAR
- Airborne SAR
- Lidar and UAV

Epicenters, faults, and GPS stations in the 2016 Kumamoto EQ

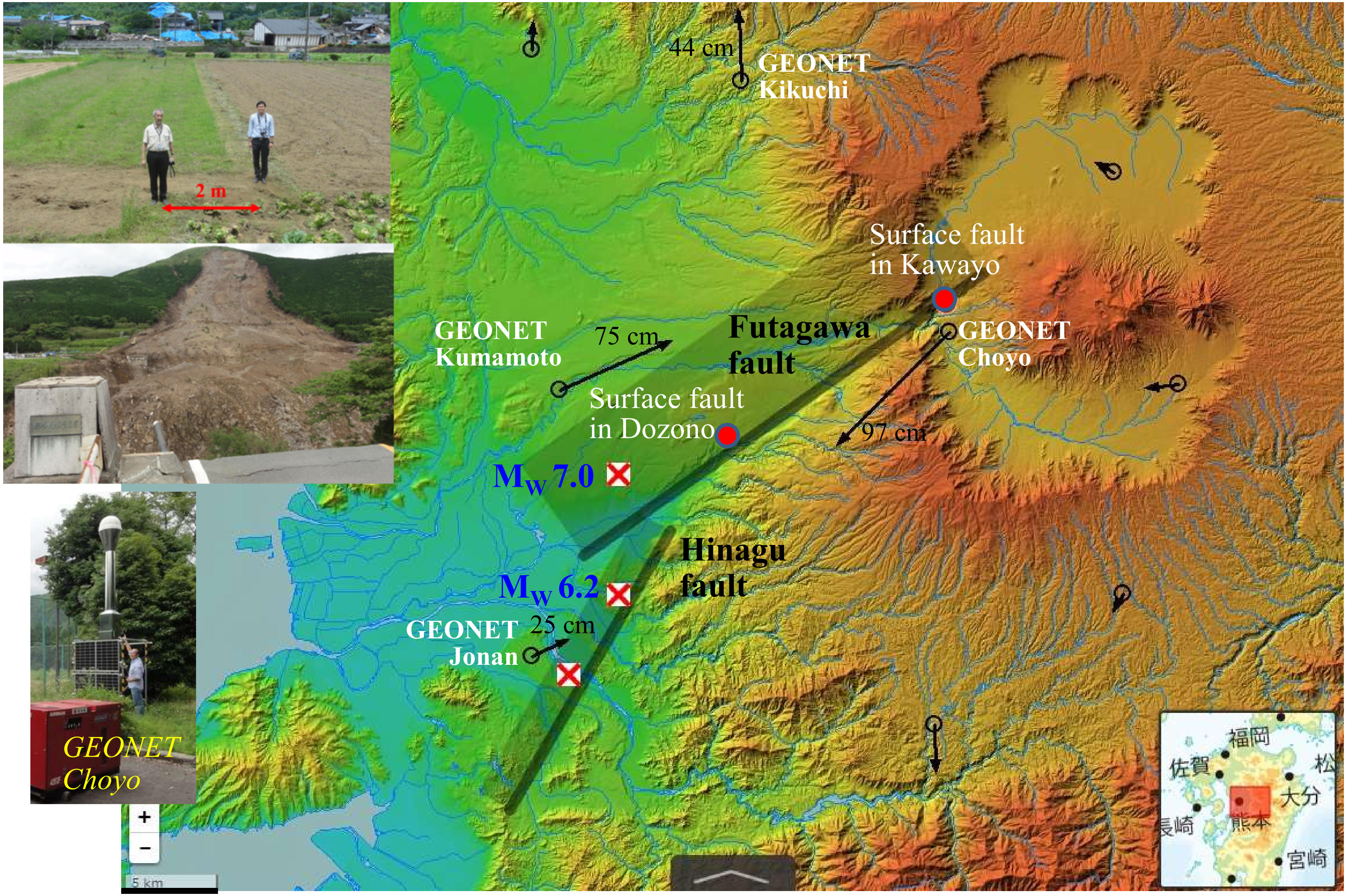

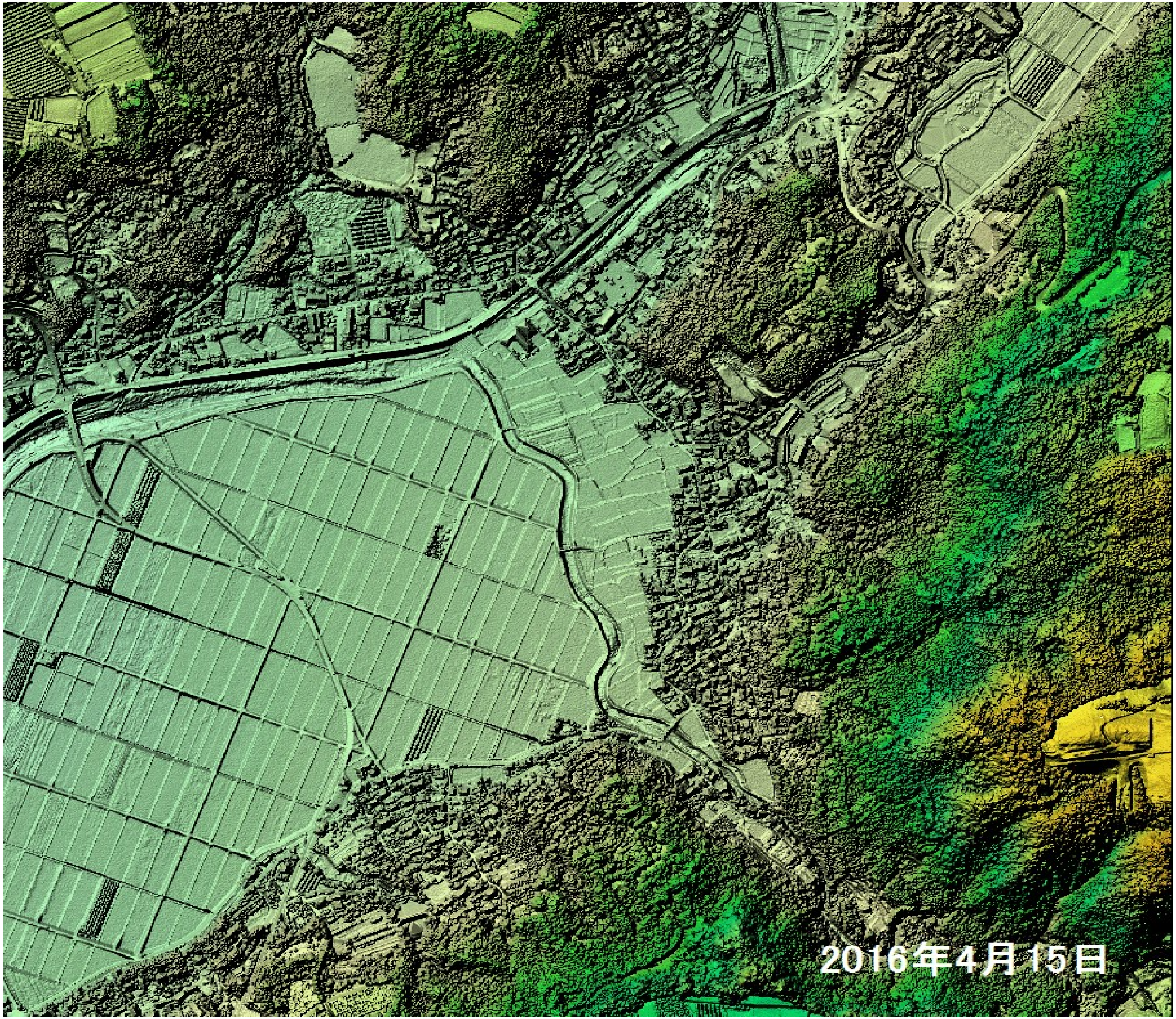
2016年4月15日

Estimation of 3D coseismic displacement from LiDAR DSMs in the main-shock of the Kumamoto EQ

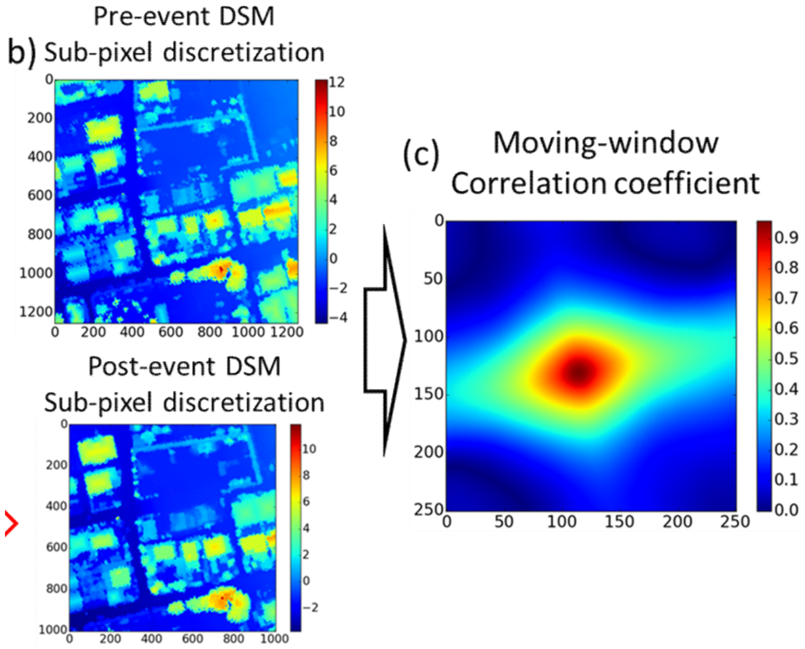

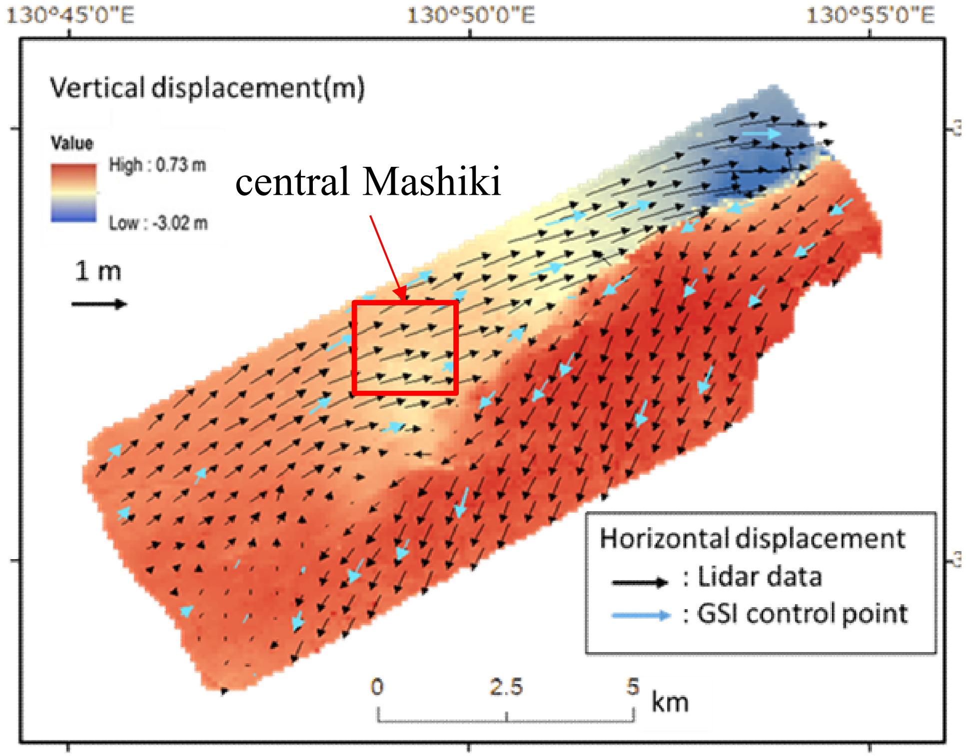

Maximum cross-correlation to determine crustal movements from LiDAR DSMs
By 100 m grid cells

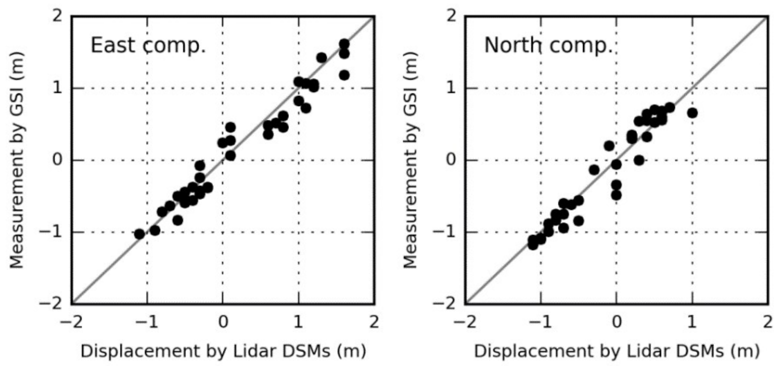

Moya, L., Yamazaki, F., Liu, W., and Chiba, T.: Calculation of coseismic displacement from lidar data in the 2016 Kumamoto, Japan, earthquake, Nat. Hazards Earth Syst. Sci. 17, 143-156, 2017

Extraction of **collapsed buildings** and **landslide** by the difference of **LiDAR** Digital Surface Models (DSMs)

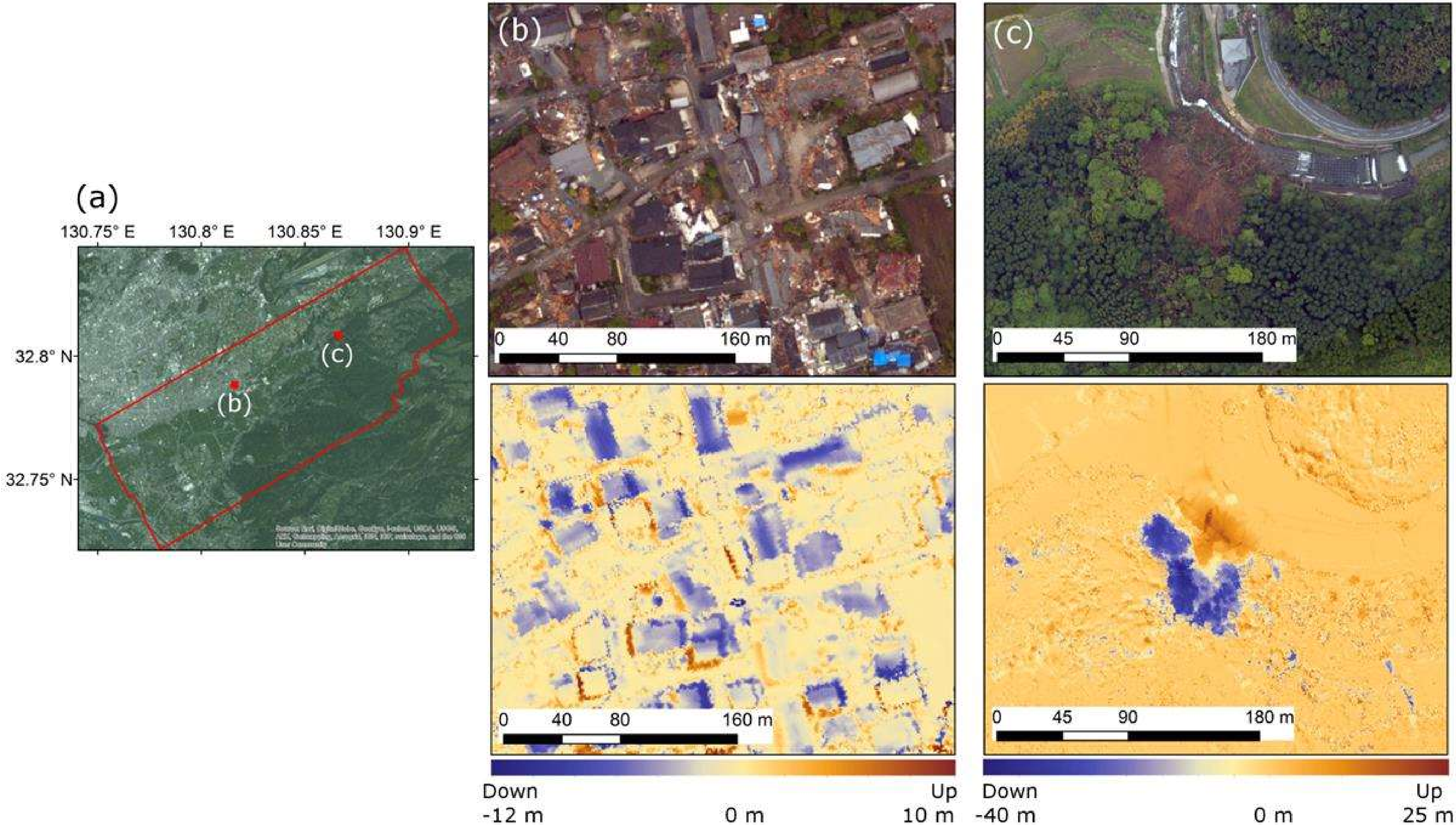

F. Yamazaki, W. Liu, Remote sensing technologies for post-earthquake damage assessment: A case study on the 2016 Kumamoto earthquake, 6th Asia Conference on Earthquake Engineering, 2016.

Extraction of collapsed buildings using two DSMs' height difference after removing crustal movements

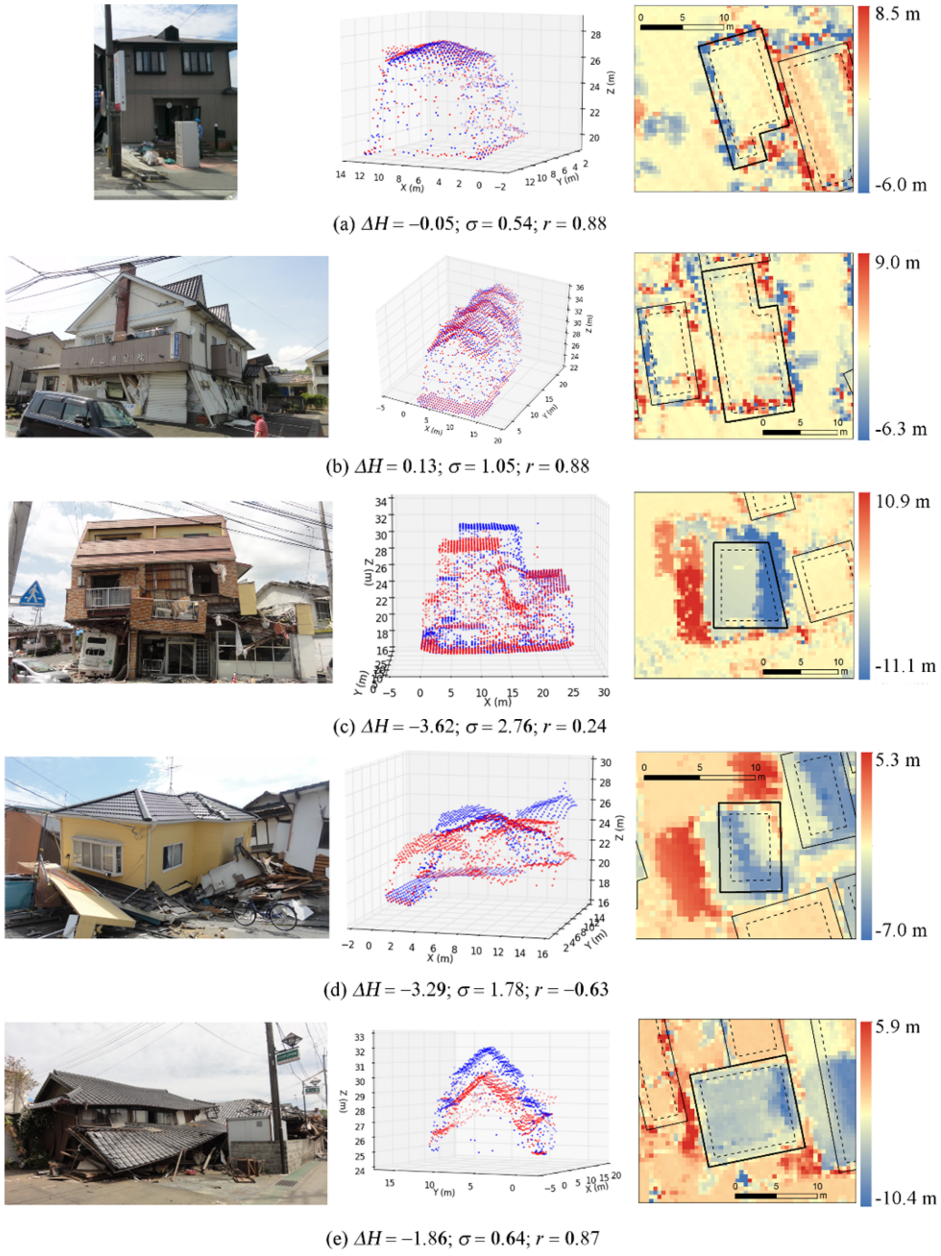

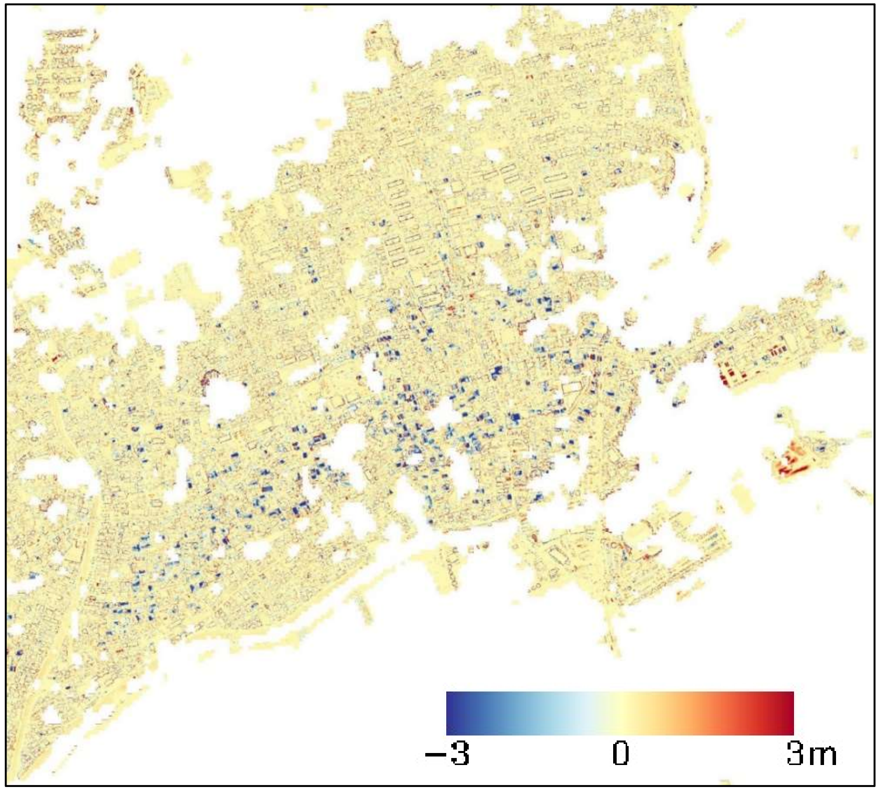

Difference of the two DSMs

L. Moya, F. Yamazaki, W. Liu, M. Yamada, Detection of collapsed buildings from lidar data due to the 2016 Kumamoto earthquake in Japan, NHESS, 2018.

Location (a) and color-composite (b) of ALOS-2 PALSAR-2 images

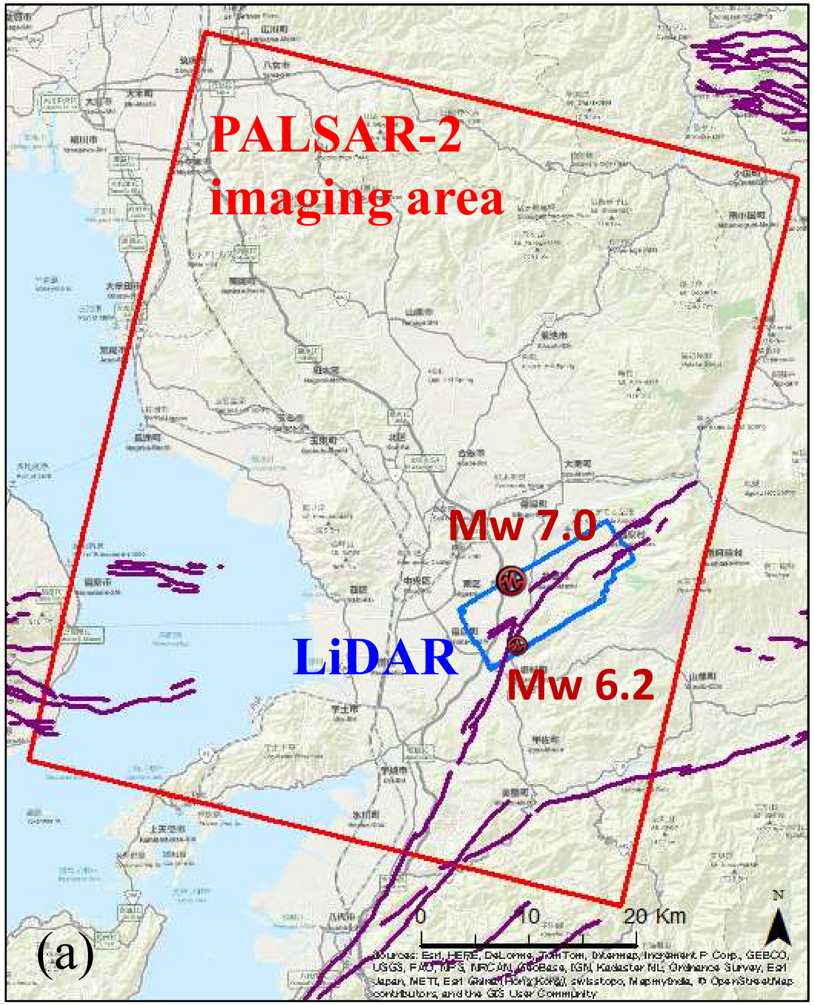

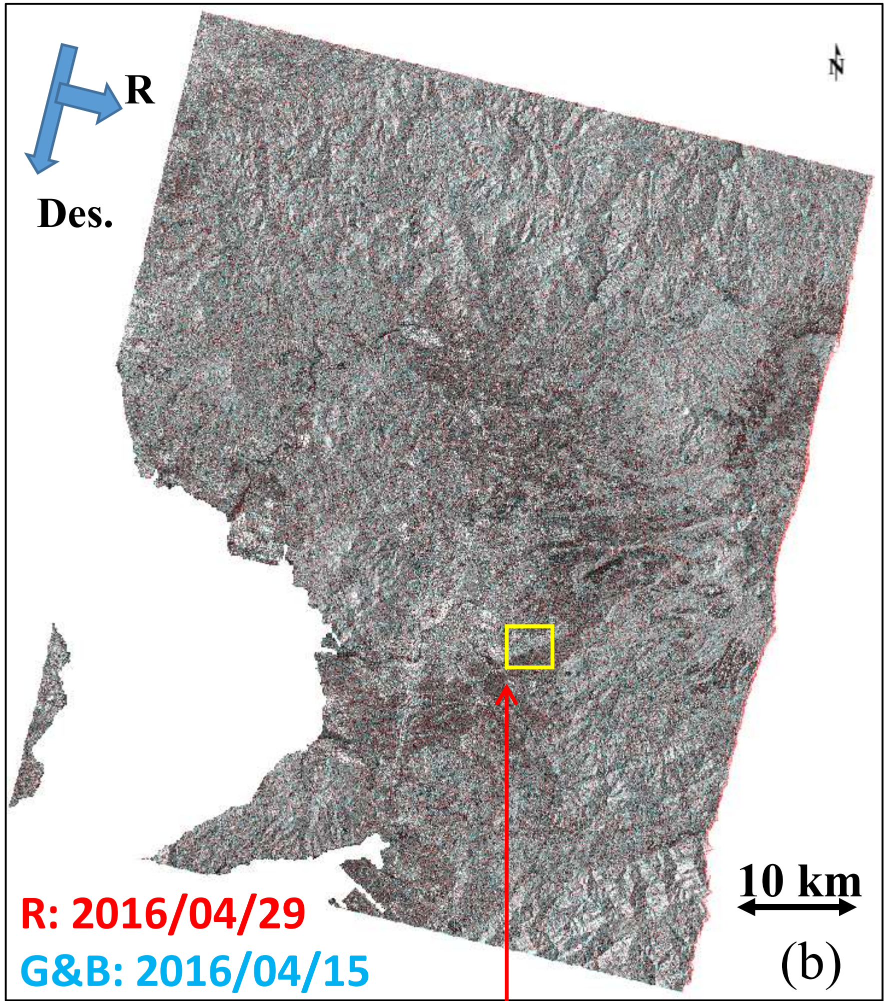

Pre-event: 2016/04/15 **Post-event**: 2016/04/29
Off-nadir angle: 32.4°, Mode: StripMap, Polarization: HH
Resolution: 1.43 m (range) and 1.74 m (azimuth)

the target area in Mashiki town

Coherence between the two PALSAR-2 images (2016/4/15 vs 2016/4/29) for the urban land-cover in the central Mashiki Town

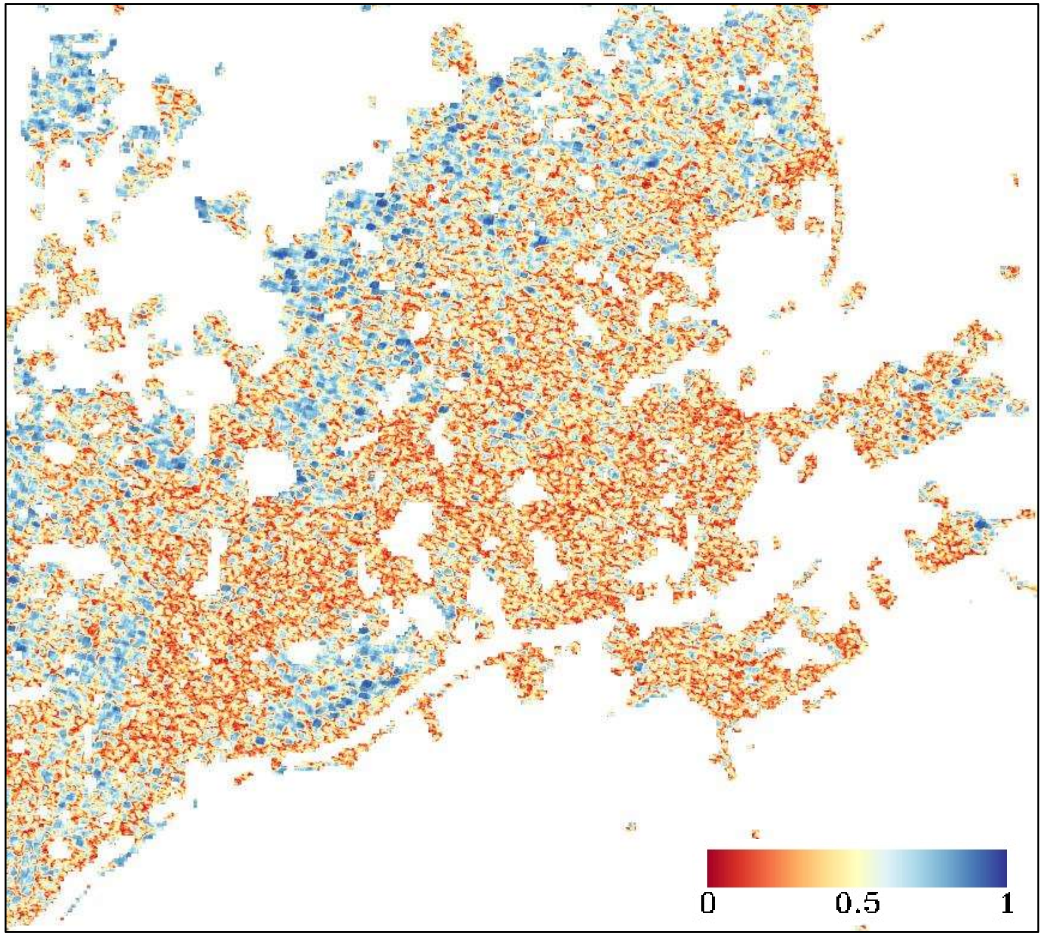

Coherence

$$\gamma = \frac{\sum C_1 C_2}{\sqrt{\sum |C_1|^2}\sqrt{\sum |C_1|^2}}$$

C is a complex number with phase (ϕ) and magnitude (A)

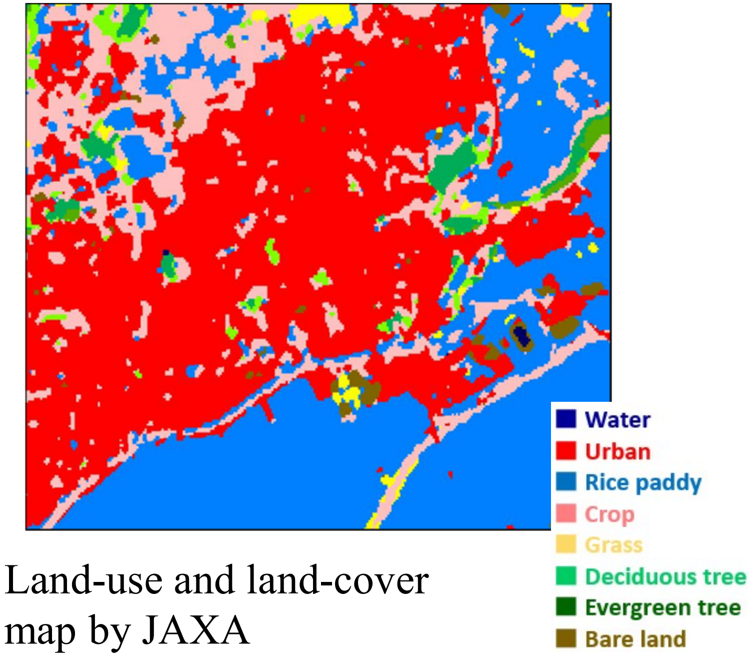

Land-use and land-cover map by JAXA

For entire images

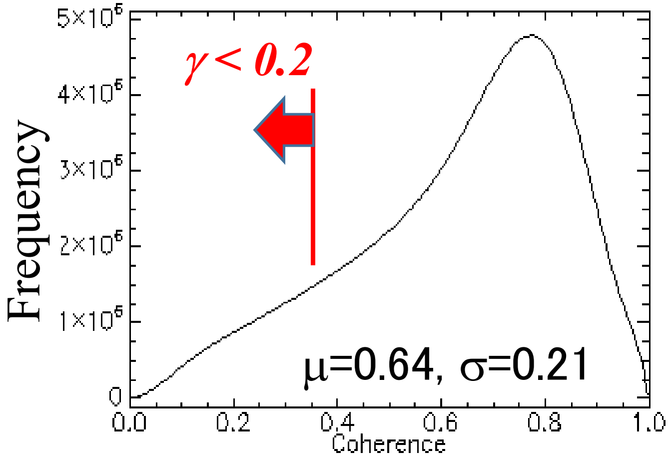

Abs. Coherence

W. Liu, F. Yamazaki Journal of Disaster Research, Vol. 12, No. 2, 2017.

Extraction of changrd areas by coherence and height-difference

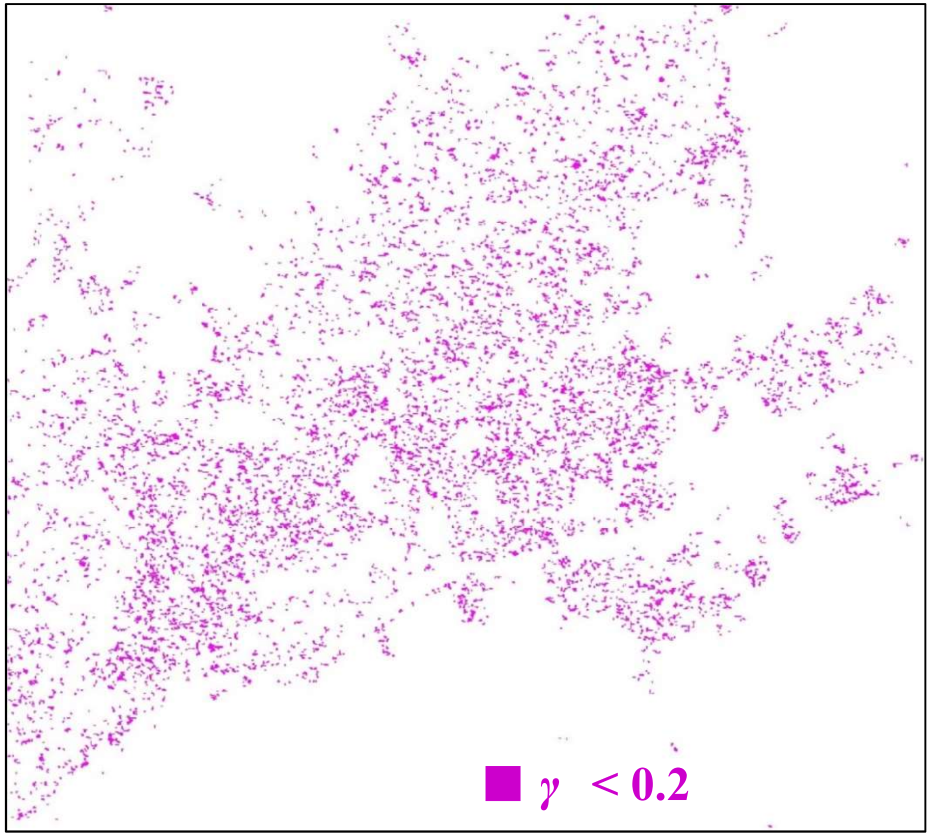

Areas extracted by
low coherence ($\gamma < 0.2$)

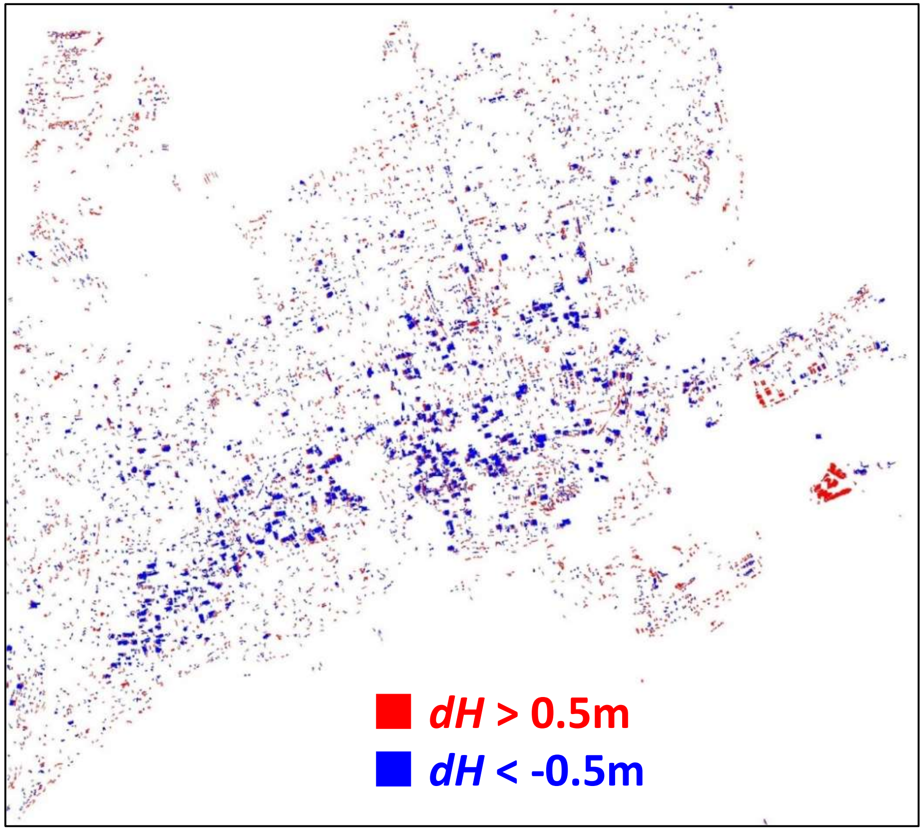

Areas extracted by DSM difference: **|dH| > 0.5 m**

Coherence and the extracted area by the coherence threshold

Height difference and the area exceeding ± the thresholds

the extracted area = about 9 %

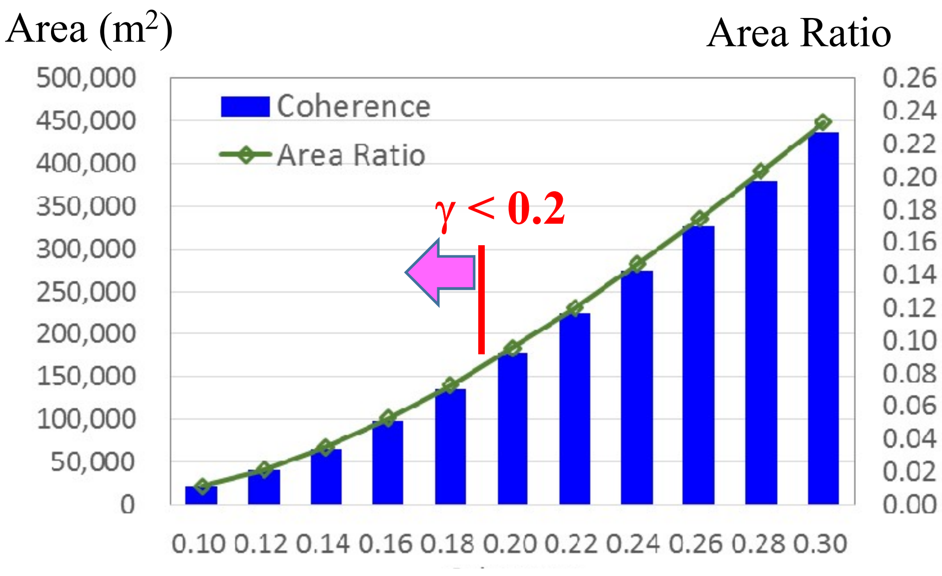

(a)

the extracted area = about 8.5 %

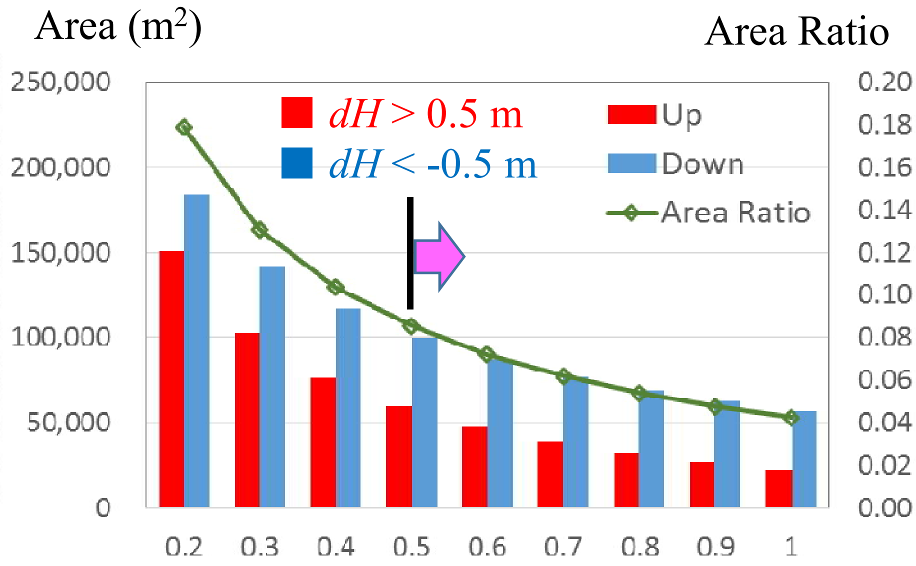

(b)

F. Yamazaki, L. Moya, W. Liu, Use of multi-temporal Lidar data to extract changes due to the 2016 Kumamoto earthquake, Proc. of SPIE, 2017

Drone (UAV) flight in Onagawa on Nov. 14, 2014

March 19, 2011 by GSI

Phantom2 vision+ 2014.11.14

H= 30 m

Building B

Structure from Motion (**SfM**) and Developed 3D Model

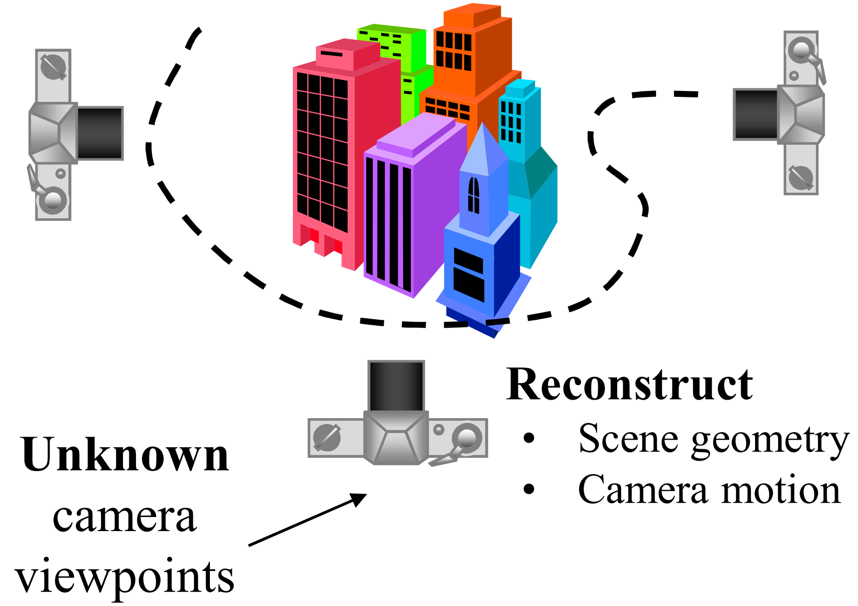

- Construction of 3D model of structures from many images with unknown positions.

- Combination of

●Computer Vision -- 3D modeling

●Robot Vision -- camera position

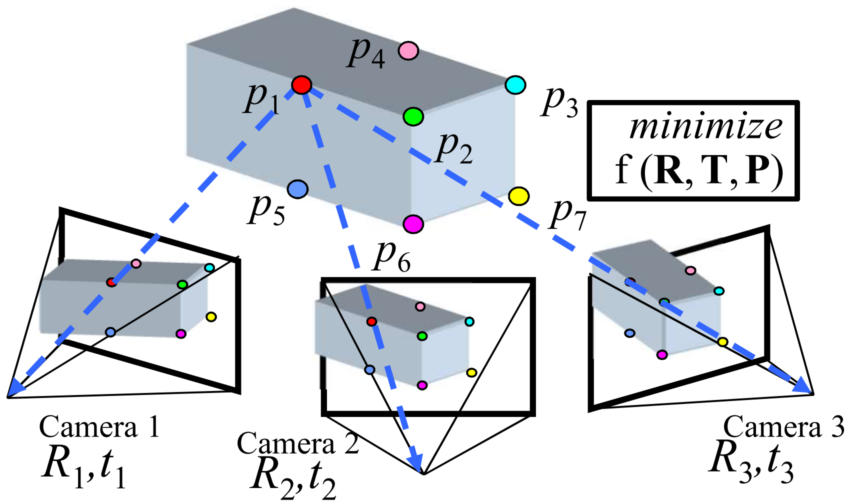

Agisoft *PhotoScan*

F. Yamazaki, T. Matsuda, S. Denda, W. LiuConstruction of 3D models of buildings damaged by earthquakes using UAV aerial images,, 9th Pacific Conference on Earthquake Engineering, Sydney, 2015.

Summary

- **Application of remote sensing** technologies to **disaster response** was discussed based on real earthquake events.
- **Optical satellite** images were used to observe **floods**, **landslides**, and damages to **built environment**. The **improvement of resolution** enabled us to monitor small-scale damages.
- **Thermal** satellite sensor could extract **flooded areas** as well as bush fires and volcanic activities.
- **Satellite SAR** sensors were used to extract **various damage situation**, even at night and under cloud-cover conditions.
- **Airborne SAR** can be used for detailed land-cover and damage mapping.
- **Aerial surveys** by airplanes and **drones** were carried out to observe detailed damage situations. **LiDAR** is also promising to observe the ground-surface situations.

Acknowledgements

JAXA, NICT, PASCO, Asia Air Survey Co., Ltd.,
GSI, JSPS_KAKENHI, JST_J-Rapid